



저작자표시-비영리-변경금지 2.0 대한민국

이용자는 아래의 조건을 따르는 경우에 한하여 자유롭게

- 이 저작물을 복제, 배포, 전송, 전시, 공연 및 방송할 수 있습니다.

다음과 같은 조건을 따라야 합니다:



저작자표시. 귀하는 원 저작자를 표시하여야 합니다.



비영리. 귀하는 이 저작물을 영리 목적으로 이용할 수 없습니다.



변경금지. 귀하는 이 저작물을 개작, 변형 또는 가공할 수 없습니다.

- 귀하는, 이 저작물의 재이용이나 배포의 경우, 이 저작물에 적용된 이용허락조건을 명확하게 나타내어야 합니다.
- 저작권자로부터 별도의 허가를 받으면 이러한 조건들은 적용되지 않습니다.

저작권법에 따른 이용자의 권리와 책임은 위의 내용에 의하여 영향을 받지 않습니다.

이것은 [이용허락규약\(Legal Code\)](#)을 이해하기 쉽게 요약한 것입니다.

[Disclaimer](#)



공학박사 학위논문

리튬 과잉 복합 양극 소재 상형성 기구 연구

Phase evolution study of lithium-rich composite oxide for Li-ion batteries

2017년 2월

서울대학교 대학원

재료공학부

최병진

Abstract

Phase evolution study of lithium-rich composite oxide for Li-ion batteries

Byungjin Choi

Department of Materials Science and Engineering

Seoul National University

The composite material $\text{Li}_x\text{Ni}_{0.25}\text{Co}_{0.10}\text{Mn}_{0.65}\text{O}_{(3.4+x)/2}$ ($x=1.6, 1.4, 1.2, 1.0, 0.8$) were synthesized and characterized for their structural, morphological, and performance as cathode materials in Li-ion batteries. The Rietveld refinement results indicate the presence of two phases at high lithium levels ($x=1.6$ and 1.4): Li_2MnO_3 ($\text{C}2/\text{m}$) and LiMO_2 ($\text{M} = \text{Ni, Co, Mn}$) ($\text{R}3\bar{m}$); the latter contains Ni^{2+} and Ni^{3+} . At low lithium levels ($x=1.2, 1.0$, and 0.8) an additional spinel phase LiM_2O_4 ($\text{Fd}3\bar{m}$) emerges, which is known to affect the electrochemical performance of the oxide. Structural analysis reveals that the spinel phase contains mixed transition metals Ni, Co, and Mn as $[\text{Li}^+, \text{Co}^{2+}][\text{Ni}^{2+}, \text{Co}^{3+}, \text{Mn}^{4+}]_2\text{O}_4$. A low lithium level is found to induce primary particle growth, as well as Co and Ni segregation within the secondary particles. These results are expected to contribute to material

optimization and commercialization of lithium-rich oxide cathodes.

The composite material $\text{Li}_2\text{MnO}_3 \cdot \text{Li}(\text{Ni},\text{Co},\text{Mn})\text{O}_2 \cdot \text{LiM}_{0.5}\text{Mn}_{1.5}\text{O}_4$ ($\text{M} = \text{Mn, Ni, Co}$) were synthesized and characterized for their structural, morphological, and performance as cathode materials in Li-ion batteries. XRD analysis indicates the presence of Li_2MnO_2 ($\text{C}2/\text{m}$), $\text{Li}(\text{Ni},\text{Co},\text{Mn})\text{O}_2$ ($\text{R}3\bar{m}$), and spinel phase $\text{LiM}_{0.5}\text{Mn}_{1.5}\text{O}_4$ ($\text{M} = \text{Mn, Ni, Co}$) ($\text{Fd}3\bar{m}$). In $\text{LiM}_{0.5}\text{Mn}_{1.5}\text{O}_4$ ($\text{M} = \text{Mn}$) ($\text{Fd}3\bar{m}$) composition spinel LiMn_2O_4 phase is embedded. At 20mol% embedding additionally $\text{LiNi}_{0.5}\text{Mn}_{1.5}\text{O}_4$ phase is also detected. Rocksalt NiO phase is formed in $\text{LiM}_{0.5}\text{Mn}_{1.5}\text{O}_4$ ($\text{M} = \text{Ni}$) composition even in oxygen atmosphere. $\text{LiM}_{0.5}\text{Mn}_{1.5}\text{O}_4$ ($\text{M} = \text{Co}$) composite composition is homogeneously synthesized even in 20mol% embedding. By embedding $\text{LiCo}_{0.5}\text{Mn}_{1.5}\text{O}_4$ phase the electrochemical performance in 18650 full cell using graphite anode is improved. Spinel embedding in lithium-rich composite oxide can improve the electrochemical performance through structural stability. The phase content, crystal size and lattice parameters were analyzed through the Rietveld refinement in $\text{LiM}_{0.5}\text{Mn}_{1.5}\text{O}_4$ ($\text{M} = \text{Co}$) composite composition. Spinel embedding induces primary particle growth during heat-treatment, as well as Co and Ni segregation within the secondary particles. Ab initio calculation shows that spinel embedding in lithium-rich composite oxide can lower the formation energy by stabilizing the structure. The phase evolution process was analyzed during high temperature XRD method.

Keywords: **Li-ion batteries, lithium-rich oxides, spinel structure, Co segregation, Li_2MnO_3**

Student Number: 2014-30221

Contents

Abstract	i
List of Tables.....	vii
List of Figures	ix
Chapter 1. Introduction (Theoretical Review).....	1
1.1 Lithium ion battery.....	2
1.2 Cathode material for lithium ion battery	2
Chapter 2. Phase evolution of lithium-rich oxide	11
2.1 Introduction.....	12
2.2 Experimental Procedure	13
2.2.1 Synthesis.....	13
2.2.2 Instrumental Characterization	14
2.2.3 Computational Methods	15
2.2.4 Electrochemical Measurement.....	15

2.3 Results and discussion.....	16
2.3.1 Material Characterization	16
2.3.2 Identification of Composite phases and Their Growth Mechanism	21
2.4 Conclusions	23
Chapter 3. Spinel phase composite of lithium-rich oxide	41
3.1 Introduction.....	42
3.2 Experimental Procedure	43
3.2.1 Synthesis.....	43
3.2.2 Characterization and evaluation	43
3.2.3 Computational Methods	44
3.3. Results and Discussion.....	45
3.3.1 Spinel LiMn₂O₄ composite.....	45
3.3.2 Spinel LiNi_{0.5}Mn_{1.5}O₄ composite	56
3.3.3 Spinel LiCo_{0.5}Mn_{1.5}O₄ composite	65

3.4. Conclusions.....	83
Chapter 4. Conclusion	91
References	94
초 록	105

List of Tables

Table 2.1 Elemental analysis for the materials under study

Table 2.2 The results of the Rietveld refinement for the materials under study

Table 2.3 XAFS analysis at the Ni K edge (d), Co K edge (e), and Mn K edge (f) for Li_{1.60}, Li_{1.40}, Li_{1.20}, Li_{1.00}, and Li_{0.80}.

Table 2.4 Rate capability tests of (1) Li1.60, (2) Li1.40, (3) Li1.20, (4) Li1.00, (5) Li0.80 at different currents (C rates) in the potential range 2.5-4.6V in coin type cells. Li counter electrodes.

Table 2.5 Composition calculation for 5 compositions with different lithium levels. Labels (1)-(4) refer to the spinel phase types LiNi_{0.5}Mn_{1.5}O₄, LiCo_{0.5}Mn_{1.5}O₄, LiMn₂O₄ and [Li⁺,Co²⁺][Ni²⁺,Co³⁺,Mn⁴⁺]₂O₄ respectively.

Table 3.1.1 Electrochemical performance tests of spinel (1) 0, (2) 2, (3) 5, (4) 10, and (5) 20mol% heat-treated at 900degC at different currents (C rates) in the potential range 2.5-4.6/4.7V in coin type cells. Li counter electrodes.

Table 3.1.2 Electrochemical performance tests of spinel (1) 0, (2) 2, (3) 5, (4) 10, and (5) 20mol% heat-treated at 750degC at different currents (C rates) in the potential range 2.5-4.6/4.7V in coin type cells. Li counter electrodes.

Table 3.2.1 Electrochemical performance tests of spinel (1) 0, (2) 2, (3) 5, (4) 10, and (5) 20mol% heat-treated at 900degC in air at different currents (C rates) in the potential range 2.5-4.6/4.7V in coin type cells. Li counter electrodes.

Table 3.3.1 Electrochemical performance tests of spinel (1) 0, (2) 2, (3) 5, and

(4) 10mol% heat-treated at 900degC at different currents (C rates) in the potential range 2.5-4.6/4.7V in coin type cells. Li counter electrodes.

Table 3.3.2 The results of the Rietveld refinement for the materials under study

Table 3.3.3 Electrochemical performance tests of spinel (1) 0, (2) 2, (3) 5, and (4) 10mol% heat-treated at 750degC at different currents (C rates) in the potential range 2.5-4.6/4.7V in coin type cells. Li counter electrodes.

Table 3.4.1 Summary of spinel composites.

List of Figures

Figure 1.1 Schematic drawing of lithium ion battery operation.

Figure 1.2 Initial charge-discharge profiles measured upon galvanostatic cycle.

Figure 1.3 Schematics of operational voltage difference in various cathode materials.

Figure 1.4 Compositional phase diagram of lithium-rich $\text{Li}(\text{Ni},\text{Co},\text{Mn})\text{O}_2$.

Figure 1.5 Voltage decay of lithium-rich $\text{Li}(\text{Ni},\text{Co},\text{Mn})\text{O}_2$ during charge-discharge cycling.

Figure 1.6 Spinel phase evolution in lithium-rich $\text{Li}(\text{Ni},\text{Co},\text{Mn})\text{O}_2$.

Figure 2.1 (a) Panels (1)-(5) are XRD patterns of $\text{Li}_{1.60}$, $\text{Li}_{1.40}$, $\text{Li}_{1.20}$, $\text{Li}_{1.00}$ and $\text{Li}_{0.80}$ respectively, after heat-treatment at 900 °C. Selected angular ranges highlight the (b) layered and (c) spinel peaks.

Figure 2.2 (a) High-resolution TEM image taken from the $\text{Li}_{1.00}$ composition. (b) and (c) Local structural information from Fast-Fourier Transformations of regions 1 region 2, respectively. The extra row of spots indicated by the arrow in (c) show a spinel structure.

Figure 2.3 Rietveld refinement for the phase contents in $\text{Li}_{1.60}\text{-Li}_{0.80}$ compositions. The fractions are calculated with the composite notation like $\text{Li}_2\text{MnO}_3 \cdot \text{Li}(\text{Ni},\text{Co},\text{Mn})\text{O}_2 \cdot \text{LiM}_x\text{Mn}_{2-x}\text{O}_4$ ($\text{M}=\text{Ni, Co, Mn}$).

Figure 2.4 XANES spectra of $\text{Li}_{1.60}\text{-Li}_{0.80}$ compositions at (a) the Ni K-edge, (b) Co K-edge, and (c) Mn K-edge. XAFS spectra at (d) the Ni K-edge, (e) Co K-edge, and (f) Mn K-edge .

Figure 2.5 (a) XRD patterns of LiMn_2O_4 and $\text{LiNi}_{0.5}\text{Mn}_{1.5}\text{O}_4$ heat-treated at 900degC. (b) and (c) Selected XRD angular range highlighting the difference between LiMn_2O_4 and $\text{LiNi}_{0.5}\text{Mn}_{1.5}\text{O}_4$.

Figure 2.6 FESEM images of (a0) $\text{Ni}_{0.25}\text{Co}_{0.10}\text{Mn}_{0.65}(\text{OH})_2$ precursor and (a)-(e) Li1.60-Li0.80 compositions heat-treated at 900 °C.

Figure 2.7 Cross-sectional EPMA mapping and images of (a) Li1.40, (b) Li1.20, and (c) Li1.00. A scale bar is located at the lower right corner.

Figure 2.8 a)-(e) Initial charge-discharge profiles measured upon galvanostatic cycle of Li1.60-Li0.80 compositions. The data are recorded at 23 mA/g (C/10) rate in the potential range of 2.5-4.7V in coin-type cells with Li counter electrodes.

Figure 2.9 Plots of specific capacity vs. cycle number of (1) Li1.60, (2) Li1.40, (3) Li1.20, (4) Li1.00, (5) Li0.80 at 1C rate (230mA/g) in the potential range 2.5-4.6V in coin type cells. Li counter electrodes.

Figure 2.10 Initial charge-discharge profiles measured upon galvanostatic cycle of (a) Li1.60, (b) Li1.40, (c) Li0.80 at 23mA/g (C/10) rate in the potential range of 3.0-5.0V in coin type cells, Li counter electrodes.

Figure 2.11 Schematic drawing showing the proposed phase evolution process for high and low lithium compositions.

Figure 3.1.1 Synthesis procedure for spinel composite oxide

Figure 3.1.2 (a) Panels (1)-(5) are XRD patterns of spinel 0, 2, 5, 10, and 20mol% respectively, after heat-treatment at 900 °C. Selected angular ranges

highlight the (b) layered and (c) spinel peaks.

Figure 3.1.3 FESEM images of spinel composites (a) 0, (b) 2, (c) 5, (d) 10, and (e) 20mol% heat-treated at 900 °C.

Figure 3.1.4 (a)-(d) Initial charge-discharge profiles measured upon galvanostatic cycle of spinel 0-20mol% compositions heat-treated at 900degC. The data are recorded at 23 mA/g (C/10) rate in the potential range of 2.5-4.7V in coin-type cells with Li counter electrodes.

Figure 3.1.5 (a) Panels (1)-(5) are XRD patterns of spinel 0, 2, 5, 10, and 20mol% respectively, after heat-treatment at 750 °C. Selected angular ranges highlight the (b) layered and (c) spinel peaks.

Figure 3.1.6 FESEM images of spinel composites (a) 0, (b) 2, (c) 5, (d) 10, and (e) 20mol% heat-treated at 750 °C..

Figure 3.2.1 (a) Panels (1)-(5) are XRD patterns of spinel 0, 2, 5, 10, and 20mol% respectively, after heat-treatment at 900 °C in air. Selected angular ranges highlight the (b) layered and (c) spinel peaks.

Figure 3.2.2 (a) Panels (1)-(5) are XRD patterns of spinel 0, 2, 5, 10, and 20mol% respectively, after heat-treatment at 750 °C in air. Selected angular ranges highlight the (b) layered and (c) spinel peaks.

Figure 3.2.3 (a) Panels (1)-(5) are XRD patterns of spinel 0, 2, 5, 10, and 20mol% respectively, after heat-treatment at 900 °C in oxygen. Selected

angular ranges highlight the (b) layered and (c) spinel peaks.

Figure 3.2.4 (a) Panels (1)-(5) are XRD patterns of spinel 0, 2, 5, 10, and 20mol% respectively, after heat-treatment at 750 °C in oxygen. Selected angular ranges highlight the (b) layered and (c) spinel peaks.

Figure 3.2.5 (a)-(d) Initial charge-discharge profiles measured upon galvanostatic cycle of spinel 0-20mol% compositions heat-treated at 900degC in air. The data are recorded at 23 mA/g (C/10) rate in the potential range of 2.5-4.7V in coin-type cells with Li counter electrodes.

Figure 3.3.1 (a) Panels (1)-(5) are XRD patterns of spinel 0, 2, 5, 10, and 20mol% respectively, after heat-treatment at 900 °C. Selected angular ranges highlight the (b) layered and (c) spinel peaks.

Figure 3.3.2 Rietveld refinement for the phase contents in (1-x)[0.4Li₂MnO₃·0.6Li(Ni,Co,Mn)O₂]·xLiCo_{0.5}Mn_{1.5}O₄ compositions. The fractions are calculated with the composite notation like Li₂MnO₃·Li(Ni,Co,Mn)O₂·LiM_xMn_{2-x}O₄ (M=Ni, Co, Mn).

Figure 3.3.3 FESEM images of spinel composites (a) 0, (b) 5, and (c) 20mol% heat-treated at 900 °C.

Figure 3.3.4 Cross-sectional EPMA mapping and images of spinel 20mol% composite heat-treated at 900degC. A scale bar is located at the right corner.

Figure 3.3.5 (a)-(c) HAADF image and EDS mapping taken from spinel

20mol% heat-treated at 900degC. (d) High-resolution TEM image taken from spinel 20mol% heat-treated at 900degC.

Figure 3.3.6 XPS data taken from spinel 20mol% heat-treated at 900degC.

Figure 3.3.7 (a) Panels (1)-(5) are XRD patterns of spinel 0, 2, 5, 10, and 20mol% respectively, after heat-treatment at 750 °C. Selected angular ranges highlight the (b) layered and (c) spinel peaks.

Figure 3.3.8 FESEM images of spinel composites (a) 0, (b) 5, and (c) 20mol% heat-treated at 750 °C.

Figure 3.3.9 Cross-sectional EPMA mapping and images of spinel 20mol% composite heat-treated at 750degC. A scale bar is located at the right corner.

Figure 3.3.10 (a)-(c) Initial charge-discharge profiles measured upon galvanostatic cycle of spinel 0-10mol% compositions heat-treated at 750degC. The data are recorded at 23 mA/g (C/10) rate in the potential range of 2.5-4.7V in coin-type cells with Li counter electrodes.

Figure 3.3.11 Full cell cycle life (a) discharge capacity retention (b) voltage decay in 18650-type full cells with graphite anode.

Figure 3.4.1 (a) Panels (1)-(4) are XRD patterns of spinel 0mol%, 20mol% LiMn_2O_4 , 20mol% $\text{LiNi}_{0.5}\text{Mn}_{1.5}\text{O}_4$ and 20mol% $\text{LiCo}_{0.5}\text{Mn}_{1.5}\text{O}_4$ respectively, after heat-treatment at 900 °C. Selected angular ranges highlight the (b) layered and (c) spinel peaks.

Figure 3.4.2 Formation energy of spinel embedded composite.

Figure 3.4.3 High temperature XRD of spinel embedded composite.

Figure 3.4.4 Schematic drawing showing the proposed phase evolution process for spinel embedded composite.

Chapter 1.

Introduction (Theoretical Review)

1.1 Lithium ion battery

Lithium ion battery operates at high voltage 3-4V range compared with other battery systems. High voltage operation can deliver more energy to consumer electronics and electric vehicles. The battery components are cathode, anode, electrolyte, and separator. Lithium ions intercalate between cathode and anode. Cathode material can accept the lithium ion in its crystal structure reversibly. LiCoO₂ as cathode and graphite as anode system was commercialized by Sony at 1991.[1, 2] During charging lithium ions are extracted from LiCoO₂ cathode and intercalated into graphite anode in Figure 1.1. The capacity means the amount of lithium which can be extracted from cathode, and the operational voltage is the difference in chemical potential between cathode and anode in Figure 1.2.

1.2 Cathode material for lithium ion battery

For high capacity and voltage cathode materials are required to have light weight and high chemical potential. LiMO₂ (M = transition metal) layered structure is used for lithium ion battery cathode material. The 3d transition metals are used for M in LiMO₂. LiCoO₂ and LiNiO₂ are well-known for layered structure. Spinel structure LiM₂O₄ and olivine structure LiMPO₄ are also used for lithium ion battery cathode, but the applications are limited due to lower capacity and rate performance. The operational voltage in different cathode materials is shown in Figure 1.3.

Among layered cathode material recently Ni-rich $\text{Li}(\text{Ni},\text{Co},\text{Mn})\text{O}_2$ and Li-rich and Mn-rich $\text{Li}(\text{Ni},\text{Co},\text{Mn})\text{O}_2$ are researched for high energy density battery. In Ni-rich $\text{Li}(\text{Ni},\text{Co},\text{Mn})\text{O}_2$ the high capacity is achieved $\text{Ni}^{2+/4+}$ redox reaction during charge-discharge. In Li-rich and Mn-rich $\text{Li}(\text{Ni},\text{Co},\text{Mn})\text{O}_2$ the high capacity is achieved through activation of oxygen in lithium-rich Li_2MnO_3 phase during high voltage activation above 4.5V in Figure 1.4.

1.3 The aim of this thesis

The demand for Li-ion batteries (LIBs) has increased rapidly owing to their relatively high energy density and design flexibility. LIBs are attractive energy sources for applications ranging from mobile devices to large-scale products such as electric vehicles (EV) and energy-storage systems (ESS).[3] However, the limited capacities from typical cathode materials such as LiCoO_2 and LiMn_2O_4 cannot satisfy the high energy density requirements for high-power LIBs used in EV and hybrid electric vehicles (HEV).

Lithium ion battery is widely used for consumer electronics, electric vehicles, and ESS application. Higher energy density is the key requirement to expand the application. Layered oxides are the most balanced material to meet the high energy and safety requirement. Lithium-rich $\text{Li}(\text{Ni},\text{Co},\text{Mn})\text{O}_2$ has been researched for commercialization because it shows high capacity above 250mAh/g.[4-6] The bottleneck for commercialization is the phase stability during charge-discharge condition.

During charge-discharge the structure is changed from layered to spinel. It affects power performance by decreasing average voltage in Figure 1.5. To improve the voltage decay various approaches have been tried. Doping, surface coating, and composite structure improved the performance even though much improvement is strongly needed. Spinel formation is reported for structural stability in Figure 1.6. By optimizing the spinel phase in lithium-rich $\text{Li}(\text{Ni},\text{Co},\text{Mn})\text{O}_2$ various approaches are attempted. The spinel phase evolution mechanism has to be clarified and electrochemical performance improvement is needed.

In chapter 2, the phase evolution during heat-treatment condition was investigated by controlling lithium content in precursor $\text{Ni}_{0.25}\text{Co}_{0.10}\text{Mn}_{0.65}(\text{OH})_2$. Structural analysis and ab initio calculation were used for clarifying phase evolution and stable phase structure.

In chapter 3, various spinel phases are embedded to improve the electrochemical performance. In precursor $\text{Ni}_{0.25}\text{Co}_{0.10}\text{Mn}_{0.65}(\text{OH})_2$ the spinel forming transition metal precursors(MnCO_3 , $\text{Co}(\text{OH})_2$, $\text{Ni}(\text{OH})_2$) were added and melt-infiltrated through heat-treatment with Li_2CO_3 . The composite structure and morphology were analyzed. The stable phase formation mechanism was explained. The electrochemical performances were analyzed using coin half-cell with lithium metal and 18650 full-cell with graphite.

Schematic of a LIB

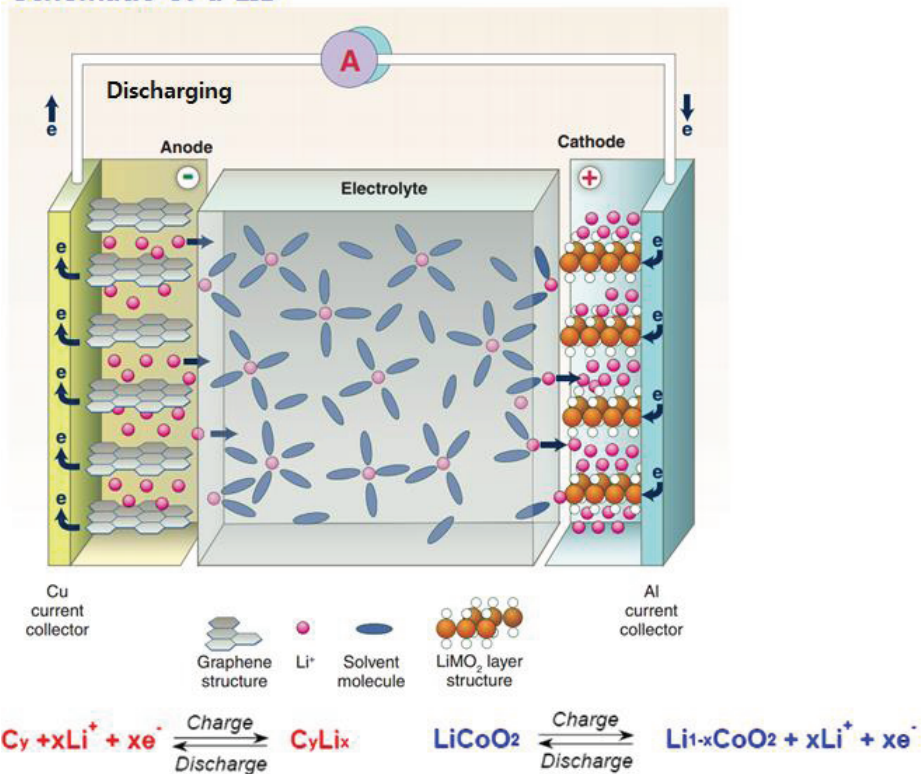


Figure 1.1 Schematic drawing of lithium ion battery operation. [7]

Operation of a LIB

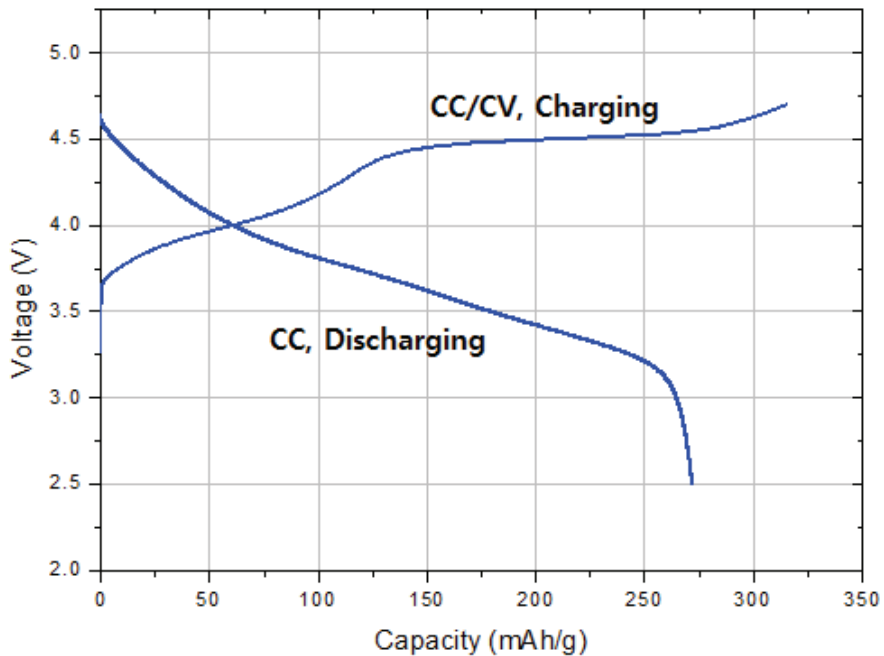


Figure 1.2 Initial charge-discharge profiles measured upon galvanostatic cycle.

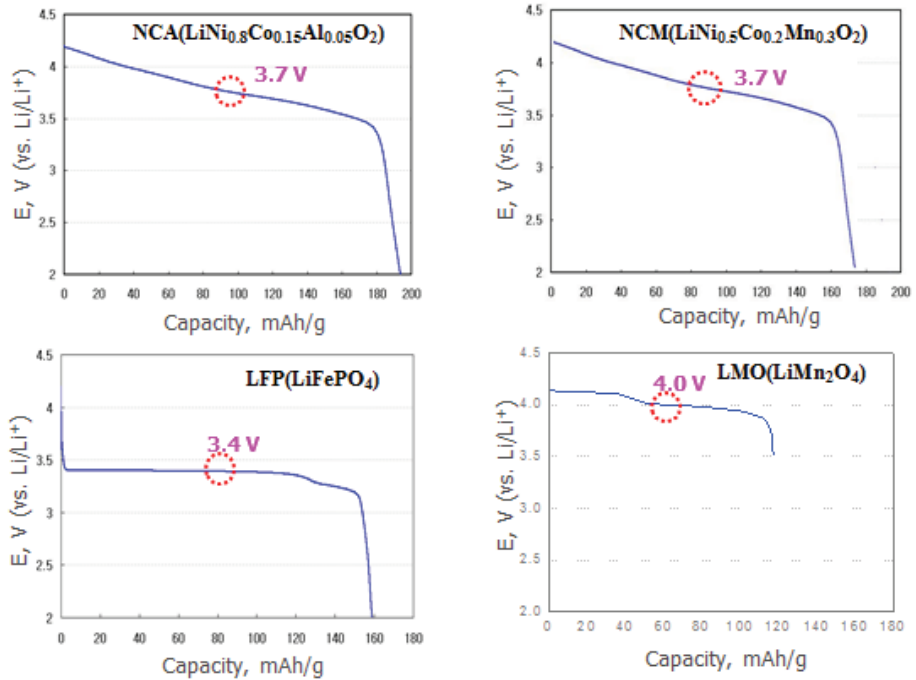


Figure 1.3 Schematics of operational voltage difference in various cathode materials.

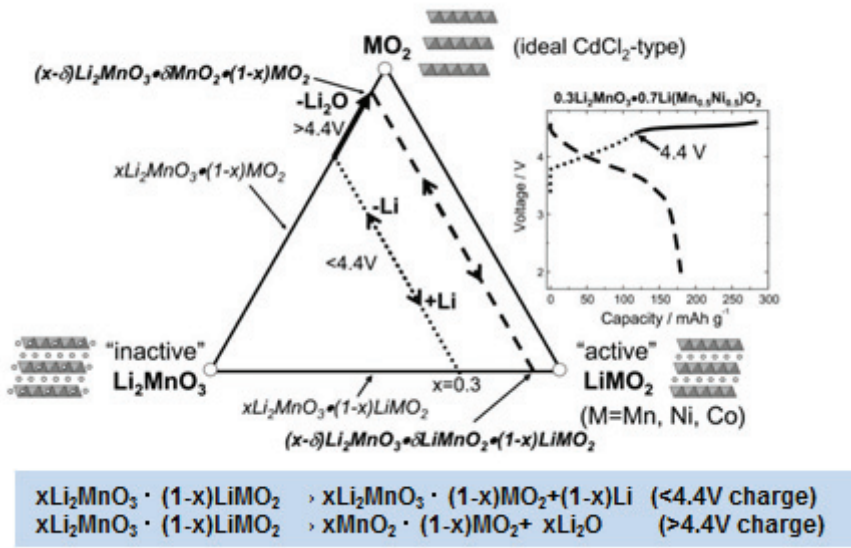


Figure 1.4 Compositional phase diagram of lithium-rich $\text{Li}(\text{Ni},\text{Co},\text{Mn})\text{O}_2$.[8]

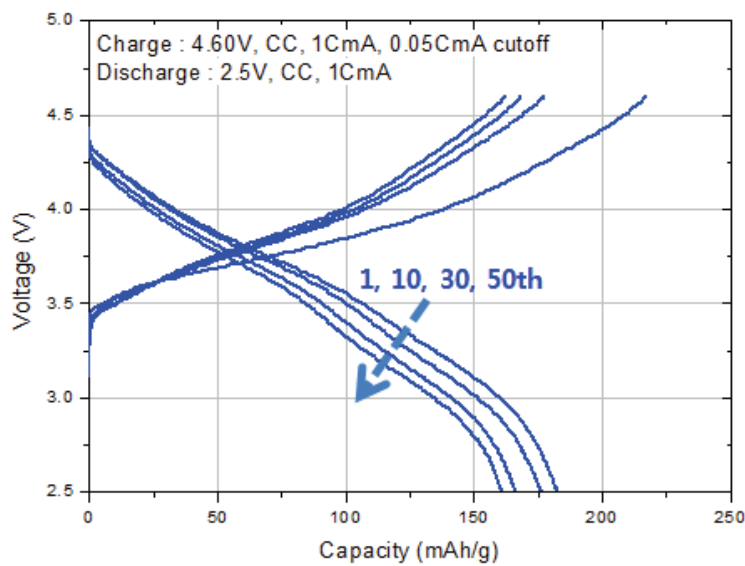


Figure 1.5 Voltage decay of lithium-rich $\text{Li}(\text{Ni},\text{Co},\text{Mn})\text{O}_2$ during charge-discharge cycling.

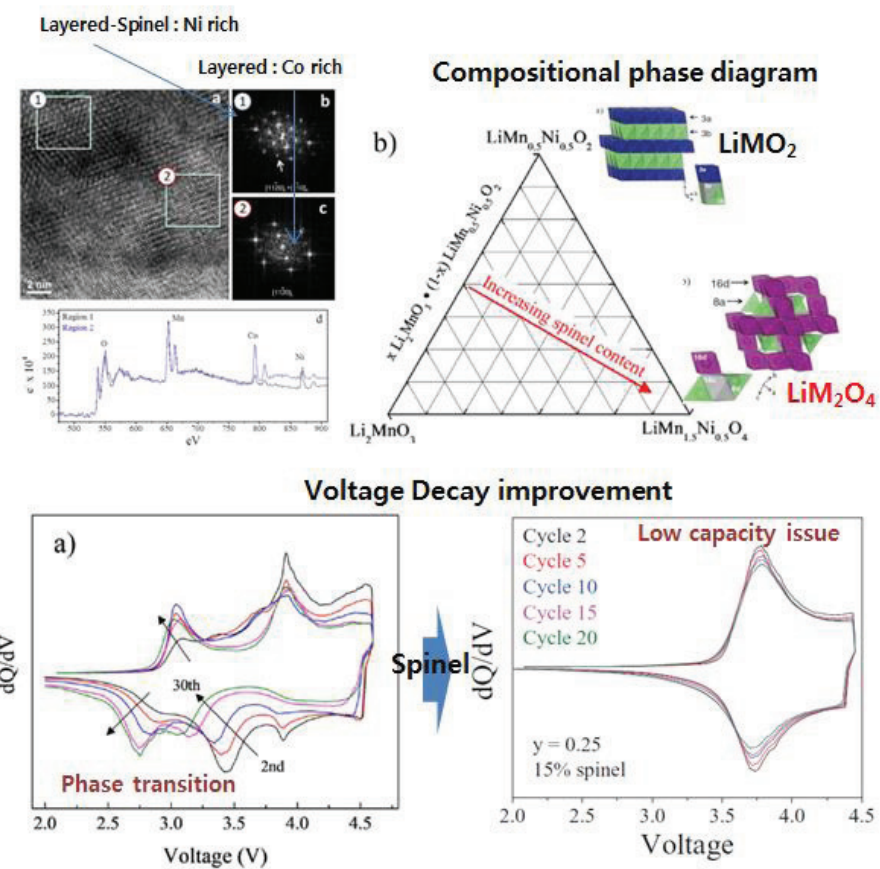


Figure 1.6 Spinel phase evolution in lithium-rich $\text{Li}(\text{Ni},\text{Co},\text{Mn})\text{O}_2$. [9]

Chapter 2.

Phase evolution of lithium-rich oxide

2.1 Introduction

Lithium-rich layered composite oxide cathode materials, referred to as over-lithiated layered oxides (OLO) in the composite system $\text{Li}_2\text{MnO}_3 \cdot \text{LiMO}_2$ (M = Ni, Co, Mn), have shown capacities exceeding 250 mAh/g at high operating voltages (>3.5 V vs. Li/Li⁺). However, lithium-rich oxide cathodes have several major drawbacks, including capacity loss during the first cycle, poor rate capability, and decreased cyclic performance. [3, 10] Various approaches, such as surface modification and composition change including doping, have been used to overcome these problems.[11] Surface modification was used to block side reactions between the electrolyte and cathode at high voltage, and suppress phase changes during the cycle. [12-15] Others have focused on optimizing the composition to reduce transition metal migration during cycling in order to maintain the high capacity (>250 mAh/g). [16-19]

After screening various compositions, our research group has focused on the cobalt-containing $\text{Li}_{1.40}\text{Ni}_{0.25}\text{Co}_{0.10}\text{Mn}_{0.65}\text{O}_{2.40}$ “baseline” composition for EV applications. [20] Similar compositions have been studied by other groups and have been demonstrated to show promising performance.[3, 16-19, 21-25] However, a systematic study of the structure and phase evolution in these compositions is still lacking, [3, 16-19] even though compositions with only Ni and Mn transition metals have been investigated extensively. [26-31]

The addition of cobalt to lithium-rich oxides induces structural and morphological changes, especially in the spinel phase formation. [3, 10, 16-19, 21-25] In the “layered-layered-spinel ($\text{Li}_2\text{MnO}_3 \cdot \text{LiMO}_2 \cdot \text{LiM}_x\text{Mn}_2$)

x O₄(M = Ni, Co, Mn))” composite structure, the initially embedded spinel phase has been shown to improve the voltage decay by stabilizing the “layered-layered (Li₂MnO₃·LiMO₂ (M = Ni, Co, Mn))” composite.[9, 32] The reported spinel phase in lithium-rich oxide are LiMn₂O₄ and LiNi_{0.5}Mn_{1.5}O₄.[9, 26, 29, 33, 34] When cobalt is included, it is important to identify the spinel structure and composition, including the mixed transition metal spinel phase. [35, 36]

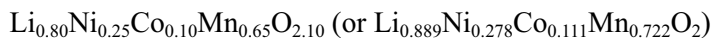
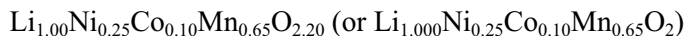
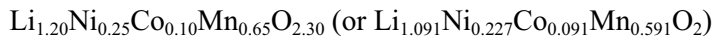
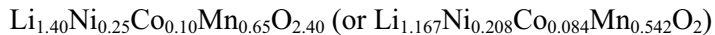
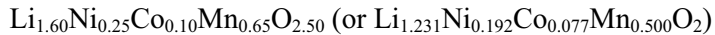
This work investigates the structural, morphological, and electrochemical performance changes in Li_xNi_{0.25}Co_{0.10}Mn_{0.65}O_{(3.4+x)/2} (x = 1.6, 1.4, 1.2, 1.0, 0.8). For brevity, they may be referred to as Li1.60 ...Li0.80 throughout the rest of the article. The analytical methods used here include high-resolution powder diffractometry (HRPD), scanning electron microscope (SEM), transmission electron microscope (TEM), X-ray absorption near edge structure (XANES), extended X-ray absorption fine structure (EXAFS), and electron probe microscopic analysis (EPMA).

2.2 Experimental Procedure

2.2.1 Synthesis

The Ni_{0.25}Co_{0.10}Mn_{0.65}(OH)₂ precursor was prepared through a hydroxide co-precipitation process. Proper amounts of NiSO₄·6H₂O, CoSO₄·7H₂O, and MnSO₄·H₂O were stirred in deionized water to form a homogeneous solution. The solution was chelated using NH₄OH and precipitated with NaOH. The co-precipitated Ni_{0.25}Co_{0.10}Mn_{0.65}(OH)₂ after

drying was mixed with Li_2CO_3 to form the composite material with the average composition $\text{Li}_x\text{Ni}_{0.25}\text{Co}_{0.10}\text{Mn}_{0.65}\text{O}_{(3.4+x)/2}$ ($x = 1.6, 1.4, 1.2, 1.0, 0.8$). [21, 29, 37] Their specific formulae are as follows:



The chemical formula in the parenthesis is the layered structure nomenclature of solid solution. The mixed powders were then calcined at 900 °C for 10 h in flowing air.

2.2.2 Instrumental Characterization

The crystal structures of the powder samples were determined by synchrotron HRPD performed at 9B HRPD beamline at Pohang Light Source II (PLS-II, Pohang, Korea) using the wavelength $\lambda=1.486$ Å. The data were refined using the FULLPROF program. XANES and EXAFS measurements were carried at 7D-XAFS beamline in Pohang Accelerator Laboratory, Korea. The XANES and EXAFS data were analyzed by established methods using the ATHENA software package. [38] Morphology changes of the powders were determined using SEM (S-4700N, Hitachi). The inductively coupled plasma technique (ICP-AES) was used to determine the ratios of Li, Ni, Co, and Mn elements in each sample. In order to observe the transition metal distributions in the secondary particles, cross sections of the powder particles were prepared by Ar ion milling on a LN2 cooled stage

and measured by an Electron Probe MicroAnalyzer (EPMA, JEOL JXA-8530F). The atomic-level structure and local phases were identified by diffraction and high-resolution TEM (FEI, Titan-cubed 60-300).

2.2.3 Computational Methods

The first principle calculations were performed using the Vienna ab initio simulation package (VASP) [39, 40] with the Projector-Augmented-Wave (PAW) method. [41] The exchange correlation interactions were included with the generalized gradient approximation Perdew-Burke-Ernzerhof (GGA-PBE) functional, [42] and the plane wave cutoff energy was set to 500 eV. The structure relaxations were carried out with a criteria of 10⁻⁴ eV for the total energy, and 0.02eV/Å for the forces on each atom. The effective on-site Hubbard U_{eff} corrections were 6.885, 5.95 and 5.0eV on the 3d electrons for Ni, Co and Mn atoms, respectively. [43] The supercells selected in this work contained between 8 and 28 unit cells, depending on the sample composition and structure.

2.2.4 Electrochemical Measurement

The electrodes were prepared by making a slurry of 92 wt% active material ($\text{Li}_x\text{Ni}_{0.25}\text{Co}_{0.10}\text{Mn}_{0.65}\text{O}_{(3.4+x)/2}$), 4 wt% conductive Denka Black, and 4 wt% polyvinylidene difluoride (PVDF) binder in N-methyl-2-pyrrolidone (NMP) as a solvent. The slurry was coated using doctor-blade method onto Al foil as a current collector. The electrodes were then dried at 120°C in vacuum and pressed. Metallic Li was used as the anode. The electrolyte solution was 1.3 mol L⁻¹ LiPF₆ dissolved in fluoroethylene carbonate and

dimethylene carbonate. A porous polyethylene-based membrane was used as a separator. The above components were assembled into CR2032-type coin cells in a dry room. The typical loading of the active mass was 10 mg/cm². The cells were charged to 4.7 V for one cycle and then cycled between 2.5 and 4.6 V vs. Li/Li⁺.

2.3 Results and discussion

2.3.1 Material Characterization

The XRD patterns of $\text{Li}_x\text{Ni}_{0.25}\text{Co}_{0.10}\text{Mn}_{0.65}\text{O}_{(3.4+x)/2}$ samples ($x = 1.6, 1.4, 1.2, 1.0, 0.8$) heat-treated at 900°C are shown in Figure 2.1. The oxygen stoichiometry was calculated to balance the total positive charge from the most stable oxidation states of Li⁺, Ni²⁺, Co³⁺, and Mn⁴⁺.[37, 44, 45] In Figure 1 (b), peaks of the Li_2MnO_3 (C2/m), LiMO_2 (R3⁻m) phases and the spinel phase $\text{LiM}_x\text{Mn}_{2-x}\text{O}_4$ (Fd3⁻m) ($M = \text{Ni, Co, Mn}$) were detected. The designed and calculated structure compositions are listed in Table 1. Note that different types of the spinel phase can lead to a number of possible compositions, which will be explained later. The actual elemental compositions obtained by ICP-AES in Table 2.1 agree with the designed stoichiometry within experimental error.

The Rietveld refinement was performed in order to clarify the phase contents and crystalline structures in the powder samples. Table 2.2 summarizes the lattice parameters of Li_2MnO_3 (C2/m), LiMO_2 (R3⁻m), and $\text{LiM}_x\text{Mn}_{2-x}\text{O}_4$ (Fd3⁻m). The phase contents were calculated from the main

and characterized peaks of each phase in Figure 2.1 (b). None of the samples could be assigned to a single phase structure; instead they were composites of two or three phases mentioned above. This composite nature led to the observed peak broadening, peak position shift and additional peaks. [37] Layered Li_2MnO_3 ($\text{C}2/\text{m}$) phase can be distinguished in $20.5\text{-}21^\circ$ range in Figure 2.1 (b), and is named “ Li_2MnO_3 -like super-lattice peak”. These peaks exist in all compositions studied here, but are particularly prominent in the low lithium samples (Li1.20, Li1.00 and Li0.80). The baseline composition Li1.40 consists of Li_2MnO_3 ($\text{C}2/\text{m}$) and LiMO_2 ($\text{R}3^-\text{m}$).

The composite structures of layered and spinel phases are also identified in high-resolution TEM results, as shown in Figure 2.2 (a). Figure 2.2 (b-c) display the fast-Fourier transformations (FFT) for regions marked 1 and 2 in (a), which exhibit layered and spinel structures, respectively. The row of spots indicated by the white arrow in Figure 2.2 (c) corresponds to the spinel phase, which is integrated with layered phase at the nanometer scale to form the composite structure.

Figure 2.3 shows the phase contents calculated from refined HRPD. In Li1.40 the phase contents of Li_2MnO_3 ($\text{C}2/\text{m}$) and LiMO_2 ($\text{R}3^-\text{m}$) are 56.4% and 43.6% respectively. As mentioned earlier, the low lithium samples Li1.20, Li1.00 and Li0.80 each contained three different phase structures: Li_2MnO_3 ($\text{C}2/\text{m}$), LiMO_2 ($\text{R}3^-\text{m}$) and LiM_2O_4 ($\text{Fd}3^-\text{m}$). From Li1.20 to Li0.80, the phase content of ($\text{Fd}3^-\text{m}$) increased[21] while that of ($\text{R}3^-\text{m}$) decreased. The ($\text{C}2/\text{m}$) phase content reached maximum at Li1.20 and decreased monotonously to Li0.80 at lower lithium contents. The larger phase content of Li_2MnO_3 phase might be exaggerated, though. This is

because Li_2MnO_3 has a higher degree of crystallinity than the other phases due to the high temperature calcination. The high-lithium sample Li1.60 has increased ($\text{C}2/\text{m}$) and decreased ($\text{R}3^-\text{m}$) phase contents, when compared to the baseline composition Li1.40. This is consistent with the tendency found in a previous study. [37] At the initial calcination stage, the lithium would be used preferentially to form the ($\text{C}2/\text{m}$) phase, and this phase is based on the formation of LiMn_6 clustering, which is thermodynamically stable during the heat treatment process. [46-48] The ($\text{Fd}3^-\text{m}$) phase appears after ($\text{C}2/\text{m}$). [49] The phase content of ($\text{R}3^-\text{m}$) phase finally gets smaller. Therefore the phase fraction of ($\text{R}3^-\text{m}$) phase decreases with the lithium content, from 43.6% in Li1.40 to 13.7% in Li0.80, as shown in Figure 2.3.

In Table 2.2, the lattice parameters in the a-axis and c-axis of ($\text{C}2/\text{m}$) show only small variations across all lithium contents, as it suggests there is little change in the transition metal composition. On the other hand, the a-axis and c-axis of ($\text{R}3^-\text{m}$) are significantly decreased at the higher lithium content, which suggest the composition variation of the transition metals.

Figure 2.4 (a-c) display the XANES spectra as the lithium content is varied. Generally, XANES peaks are shifted to a lower energy region as the number of valence electrons increases due to the core-hole screening effect, and the peak shapes are related to its interaction with neighboring elements. For the Ni K-edge, the peak shapes for all compositions except Li1.60 are almost identical. Only the peak of Li1.60 shifted to higher energy in Figure 2.4 (a), which means nickel is partially changed from Ni^{2+} to Ni^{3+} for the charge balance. The peak shapes for all

compositions except Li1.60 are almost identical. The Co K-edge spectra display more variation in peak positions and shapes. The shape change is due to rearrangement of the surrounding atoms induced by lithium content change. The peak shift confirms the oxidation state change in Co. When the lithium content was lower than the baseline Li1.40, the spectral peaks shifted to lower energy, which could be interpreted as partial reduction of Co^{3+} to Co^{2+} . On the other hand, the Co spectrum change between Li1.40 and Li1.60 was negligible. Mn K-edge XANES spectra of the samples exhibited negligible changes with Li contents (Figure 2.4 (c)).

In Figure 2.4 (d) the Ni K-edge XAFS shows that the spectral distribution in Li1.60 was increased because Ni^{3+} induced the Jahn-Teller distortion. The detailed EXAFS data are shown in Table 2.3. Co K-edge EXAFS shows the Co coordination changed from the octahedral to the tetrahedral site as the lithium content was lowered. In lower lithium compositions Co^{2+} might be formed in the tetrahedral site. Previously reported ($\text{Fd}\bar{3}\text{m}$) phase considered only Ni and Mn transition metals. [9, 26] Since Li_2MnO_3 ($\text{C}2/\text{m}$) and LiMO_2 ($\text{R}\bar{3}\text{m}$) do not have stable site for divalent Co ions, it was believed that the divalent Co ions participate in forming the ($\text{Fd}\bar{3}\text{m}$) spinel phase. This phase might be the mixed spinel phase $[\text{Li}^+, \text{Co}^{2+}][\text{Ni}^{2+}, \text{Co}^{3+}, \text{Mn}^{4+}]_2\text{O}_4$, [35, 50] with Co^{2+} and Co^{3+} occupying the tetrahedral and octahedral sites, respectively. The spectra of Mn K-edge in XANES and EXAFS are all very similar, indicating that the oxidation state and local interactions of Mn were not significantly affected by the lithium content.

In Figure 2.5, the XRD pattern of Li1.00 composition is

compared with those of three spinel structures: (1) $\text{LiNi}_{0.5}\text{Mn}_{1.5}\text{O}_4$, (2) $\text{LiCo}_{0.5}\text{Mn}_{1.5}\text{O}_4$, and (3) LiMn_2O_4 . The spinel (111) peak position in Li1.00 was located in a position close to $\text{LiNi}_{0.5}\text{Mn}_{1.5}\text{O}_4$ and $\text{LiCo}_{0.5}\text{Mn}_{1.5}\text{O}_4$ phases. This is also consistent with the spinel phase in Li1.00 being the mixed spinel phase (4) $[\text{Li}^+,\text{Co}^{2+}][\text{Ni}^{2+},\text{Co}^{3+},\text{Mn}^{4+}]_2\text{O}_4$.

Figure 2.6 shows SEM images of the precursor $\text{Ni}_{0.25}\text{Co}_{0.10}\text{Mn}_{0.65}(\text{OH})_2$ and all $\text{Li}_x\text{Ni}_{0.25}\text{Co}_{0.10}\text{Mn}_{0.65}\text{O}_{(3.4+x)/2}$ samples heat-treated at 900°C. In the precursor, flake-shaped primary particles agglomerated to form secondary particles about 5 μm in size after co-precipitation. After heat treatment, the primary particles grew into spheres with faceted morphology. The smallest primary particles, approximately 200 nm in size, occurred in Li1.40 baseline composition. At higher lithium content (Li1.60), the size increased to 400 nm (Figure 5 (a)), which could be attributed to the Li_2CO_3 phase which acts as a flux medium. [10] At lower lithium contents, the primary particles were larger and octahedral-shaped (Figure 5 (c)-(e)). The morphology and primary particle size change might be caused by an increase of the spinel ($\text{Fd}3\bar{m}$) phase content (Figure 3), as well as segregation of Co which is seen in the EPMA mapping results (Figure 6).

Figure 2.7 shows the EPMA composition mapping data. EPMA is generally used to determine the compositional distribution of transition metals. The powders were molded in epoxy and Ar ion-milled to reveal the vertical section of particles. In the baseline composition Li1.40, Ni, Co, and Mn were distributed uniformly within the spherical secondary particles. At lower lithium contents (Li1.20 and Li1.00), separate Ni-rich and Co-rich

regions formed inside a single particle. Mn, on the other hand, was uniformly distributed in all 5 calcinated compositions. Different diffusional mobilities and composition differences of Ni, Co and Mn in $\text{Ni}_{0.25}\text{Co}_{0.10}\text{Mn}_{0.65}(\text{OH})_2$ precursor might cause the segregation during the heat treatment at lower lithium levels. The segregated Co induced by lower lithium promotes particle growth. [51]

Figure 2.8 shows the charge-discharge profiles at the first cycle, i.e. activation at 4.7 V. The cells delivered discharge capacities of 188, 272, 216, 146, and $91 \text{ mAh}\cdot\text{g}^{-1}$ with Li1.60, Li1.40, Li1.20, Li1.00, and Li0.80 cathode materials, respectively. Table 2.4 lists the rate capabilities of these compositions. The specific capacity vs. cycle number results are shown in Figure 2.9. The baseline sample Li1.40 shows the best performance, as expected from our previous studies, [20] because it had the smallest particle sized and the optimized amount and composition of ($\text{C}2/\text{m}$) and ($\text{R}3^-\text{m}$) phases.[16] During charging all the compositions display a plateau around 4.5 V , which is known as the activation region of ($\text{C}2/\text{m}$) phase found at all lithium levels (Figure 2.8). In Li1.20, the plateau around 2.7 V during discharging is related to the electrochemical reaction of the spinel phase. This plateau remains visible in Li1.00 and Li0.80. The spinel plateau at 4.8 V during charging, shown in Figure 2.10, is also known as characteristic of high-voltage redox reaction of the spinel $\text{LiNi}_{0.5}\text{Mn}_{1.5}\text{O}_4$ phase.

2.3.2 Identification of Composite phases and Their Growth Mechanism

Based on the structural, morphological and electrochemical results

above, the possible compositions of different phases are calculated in Table 2.5. The assumption is that during heat treatment lithium will be ordered preferentially with Mn in LiMn_6 clustering in the transition metal layers, and form the Li_2MnO_3 phase. The remaining lithium will react with Ni, Co, and Mn to form the LiMO_2 and $\text{LiM}_x\text{Mn}_{2-x}\text{O}_4$ phases. Li1.60 contains both ($\text{C}2/\text{m}$) and Ni-rich ($\text{R}3\bar{\text{m}}$) phases, the latter having been observed in XANES spectra with coexisting Ni^{2+} and Ni^{3+} . At lower lithium levels, the spinel phase has been detected in XRD and electrochemical charging-discharging results.

The types of the spinel phase should be specified for each composition. A total of four types should be considered, as mentioned earlier. The calculated compositions are given in Table 1. At lower lithium levels, the most possible composite phase is the mixed spinel phase (4) $[\text{Li}^+, \text{Co}^{2+}][\text{Ni}^{2+}, \text{Co}^{3+}, \text{Mn}^{4+}]_2\text{O}_4$, indicated in bold and red color. Table 1 and Table S5 show the formation energy in the composite structure from ab initio calculations. The trend in these formation energies is consistent with the structural analysis results. For example, in Li1.00 the mixed spinel phase $0.4\text{Li}_2\text{MnO}_3 \cdot 0.2\text{LiNi}_{0.333}\text{Co}_{0.333}\text{Mn}_{0.333}\text{O}_2 \cdot 0.4\text{LiNi}_{0.707}\text{Co}_{0.180}\text{Mn}_{1.110}\text{O}_4$ has the lowest formation energy and therefore is the most stable structure. To match the phase content of 63.3% Li_2MnO_3 in Li1.00 obtained from Rietveld refinement (Figure 2.3), the phase content of 50% Li_2MnO_3 is also calculated. The LiMO_2 ($\text{R}3\bar{\text{m}}$) phase, however, cannot exist in this case; only Li_2MnO_3 ($\text{C}2/\text{m}$) and $\text{LiM}_x\text{Mn}_{2-x}\text{O}_4$ ($\text{Fd}3\bar{\text{m}}$) are present as $0.5\text{Li}_2\text{MnO}_3 \cdot 0.5\text{LiNi}_{0.75}\text{Co}_{0.30}\text{Mn}_{0.95}\text{O}_4$.

Figure 2.11 schematically sketches the phase evolution during

heat-treatment at high and low lithium levels. When the lithium is at the baseline (Li1.40) level or higher, the transition metals are distributed uniformly within the secondary particles during heat treatment. At lower lithium levels Co and Ni become segregated.

We have already seen that cobalt plays an important role in the elemental segregation and morphology. Cobalt has been reported to reduce the amount and domain size of (C2/m) phase.[25] Li et al. reported that increased cobalt content led to the acceleration of grain growth.[51] Cobalt also favors the layered structure and suppresses the spinel phase according to Deng et al.[21] The cobalt-rich domains, such as those in Figure 2.7, might easily form the (R3⁻m) phase, suppressing the growth of (C2/m). However, the nickel-rich domains might favorably form (Fd3⁻m) and (C2/m) phases instead. The voltage decay and capacity loss in the batteries induced by phase transition might be reduced through the possibility of a spinel phase with mixed transition metals.

2.4 Conclusions

Lithium-rich oxides $\text{Li}_x\text{Ni}_{0.25}\text{Co}_{0.10}\text{Mn}_{0.65}\text{O}_{(3.4+x)/2}$ ($x = 1.6, 1.4, 1.2, 1.0, 0.8$) were synthesized by hydroxide co-precipitation method. The baseline $x=1.4$ composition showed the best electrochemical performance due to its small primary particle size and homogeneous distribution of nano-sized phase domains. XRD, XANES and EXAFS studies indicate that the high-lithium compositions Li1.60 and Li1.40 consisted of two phases (C2/m) and (R3⁻m) phase which contains Ni^{2+} and Ni^{3+} . At lower lithium levels ($x < 1.4$) the composition contains three different phases: (C2/m), (R3⁻m) and

the spinel phase $\text{LiM}_x\text{Mn}^{2-x}\text{O}^4$ ($\text{Fd}3^- \text{m}$). EXAFS analysis shows that low lithium content forces Co to move from octahedral site to tetrahedral site, suggesting that the spinel phase might be composed of mixed transition metals as $[\text{Li}^+, \text{Co}^{2+}][\text{Ni}^{2+}, \text{Co}^{3+}, \text{Mn}^{4+}]_2\text{O}_4$. Low lithium condition is also shown to induce Co, Ni segregation and primary particle growth. As the spinel phase is known to affect the electrochemical performance of the composite, results presented here will help formulating the composition and synthesis protocol of cobalt-containing, lithium-rich oxides for optimal Li-ion batteries performance.

Table 2.1 Elemental analysis for the materials under study

Sample ^o	Elemental Analysis ⁺			
	<u>Ni+Co+Mn = 1 mol^o</u>			
	Li ^o	Ni ^o	Co ^o	Mn ^o
Li _{1.40} Ni _{0.25} Co _{0.10} Mn _{0.65} O _{2.40^o}	1.44 ^o	0.25 ^o	0.10 ^o	0.65 ^o
Li _{1.20} Ni _{0.25} Co _{0.10} Mn _{0.65} O _{2.30^o}	1.24 ^o	0.25 ^o	0.10 ^o	0.65 ^o
Li _{1.00} Ni _{0.25} Co _{0.10} Mn _{0.65} O _{2.20^o}	1.03 ^o	0.25 ^o	0.10 ^o	0.65 ^o
Li _{0.80} Ni _{0.25} Co _{0.10} Mn _{0.65} O _{2.10^o}	0.81 ^o	0.25 ^o	0.10 ^o	0.65 ^o

Table 2.2 The results of the Rietveld refinement for the materials under study

Composition ^a	Lattice Parameters ^a						
	Li ₂ MnO ₃ ^b (C2/m) ^c				Li(Ni,Co,Mn)O ₂ ^d (R-3m) ^e		LiM _x Mn _{1.5-x} O ₄ ^f (Fd-3m) ^g
	a ^h	b ^h	c ^h	beta ^h	a ^h	c ^h	a ^h
Li _{1.60} Ni _{0.25} Co _{0.10} Mn _{0.65} O _{2.50} ^h	4.9364(2) ⁱ	8.5405(3) ⁱ	5.0245(1) ⁱ	109.292(3) ⁱ	2.8492(1) ⁱ	14.2270(3) ⁱ	
Li _{1.40} Ni _{0.25} Co _{0.10} Mn _{0.65} O _{2.40} ^h	4.9573(2) ⁱ	8.5697(6) ⁱ	5.0350(2) ⁱ	109.359(5) ⁱ	2.8597(1) ⁱ	14.2516(3) ⁱ	
Li _{1.20} Ni _{0.25} Co _{0.10} Mn _{0.65} O _{2.30} ^h	4.9420(2) ⁱ	8.5514(3) ⁱ	5.0324(1) ⁱ	109.226(2) ⁱ	2.8952(1) ⁱ	14.3035(9) ⁱ	8.1564(3) ⁱ
Li _{1.00} Ni _{0.25} Co _{0.10} Mn _{0.65} O _{2.20} ^h	4.9394(2) ⁱ	8.5462(3) ⁱ	5.0333(2) ⁱ	109.257(2) ⁱ	2.8983(1) ⁱ	14.3209(6) ⁱ	8.1766(1) ⁱ
Li _{0.80} Ni _{0.25} Co _{0.10} Mn _{0.65} O _{2.10} ^h	4.9377(1) ⁱ	8.5468(2) ⁱ	5.0344(2) ⁱ	109.240(2) ⁱ	2.8991(1) ⁱ	14.3225(9) ⁱ	8.1794(1) ⁱ

Table 2.3 XAFS analysis at the Ni K edge (d), Co K edge (e), and Mn K edge (f)for Li_{1.60}, Li_{1.40}, Li_{1.20}, Li_{1.00}, and Li_{0.80}.

c	Ni K edge ^c				Co K edge ^c				Mn K edge ^c			
	Me-O (CN) ^c	Me-O (Å) ^c	$\Delta^2(\text{Å}^2)$ ^c	R-factor ^c	Me-O (CN) ^c	Me-O (Å) ^c	$\Delta^2(\text{Å}^2)$ ^c	R-factor ^c	Me-O (CN) ^c	Me-O (Å) ^c	$\Delta^2(\text{Å}^2)$ ^c	R-factor ^c
	Li _{1.60} ^c (0.433495) ^c	4.740680 ^c (0.008535) ^c	1.9376 ^c (0.001279) ^c	0.009156 ^c (0.001279) ^c	0.001816 ^c	5.987700 ^c (0.340673) ^c	1.9082 ^c (0.005100) ^c	0.001727 ^c (0.000699) ^c	0.001356 ^c (0.377452) ^c	5.914920 ^c (0.005414) ^c	1.9084 ^c (0.000748) ^c	0.001345 ^c (0.002498) ^c
Li _{1.40} ^c (0.474581) ^c	5.793592 ^c (0.007618) ^c	2.0232 ^c (0.001148) ^c	0.007303 ^c (0.001148) ^c	0.001606 ^c	5.961626 ^c (0.337249) ^c	1.9131 ^c (0.005067) ^c	0.001469 ^c (0.000685) ^c	0.001348 ^c (0.402843) ^c	5.990061 ^c (0.005741) ^c	1.9108 ^c (0.000795) ^c	0.001509 ^c (0.002760) ^c	
Li _{1.20} ^c (0.537983) ^c	5.872209 ^c (0.008556) ^c	2.0318 ^c (0.001251) ^c	0.006494 ^c (0.001251) ^c	0.002110 ^c	5.588494 ^c (0.359624) ^c	1.9136 ^c (0.005815) ^c	0.001645 ^c (0.000787) ^c	0.001742 ^c (0.406160) ^c	5.933904 ^c (0.005828) ^c	1.9107 ^c (0.000806) ^c	0.001432 ^c (0.002866) ^c	
Li _{1.00} ^c (0.686386) ^c	5.981148 ^c (0.010814) ^c	2.0344 ^c (0.001592) ^c	0.006874 ^c (0.001592) ^c	0.003218 ^c	5.258099 ^c (0.256709) ^c	1.9161 ^c (0.004520) ^c	0.002072 ^c (0.000608) ^c	0.000996 ^c (0.428826) ^c	5.937903 ^c (0.006162) ^c	1.9099 ^c (0.000853) ^c	0.001510 ^c (0.003180) ^c	
Li _{0.80} ^c (0.698743) ^c	6.164582 ^c (0.010749) ^c	2.0352 ^c (0.001598) ^c	0.007299 ^c (0.001598) ^c	0.003048 ^c	5.125883 ^c (0.280480) ^c	1.9142 ^c (0.005045) ^c	0.002047 ^c (0.000678) ^c	0.001246 ^c (0.460037) ^c	5.873368 ^c (0.006680) ^c	1.9093 ^c (0.000926) ^c	0.001583 ^c (0.003720) ^c	

Table 2.4 Rate capability tests of (1) Li1.60, (2) Li1.40, (3) Li1.20, (4) Li1.00, (5) Li0.80 at different currents (C rates) in the potential range 2.5-4.6V in coin type cells. Li counter electrodes.

o	1st cycle ^o			Discharge Rate @0.5C Cha ^o			
	0.1C Cha ^o	0.1C Dis. ^o	eff. ^o	0.2C ^o	1C Dis. ^o	2C Dis. ^o	2C vs. 0.2C ^o
	mAh/g ^o	mAh/g ^o	%	mAh/g ^o	mAh/g ^o	mAh/g ^o	%
Li _{1.60} Ni _{0.25} Co _{0.10} Mn _{0.65} O _{2.50} ^o	291 ^o	188 ^o	64.6% ^o	209 ^o	183 ^o	166 ^o	79.5% ^o
Li _{1.40} Ni _{0.25} Co _{0.10} Mn _{0.65} O _{2.40} ^o	315 ^o	272 ^o	86.3% ^o	256 ^o	219 ^o	208 ^o	81.3% ^o
Li _{1.20} Ni _{0.25} Co _{0.10} Mn _{0.65} O _{2.30} ^o	254 ^o	216 ^o	85.1% ^o	218 ^o	196 ^o	183 ^o	83.8% ^o
Li _{1.00} Ni _{0.25} Co _{0.10} Mn _{0.65} O _{2.20} ^o	173 ^o	146 ^o	84.4% ^o	145 ^o	116 ^o	107 ^o	73.7% ^o
Li _{0.80} Ni _{0.25} Co _{0.10} Mn _{0.65} O _{2.10} ^o	104 ^o	91 ^o	87.5% ^o	80 ^o	72 ^o	64 ^o	80.6% ^o

Table 2.5 Composition calculation for 5 compositions with different lithium levels. Labels (1)-(4) refer to the spinel phase types $\text{LiNi}_{0.5}\text{Mn}_{1.5}\text{O}_4$, $\text{LiCo}_{0.5}\text{Mn}_{1.5}\text{O}_4$, LiMn_2O_4 and $[\text{Li}^+,\text{Co}^{2+}][\text{Ni}^{2+},\text{Co}^{3+},\text{Mn}^{4+}]_2\text{O}_4$ respectively.

Composition : Synthesis-Design	Composition : Layered structure	Composition : Composite structure (Probable)	Formation Energy(eV/f.u.)	Remark
$\text{Li}_{1.60}\text{Ni}_{0.25}\text{Co}_{0.10}\text{Mn}_{0.65}\text{O}_{2.50}$	$\text{Li}_{1.23}\text{Ni}_{0.19}\text{Co}_{0.077}\text{Mn}_{0.50}\text{O}_2$	$0.6\text{Li}_2\text{MnO}_3 \cdot 0.4\text{LiNi}_{0.63}\text{Co}_{0.25}\text{Mn}_{0.126}\text{O}_2$	-	
$\text{Li}_{1.40}\text{Ni}_{0.25}\text{Co}_{0.10}\text{Mn}_{0.65}\text{O}_{2.40}$	$\text{Li}_{1.16}\text{Ni}_{0.20}\text{Co}_{0.084}\text{Mn}_{0.54}\text{O}_2$	$0.4\text{Li}_2\text{MnO}_3 \cdot 0.6\text{LiNi}_{0.417}\text{Co}_{0.147}\text{Mn}_{0.417}\text{O}_2$	-	Baseline
		(1) $0.350\text{Li}_2\text{MnO}_3 \cdot 0.525\text{LiNi}_{0.417}\text{Co}_{0.24}\text{Mn}_{0.36}\text{O}_2 \cdot 0.125\text{LiNi}_{0.5}\text{Mn}_{1.5}\text{O}_4$ (2) $0.350\text{Li}_2\text{MnO}_3 \cdot 0.525\text{LiNi}_{0.33}\text{Co}_{0.09}\text{Mn}_{0.36}\text{O}_2 \cdot 0.125\text{LiCo}_{0.5}\text{Mn}_{1.5}\text{O}_4$ (3) $0.350\text{Li}_2\text{MnO}_3 \cdot 0.525\text{LiNi}_{0.534}\text{Co}_{0.24}\text{Mn}_{0.25}\text{O}_2 \cdot 0.125\text{LiMn}_2\text{O}_4$ (4) $0.5\text{Li}_2\text{MnO}_3 \cdot 0.25\text{LiNi}_{0.333}\text{Co}_{0.333}\text{Mn}_{0.333}\text{O}_2 \cdot 0.25\text{LiNi}_{0.917}\text{Co}_{0.176}\text{Mn}_{0.917}\text{O}_4$ (5) $0.25\text{Li}_2\text{MnO}_3 \cdot 0.50\text{LiNi}_{0.375}\text{Co}_{0.20}\text{Mn}_{0.375}\text{O}_2 \cdot 0.25\text{LiNi}_{0.5}\text{Mn}_{1.5}\text{O}_4$ (6) $0.25\text{Li}_2\text{MnO}_3 \cdot 0.50\text{LiNi}_{0.455}\text{Mn}_{0.375}\text{O}_2 \cdot 0.25\text{LiCo}_{0.5}\text{Mn}_{1.5}\text{O}_4$	-29.941 -29.969 -29.884 -33.796	
$\text{Li}_{1.20}\text{Ni}_{0.25}\text{Co}_{0.10}\text{Mn}_{0.65}\text{O}_{2.30}$	$\text{Li}_{1.09}\text{Ni}_{0.22}\text{Co}_{0.091}\text{Mn}_{0.591}\text{O}_2$			
$\text{Li}_{1.00}\text{Ni}_{0.25}\text{Co}_{0.10}\text{Mn}_{0.65}\text{O}_{2.20}$	$\text{Li}_{1.00}\text{Ni}_{0.25}\text{Co}_{0.100}\text{Mn}_{0.650}\text{O}_2$	(1) $0.25\text{Li}_2\text{MnO}_3 \cdot 0.50\text{LiNi}_{0.625}\text{Co}_{0.25}\text{Mn}_{0.125}\text{O}_2 \cdot 0.25\text{LiMn}_2\text{O}_4$ (4) $0.4\text{Li}_2\text{MnO}_3 \cdot 0.2\text{LiNi}_{0.333}\text{Co}_{0.333}\text{Mn}_{0.333}\text{O}_2 \cdot 0.4\text{LiNi}_{0.707}\text{Co}_{0.188}\text{Mn}_{1.110}\text{O}_4$ (5) $0.5\text{Li}_2\text{MnO}_3 \cdot 0.5\text{LiNi}_{0.75}\text{Co}_{0.30}\text{Mn}_{0.50}\text{O}_4$	-31.161 -31.165 -31.424 -35.656 -	
$\text{Li}_{0.80}\text{Ni}_{0.25}\text{Co}_{0.10}\text{Mn}_{0.65}\text{O}_{2.10}$	$\text{Li}_{0.889}\text{Ni}_{0.278}\text{Co}_{0.111}\text{Mn}_{0.722}\text{O}_2$	(1) $0.15\text{Li}_2\text{MnO}_3 \cdot 0.413\text{LiNi}_{0.341}\text{Co}_{0.344}\text{Mn}_{0.311}\text{O}_2 \cdot 0.437\text{LiNi}_{0.5}\text{Mn}_{1.5}\text{O}_4$ (2) $0.75\text{LiNi}_{0.417}\text{Mn}_{0.58}\text{O}_2 \cdot 0.25\text{LiCo}_{0.5}\text{Mn}_{1.5}\text{O}_4$ (3) $0.75\text{LiNi}_{0.417}\text{Co}_{0.167}\text{Mn}_{0.416}\text{O}_2 \cdot 0.25\text{LiMn}_2\text{O}_4$ (4) $0.25\text{Li}_2\text{MnO}_3 \cdot 0.19\text{LiNi}_{0.333}\text{Co}_{0.333}\text{Mn}_{0.333}\text{O}_2 \cdot 0.56\text{LiNi}_{0.83}\text{Co}_{0.17}\text{Mn}_{1.25}\text{O}_4$ (5) $0.5\text{Li}_2\text{MnO}_3 \cdot 0.5\text{LiNi}_{0.75}\text{Co}_{0.30}\text{Mn}_{0.50}\text{O}_4$	-34.278 -28.780 -28.733 -37.130	

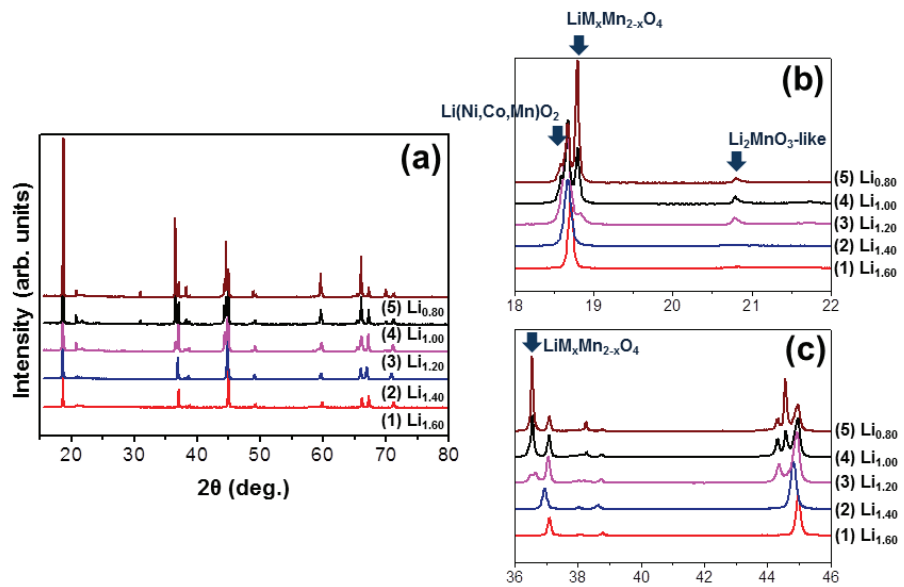


Figure 2.1 (a) Panels (1)-(5) are XRD patterns of $\text{Li}_{1.60}$, $\text{Li}_{1.40}$, $\text{Li}_{1.20}$, $\text{Li}_{1.00}$ and $\text{Li}_{0.80}$ respectively, after heat-treatment at 900°C . Selected angular ranges highlight the (b) layered and (c) spinel peaks.

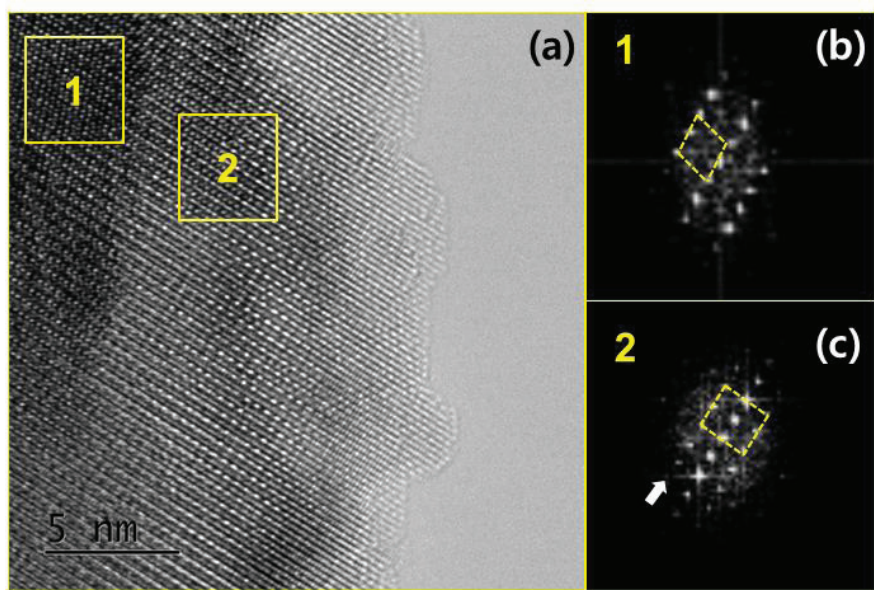


Figure 2.2 (a) High-resolution TEM image taken from the Li1.00 composition. (b) and (c) Local structural information from Fast-Fourier Transformations of regions 1 region 2, respectively. The extra row of spots indicated by the arrow in (c) show a spinel structure.

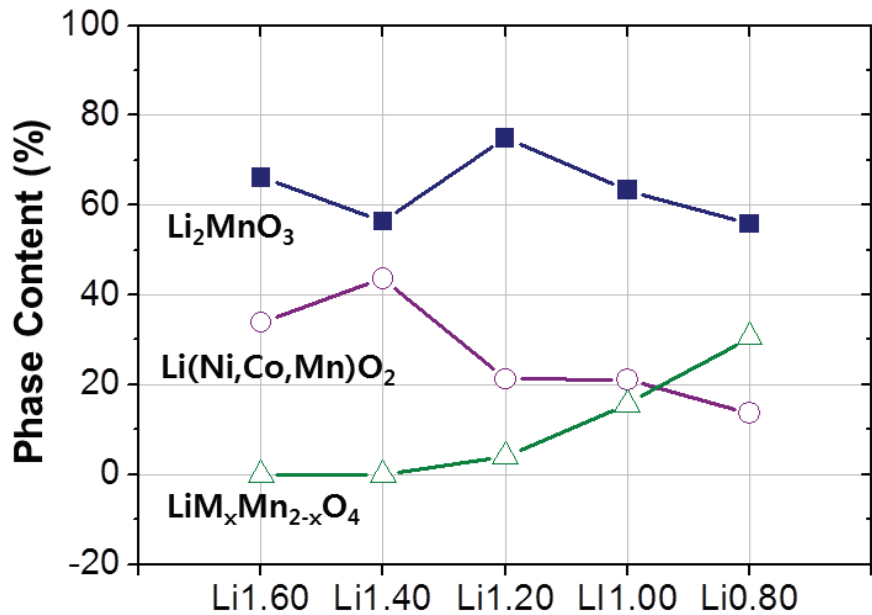


Figure 2.3 Rietveld refinement for the phase contents in Li1.60-Li0.80 compositions. The fractions are calculated with the composite notation like $\text{Li}_2\text{MnO}_3 \cdot \text{Li}(\text{Ni},\text{Co},\text{Mn})\text{O}_2 \cdot \text{LiM}_x\text{Mn}_{2-x}\text{O}_4$ ($\text{M}=\text{Ni, Co, Mn}$).

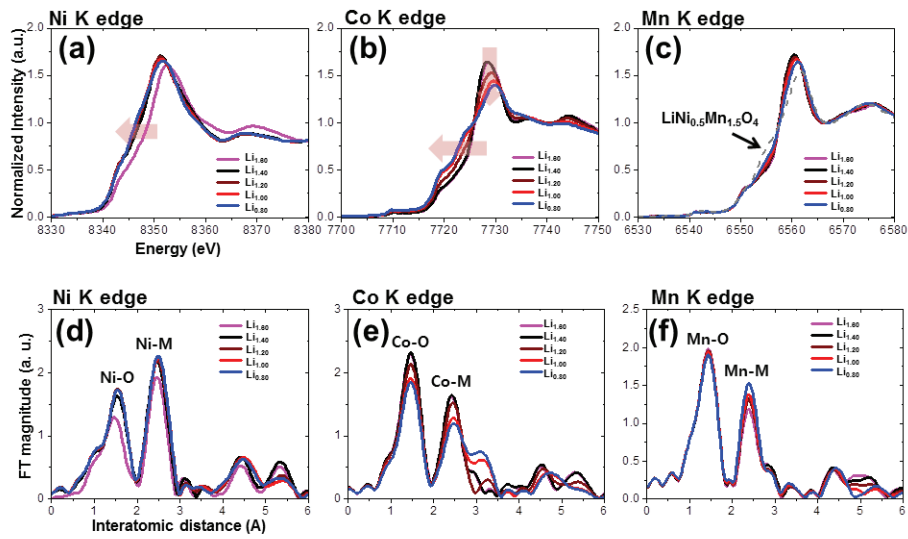


Figure 2.4 XANES spectra of Li_{1.60}-Li_{0.80} compositions at (a) the Ni K-edge, (b) Co K-edge, and (c) Mn K-edge. XAFS spectra at (d) the Ni K-edge, (e) Co K-edge, and (f) Mn K-edge .

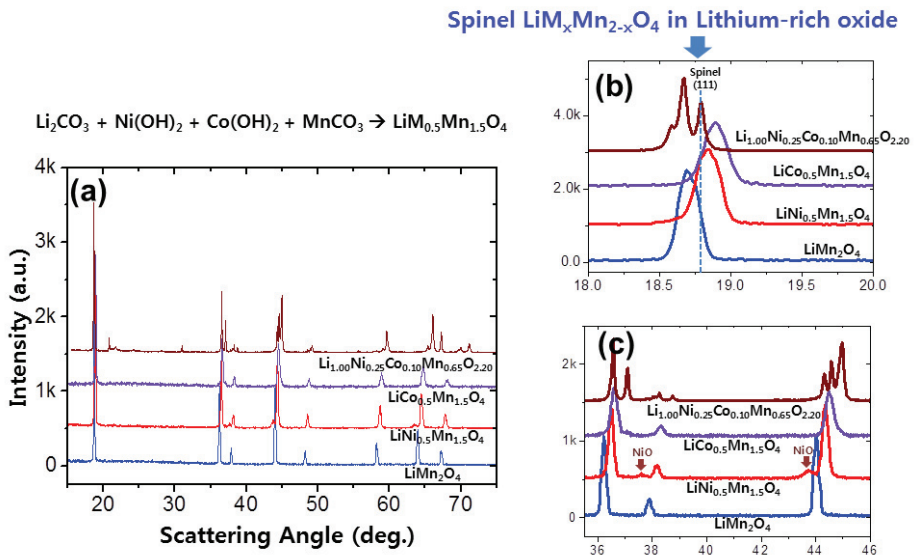


Figure 2.5 (a) XRD patterns of LiMn_2O_4 and $\text{LiNi}_{0.5}\text{Mn}_{1.5}\text{O}_4$ heat-treated at 900degC. (b) and (c) Selected XRD angular range highlighting the difference between LiMn_2O_4 and $\text{LiNi}_{0.5}\text{Mn}_{1.5}\text{O}_4$.

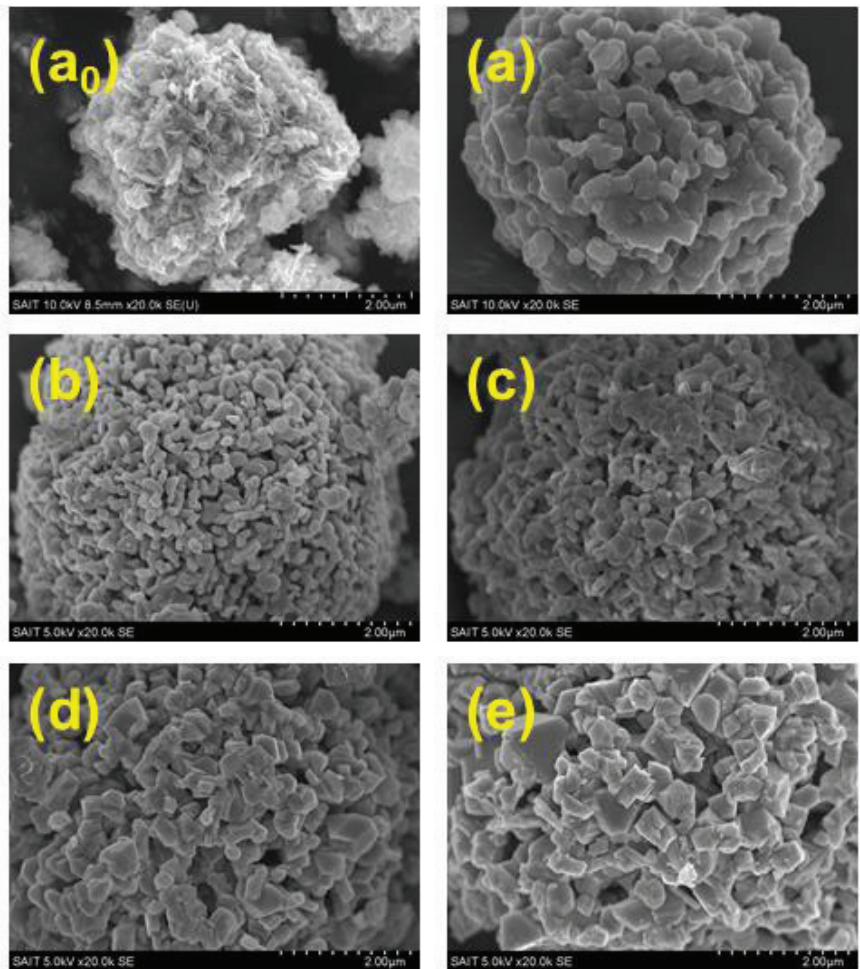


Figure 2.6 FESEM images of (a0) $\text{Ni}_{0.25}\text{Co}_{0.10}\text{Mn}_{0.65}(\text{OH})_2$ precursor and (a)-(e) Li1.60-Li0.80 compositions heat-treated at 900 °C.

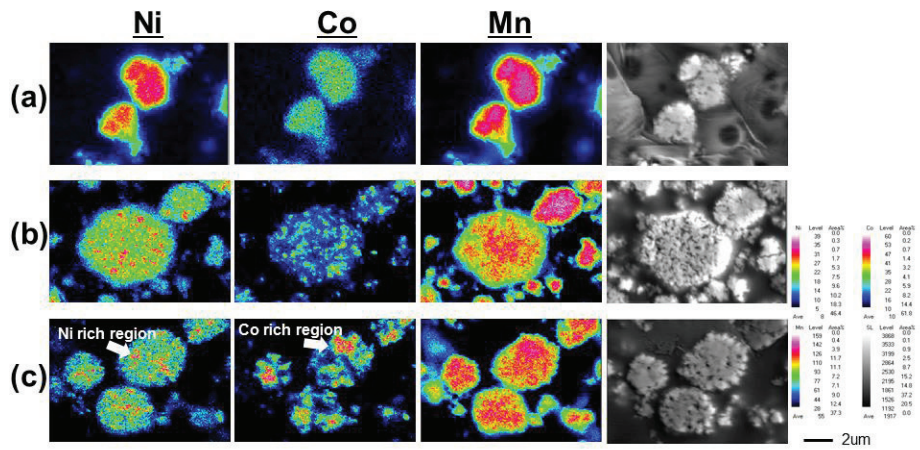


Figure 2.7 Cross-sectional EPMA mapping and images of (a) Li1.40, (b) Li1.20, and (c) Li1.00. A scale bar is located at the lower right corner.

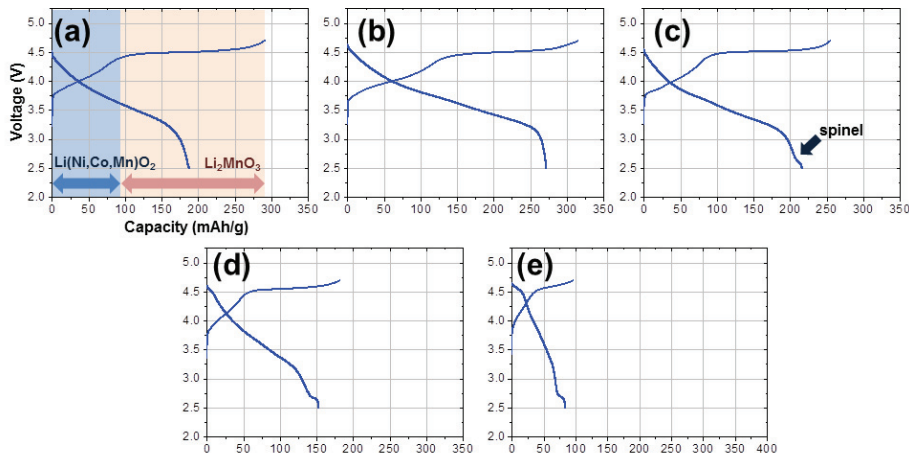


Figure 2.8 a)-(e) Initial charge-discharge profiles measured upon galvanostatic cycle of Li_{1.60}-Li_{0.80} compositions. The data are recorded at 23 mA/g (C/10) rate in the potential range of 2.5-4.7V in coin-type cells with Li counter electrodes.

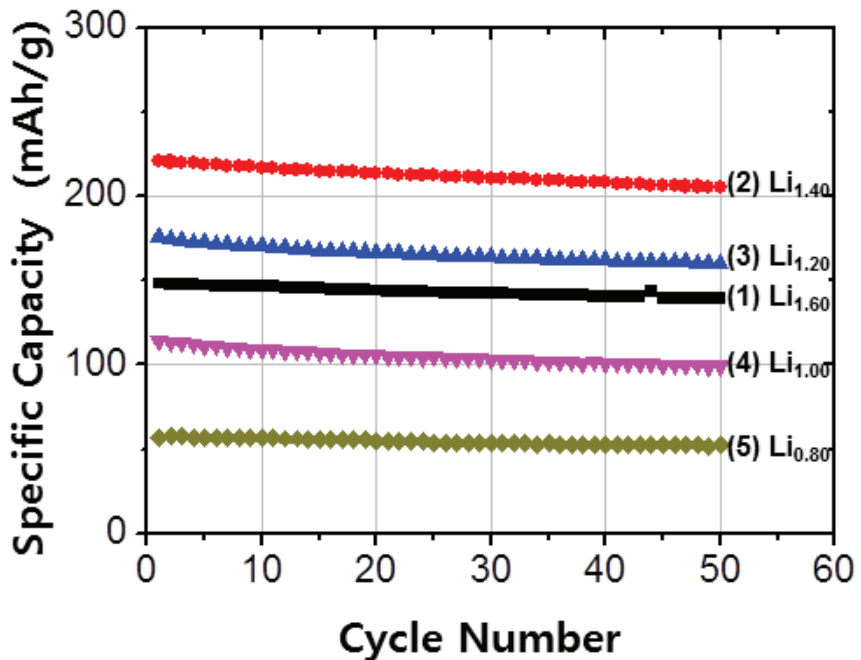


Figure 2.9 Plots of specific capacity vs. cycle number of (1) $\text{Li}_{1.60}$, (2) $\text{Li}_{1.40}$, (3) $\text{Li}_{1.20}$, (4) $\text{Li}_{1.00}$, (5) $\text{Li}_{0.80}$ at 1C rate (230mA/g) in the potential range 2.5-4.6V in coin type cells. Li counter electrodes.

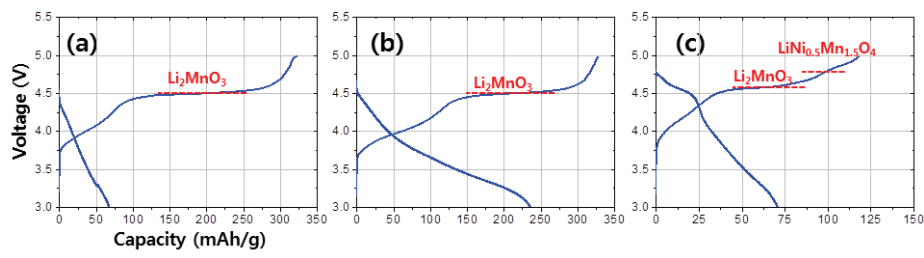


Figure 2.10 Initial charge-discharge profiles measured upon galvanostatic cycle of (a) Li1.60, (b) Li1.40, (c) Li0.80 at 23mA/g (C/10) rate in the potential range of 3.0-5.0V in coin type cells, Li counter electrodes.

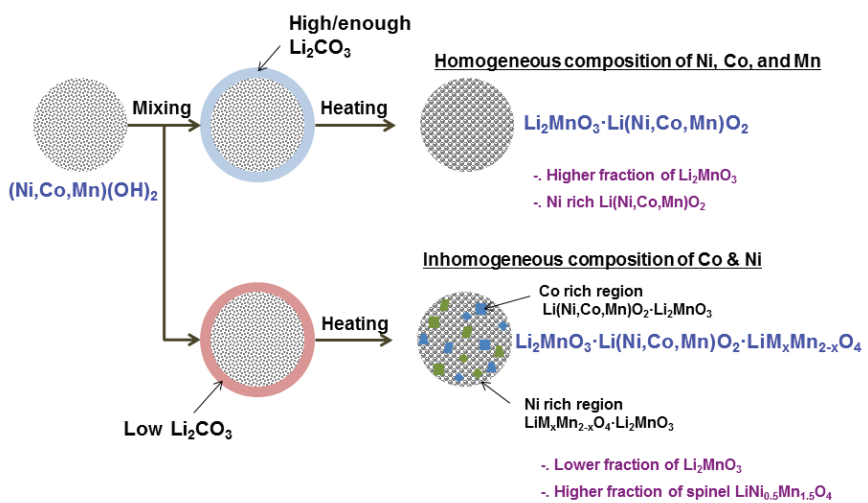


Figure 2.11 Schematic drawing showing the proposed phase evolution process for high and low lithium compositions.

Chapter 3.

Spinel phase composite of lithium-rich oxide

3.1 Introduction

Lithium-rich composite oxide has attracted research focus for a decade due to high discharge capacity, improved safety, and low cost. The high capacity above 250mAh/g come by sacrificing structural stability – oxygen evolution, cation migration, and phase transformation.[4, 52, 53] Commercial exploitation of lithium-rich composite oxide has been challenged and delayed by degradation of the capacity and voltage during charge-discharge cycling.[54] A lot of research activities have been tried to improve the capacity retention and voltage decay in lithium rich oxide. Doping, surface treatment, and composite structure are extensively researched.[4, 55, 56] To prevent phase transition during cycling stable structure is needed.[54] Using another stable phase embedding has a possibility to improve performance. Candidates for stable embedding are spinel phase.[9, 32, 57, 58] To implement spinel phase in lithium-rich composite oxide multiple synthesis techniques are tried, but does not satisfactorily explain the phase evolution and electrochemical performance improvement.[9, 57]

To improve the electrochemical performance spinel embedding composite structure is designed. Spinel types $\text{LiM}_{0.5}\text{Mn}_{1.5}\text{O}_4$ ($\text{M} = \text{Ni, Co, Mn}$) are varied and synthesized by controlling spinel composition and content. Spinel LiMn_2O_4 is widely used for safe battery design.[59] Spinel $\text{LiNi}_{0.5}\text{Mn}_{1.5}\text{O}_4$ is researched for high voltage battery system.[60-63] Spinel $\text{LiCo}_{0.5}\text{Mn}_{1.5}\text{O}_4$ can operate high voltage but isn't researched widely.[64-67]

Lithium-rich oxide with various spinel type is designed and

evaluated for electrochemical performances.

3.2 Experimental Procedure

3.2.1 Synthesis

The $\text{Ni}_{0.25}\text{Co}_{0.10}\text{Mn}_{0.65}(\text{OH})_2$ precursor was prepared through a hydroxide co-precipitation process.[68] Proper amounts of $\text{NiSO}_4 \cdot 6\text{H}_2\text{O}$, $\text{CoSO}_4 \cdot 7\text{H}_2\text{O}$, and $\text{MnSO}_4 \cdot \text{H}_2\text{O}$ were stirred in deionized water to form a homogeneous solution. The solution was chelated using NH_4OH and precipitated with NaOH . The co-precipitated $\text{Ni}_{0.25}\text{Co}_{0.10}\text{Mn}_{0.65}(\text{OH})_2$ after drying was mixed with Li_2CO_3 , MnCO_3 , $\text{Ni}(\text{OH})_2$, and $\text{Co}(\text{OH})_2$ to form the composite material in Figure 3.1.1. Their specific formulae are as follows:



The detailed compositions are as follows :

$$(1-x)[0.4\text{Li}_2\text{MnO}_3 \cdot 0.6\text{LiNi}_{0.417}\text{Co}_{0.167}\text{Mn}_{0.417}\text{O}_2] + x\text{LiM}_{0.5}\text{Mn}_{1.5}\text{O}_4, \quad (x = 0.00/0.02/0.05/0.10/0.20, M = Ni, Co, Mn)$$

The mixed powders were then calcined at 750-900 °C for 10 h in flowing air or oxygen.

3.2.2 Characterization and evaluation

The crystal structures of the powder samples were determined by XRD using Cu K α . Morphology changes of the powders were determined using SEM (S-4700N, Hitachi). The inductively coupled plasma technique (ICP-AES) was

used to determine the ratios of Li, Ni, Co, and Mn elements in each sample. In order to observe the transition metal distributions in the secondary particles, cross sections of the powder particles were prepared by Ar ion milling on a LN₂ cooled stage and measured by an Electron Probe MicroAnalyzer (EPMA, JEOL JXA-8530F). The atomic-level structure and local phases were identified by diffraction and high-resolution TEM (FEI, Titan-cubed 60-300).

The electrodes were prepared by making a slurry of 92 wt% active material ($\text{Li}_2\text{MnO}_3 \cdot \text{Li}(\text{Ni},\text{Co},\text{Mn})\text{O}_2 \cdot \text{LiM}_{0.5}\text{Mn}_{1.5}\text{O}_4$ (M = Ni, Co, Mn)) 4 wt% conductive Denka Black, and 4 wt% polyvinylidene difluoride (PVDF) binder in N-methyl-2-pyrrolidone (NMP) as a solvent. The slurry was coated using doctor-blade method onto Al foil as a current collector. The electrodes were then dried at 120°C in vacuum and pressed. Metallic Li was used as the anode. The electrolyte solution was 1.3 mol L⁻¹ LiPF₆ dissolved in fluoroethylene carbonate and dimethylene carbonate. A porous polyethylene-based membrane was used as a separator. The above components were assembled into CR2032-type coin cells in a dry room. The typical loading of the active mass was 10 mg/cm². The cells were charged to 4.7 V for one cycle and then cycled between 2.5 and 4.6 V vs. Li/Li⁺.

3.2.3 Computational Methods

The first principle calculations were performed using the Vienna ab initio simulation package (VASP) [39, 40] with the Projector-Augmented-Wave (PAW) method. [41] The exchange correlation interactions were included with the generalized gradient approximation Perdew-Burke-Ernzerhof (GGA-PBE) functional, [42] and the plane wave cutoff energy

was set to 500 eV. The structure relaxations were carried out with a criteria of 10-4 eV for the total energy, and 0.02eV/Å for the forces on each atom. The effective on-site Hubbard Ueff corrections were 6.885, 5.95 and 5.0eV on the 3d electrons for Ni, Co and Mn atoms, respectively. [43] The supercells selected in this work contained between 8 and 28 unit cells, depending on the sample composition and structure.

3.3. Results and Discussion

3.3.1 Spinel LiMn_2O_4 composite

The XRD patterns of spinel LiMn_2O_4 embedded samples ($x = 0, 2, 5, 10, 20\text{mol}\%$) heat-treated at 900°C are shown in Figure 3.1.2. In Figure 3.1.2 (a), peaks of the Li_2MnO_3 ($\text{C}2/\text{m}$), $\text{Li}(\text{Ni},\text{Co},\text{Mn})\text{O}_2$ ($\text{R}3^-\text{m}$) phases and the spinel phase $\text{LiM}_x\text{Mn}_{2-x}\text{O}_4$ ($\text{Fd}3^-\text{m}$) ($\text{M} = \text{Ni}$ or Mn) were detected. The composite composition is layered-layered-spinel-spinel ($\text{Li}_2\text{MnO}_3 \cdot \text{Li}(\text{Ni},\text{Co},\text{Mn})\text{O}_2 \cdot \text{LiMn}_2\text{O}_4 \cdot \text{LiNi}_{0.5}\text{Mn}_{1.5}\text{O}_4$). At 10mol% spinel LiMn_2O_4 embedding LiMn_2O_4 (400) peak is discerned, but 20mol% spinel LiMn_2O_4 embedding newly $\text{LiNi}_{0.5}\text{Mn}_{1.5}\text{O}_4$ (400) peak is emerged. Li_2CO_3 and MnCO_3 are consumed to Li_2MnO_3 and spinel phase is changed to lower Mn content spinel type - $\text{LiNi}_{0.5}\text{Mn}_{1.5}\text{O}_4$ in 20mol% composition. The intensity of Li_2MnO_3 superlattice peak in 20-25deg is increased in 20mol% compared to designed composition. As spinel phase is increased, Li_2MnO_3 content has to be decreased in composition design. The phase evolution mechanism is discussed in Session 3.3.3 in more detail.

Figure 3.1.3 shows SEM images of spinel LiMn_2O_4 embedded samples ($x = 0, 2, 5, 10, 20\text{mol\%}$) heat-treated at 900°C . After heat treatment, the primary particles grew into spheres with faceted morphology. The smallest primary particles, approximately 200 nm in size, occurred in spinel LiMn_2O_4 0.0mol% composition. At higher spinel LiMn_2O_4 content (20mol%), the size increased to 1um (Figure 3.1.3 (e)), which could be attributed to the Li_2CO_3 and MnCO_3 phase which acts as a flux medium to promote the grain growth. At higher spinel LiMn_2O_4 contents, the primary particles were larger and octahedral-shaped (Figure 3.1.3 (b)-(e)).

Figure 3.1.4 shows the charge-discharge profiles at the first cycle, i.e. activation at 4.7 V. The cells delivered discharge capacities of 278, 261, 257, 214 and $119 \text{ mAh}\cdot\text{g}^{-1}$ with spinel $\text{LiMn}_2\text{O}_4 = 0, 2, 5, 10$, and 20mol\% cathode materials, respectively. Table 3.1.1 lists the rate capabilities of these compositions. The specific capacity vs. cycle number results are also shown in Table 3.1.1. The higher spinel LiMn_2O_4 content shows the lower capacity and cycle performance. The growth of primary particle size during high temperature condition(900degC) limits lithium ion diffusion during charge-discharge even though spinel embedding improves structure stability. During charging all the compositions display a plateau around 4.5V, which is known as the activation region of Li_2MnO_3 ($\text{C}2/\text{m}$) phase found at all spinel LiMn_2O_4 levels (Figure 3.1.4). In spinel LiMn_2O_4 10mol%, the plateau around 2.7 V during discharging is related to the electrochemical reaction of the spinel phase. This plateau remains visible in spinel LiMn_2O_4 10 and 20mol%.

The XRD patterns of spinel LiMn_2O_4 embedded samples ($x = 0, 2,$

5, 10, 20mol%) heat-treated at 750°C are shown in Figure 3.1.5. In Figure 3.1.5 (a), peaks of the Li_2MnO_3 ($\text{C}2/\text{m}$), $\text{Li}(\text{Ni},\text{Co},\text{Mn})\text{O}_2$ ($\text{R}\bar{3}-\text{m}$) phases and the spinel phase $\text{LiM}_{\text{x}}\text{Mn}_{2-\text{x}}\text{O}_4$ ($\text{Fd}\bar{3}-\text{m}$) ($\text{M} = \text{Ni}$ or Mn) were detected. The composite composition is layered-layered-spinel-spinel ($\text{Li}_2\text{MnO}_3 \cdot \text{Li}(\text{Ni},\text{Co},\text{Mn})\text{O}_2 \cdot \text{LiMn}_2\text{O}_4 \cdot \text{LiNi}_{0.5}\text{Mn}_{1.5}\text{O}_4$) the same as heat-treated at 900°C. The intensity of Li_2MnO_3 superlattice peak in 22deg is increased as spinel contents are increased in designed compositions.

Figure 3.1.6 shows SEM images of spinel LiMn_2O_4 embedded samples ($\text{x} = 0, 2, 5, 10, 20\text{mol\%}$) heat-treated at 750°C At higher spinel LiMn_2O_4 content (20mol%), the size is the same as lower spinel content, which could be attributed to low temperature for grain growth.

Table 3.1.2 lists the rate capabilities of these compositions. The specific capacity vs. cycle number results are also shown in Table 3.1.2. The higher spinel LiMn_2O_4 content (20mol%) shows the lower capacity (190mAh/g at 0.1C) and cycle performance (74.1% at 50th). At spinel LiMn_2O_4 content (2mol%) the cycle performances are improved. Capacity retention after 50th cycle is 90.6%, and voltage decay -55mV. The spinel embedded structure improved the structure stability during charge-discharge at small primary particle morphology.

Table 3.1.1 Electrochemical performance tests of spinel (1) 0, (2) 2, (3) 5, (4) 10, and (5) 20mol% heat-treated at 900degC at different currents (C rates) in the potential range 2.5-4.6/4.7V in coin type cells. Li counter electrodes.

	1st cycle			Discharge Rate @0.5C Cha				Cycle Life (50 th)	
	0.1C Cha mAh/g	0.1C Dis mAh/g	eff. %	0.2C mAh/g	1C Dis mAh/g	2C Dis mAh/g	2C vs. 0.2C	CRR (%)	Voltage Decay (mV)
(1) x=0.00	327	278	85.20	257	231	214	83.40%	95.3	-67
(2) x=0.02	302	261	86.40	243	215	200	82.20%	87.7	-81
(3) x=0.05	291	257	88.40	241	211	190	78.70%	86.3	-74
(4) x=0.10	250	214	85.50	216	184	165	76.20%	89	-78
(5) x=0.20	133	119	90.00	130	129	117	89.90%	86.3	-118

• Based on capacity 230mAh/g, 90:5=(Active Material):DB:PVDF, Charge : 4.70/4.60V, Discharge : 2.5V,

* (1-x)[0.4Li₂MnO₃·0.6LiNi_{0.417}Co_{0.167}Mn_{0.417}O₂] xLiMn₂O₄

Table 3.1.2 Electrochemical performance tests of spinel (1) 0, (2) 2, (3) 5, (4) 10, and (5) 20mol% heat-treated at 750degC at different currents (C rates) in the potential range 2.5-4.6/4.7V in coin type cells. Li counter electrodes.

	1st cycle			Discharge Rate @0.5C Cha				Cycle Life (50 th)	
	0.1C Cha mAh/g	0.1C Dis mAh/g	eff. %	0.2C mAh/g	1C Dis mAh/g	2C Dis mAh/g	2C vs. 0.2C	CRR (%)	Voltage Decay (mV)
(1) x=0.00	319	270	84.80	252	229	215	85.60%	88.4	-75
(2) x=0.02	288	258	89.60	248	222	204	82.40%	90.6	-55
(3) x=0.05	279	251	90.10	240	209	186	77.60%	87.9	-52
(4) x=0.10	252	222	88.00	213	190	172	80.70%	87.7	-58
(5) x=0.20	195	190	97.10	179	168	156	87.50%	74.1	-90

• Based on capacity 230mAh/g, 90:5:5=(Active Material):DB:PVDF, Charge : 4.70/4.60V, Discharge : 2.5V,

* $(1-x)[0.4\text{Li}_2\text{MnO}_3 \cdot 0.6\text{LiNi}_{0.417}\text{Co}_{0.167}\text{Mn}_{0.417}\text{O}_2]_x\text{LiMn}_2\text{O}_4$

[Synthesis Procedure]

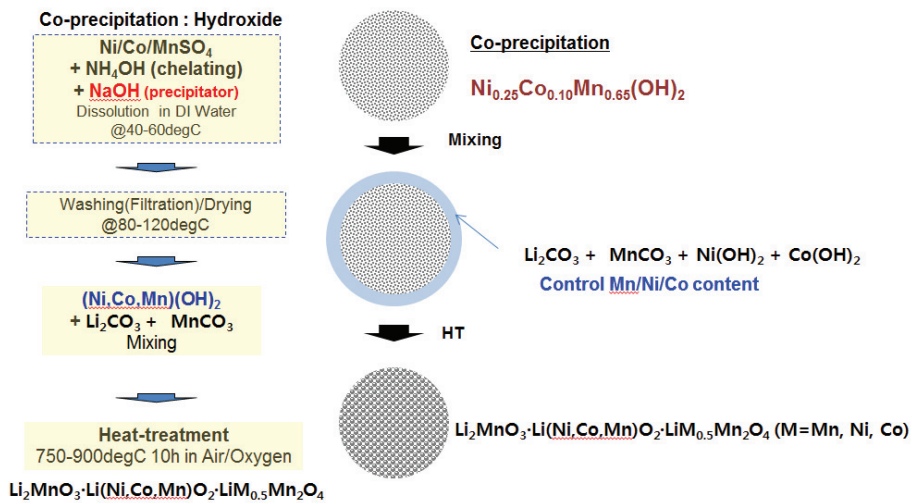


Figure 3.1.1 Synthesis procedure for spinel composite oxide

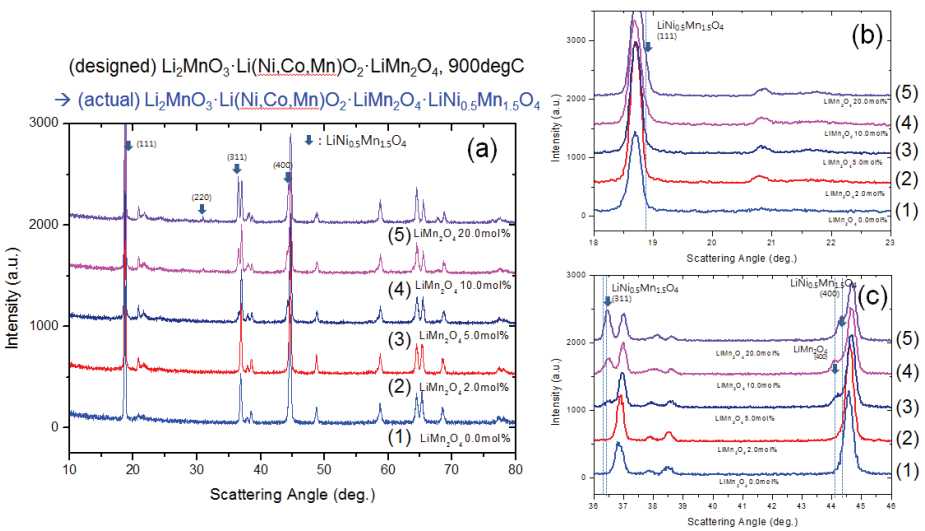


Figure 3.1.2 (a) Panels (1)-(5) are XRD patterns of spinel 0, 2, 5, 10, and 20mol% respectively, after heat-treatment at 900 °C. Selected angular ranges highlight the (b) layered and (c) spinel peaks.

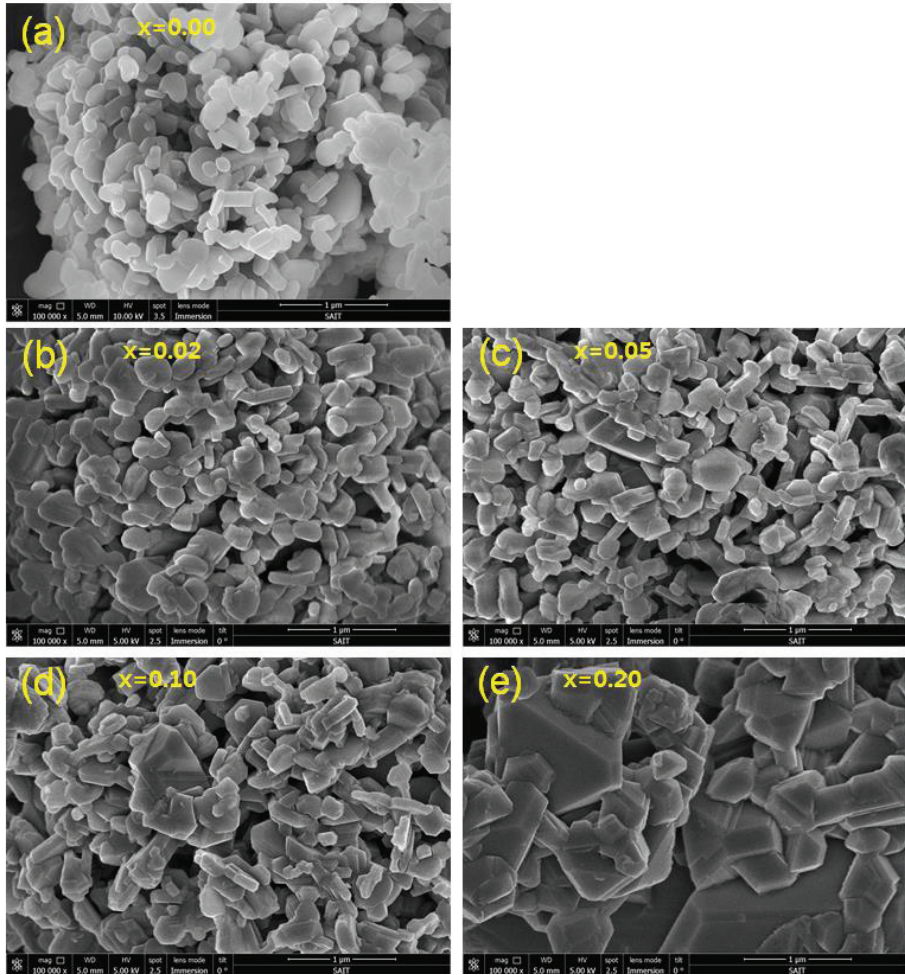


Figure 3.1.3 FESEM images of spinel composites (a) 0, (b) 2, (c) 5, (d) 10, and (e) 20mol% heat-treated at 900 °C.

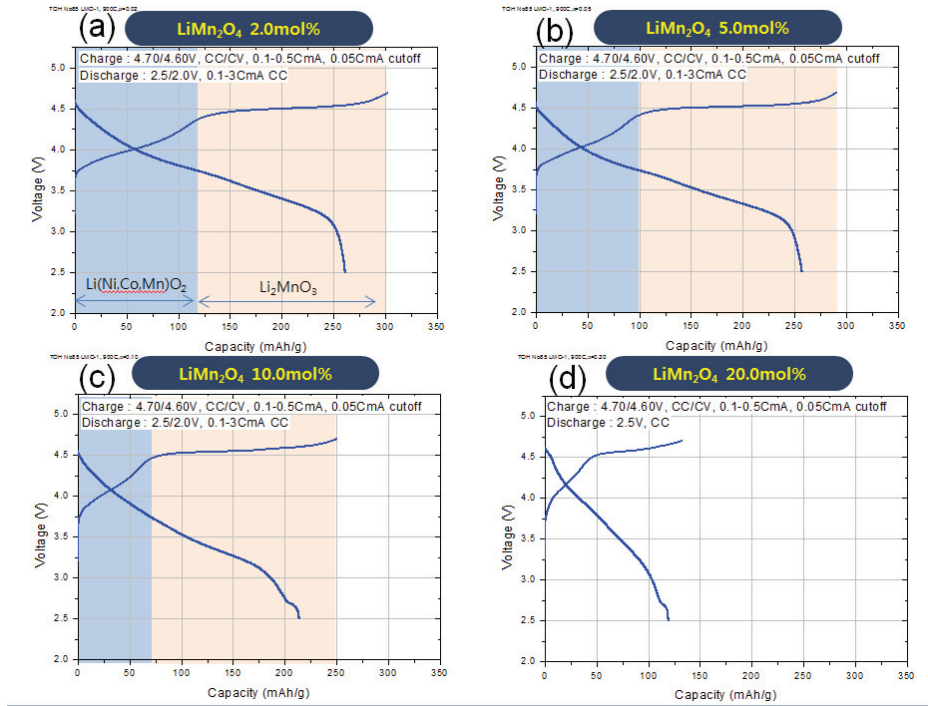


Figure 3.1.4 (a)-(d) Initial charge-discharge profiles measured upon galvanostatic cycle of spinel 0-20mol% compositions heat-treated at 900degC. The data are recorded at 23 mA/g (C/10) rate in the potential range of 2.5-4.7V in coin-type cells with Li counter electrodes.

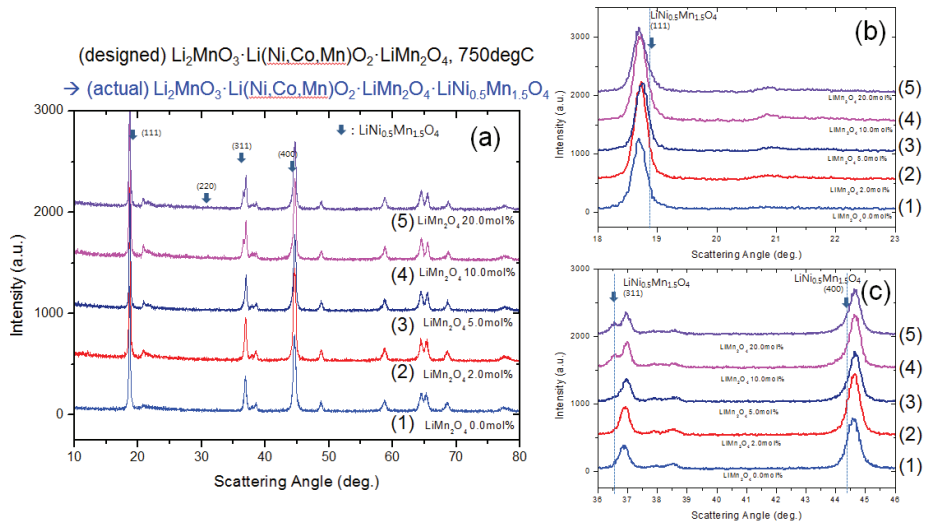


Figure 3.1.5 (a) Panels (1)-(5) are XRD patterns of spinel 0, 2, 5, 10, and 20mol% respectively, after heat-treatment at 750 °C. Selected angular ranges highlight the (b) layered and (c) spinel peaks.

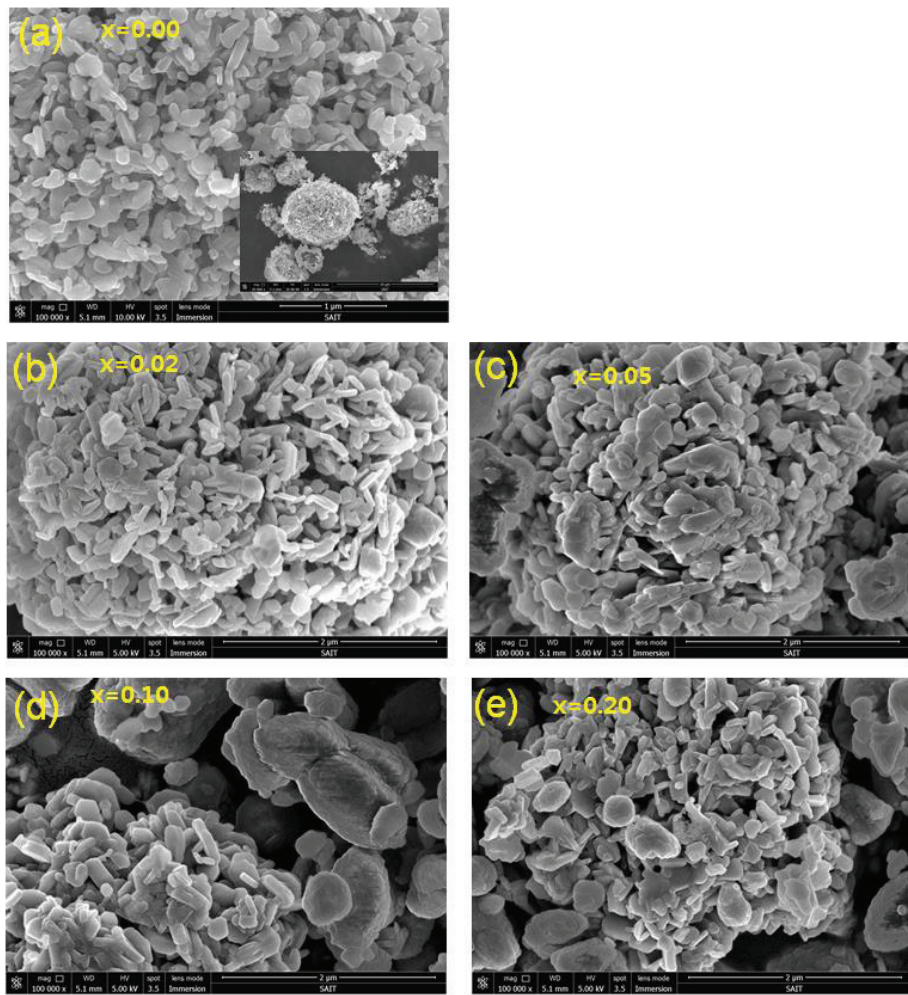


Figure 3.1.6 FESEM images of spinel composites (a) 0, (b) 2, (c) 5, (d) 10, and (e) 20mol% heat-treated at 750 °C..

3.3.2 Spinel $\text{LiNi}_{0.5}\text{Mn}_{1.5}\text{O}_4$ composite

The XRD patterns of spinel $\text{LiNi}_{0.5}\text{Mn}_{1.5}\text{O}_4$ embedded samples ($x = 0, 2, 5, 10, 20\text{mol\%}$) heat-treated at 900°C in air are shown in Figure 3.2.1. In Figure 3.2.1 (a), peaks of the Li_2MnO_3 ($\text{C}2/\text{m}$), $\text{Li}(\text{Ni},\text{Co},\text{Mn})\text{O}_2$ ($\text{R}3^-\text{m}$) phases and the spinel phase $\text{LiM}_x\text{Mn}_{2-x}\text{O}_4$ ($\text{Fd}3^-\text{m}$) ($M = \text{Ni}$) are detected. The rocksalt NiO is also detected. The composite composition is layered-layered-spinel-rocksalt ($\text{Li}_2\text{MnO}_3 \cdot \text{Li}(\text{Ni},\text{Co},\text{Mn})\text{O}_2 \cdot \text{LiNi}_{0.5}\text{Mn}_{1.5}\text{O}_4 \cdot \text{NiO}$).

The XRD patterns of spinel $\text{LiNi}_{0.5}\text{Mn}_{1.5}\text{O}_4$ embedded samples ($x = 0, 2, 5, 10, 20\text{mol\%}$) heat-treated at 750°C in air are shown in Figure 3.2.2. In Figure 3.2.2 (a), peaks of the Li_2MnO_3 ($\text{C}2/\text{m}$), $\text{Li}(\text{Ni},\text{Co},\text{Mn})\text{O}_2$ ($\text{R}3^-\text{m}$) phases and the spinel phase $\text{LiM}_x\text{Mn}_{2-x}\text{O}_4$ ($\text{Fd}3^-\text{m}$) ($M = \text{Ni}$) are detected. The rocksalt NiO is detected. The composite composition is layered-layered-spinel-rocksalt ($\text{Li}_2\text{MnO}_3 \cdot \text{Li}(\text{Ni},\text{Co},\text{Mn})\text{O}_2 \cdot \text{LiNi}_{0.5}\text{Mn}_{1.5}\text{O}_4 \cdot \text{NiO}$).

The XRD patterns of spinel $\text{LiNi}_{0.5}\text{Mn}_{1.5}\text{O}_4$ embedded samples ($x = 0, 2, 5, 10, 20\text{mol\%}$) heat-treated at 900°C in oxygen are shown in Figure 3.2.3. In Figure 3.2.3 (a), peaks of the Li_2MnO_3 ($\text{C}2/\text{m}$), $\text{Li}(\text{Ni},\text{Co},\text{Mn})\text{O}_2$ ($\text{R}3^-\text{m}$) phases and the spinel phase $\text{LiM}_x\text{Mn}_{2-x}\text{O}_4$ ($\text{Fd}3^-\text{m}$) ($M = \text{Ni}$) are detected. The rocksalt NiO is detected. The rocksalt NiO phase heat-treated at 900degC in oxygen is decreased compared with air atmosphere. The composite composition is layered-layered-spinel-rocksalt ($\text{Li}_2\text{MnO}_3 \cdot \text{Li}(\text{Ni},\text{Co},\text{Mn})\text{O}_2 \cdot \text{LiNi}_{0.5}\text{Mn}_{1.5}\text{O}_4 \cdot \text{NiO}$).

The XRD patterns of spinel $\text{LiNi}_{0.5}\text{Mn}_{1.5}\text{O}_4$ embedded samples ($x = 0, 2, 5, 10, 20\text{mol\%}$) heat-treated at 750°C in oxygen are shown in Figure 3.2.4. In Figure 3.2.4 (a), peaks of the Li_2MnO_3 ($\text{C}2/\text{m}$), $\text{Li}(\text{Ni},\text{Co},\text{Mn})\text{O}_2$ ($\text{R}3^-\text{m}$) phases and the spinel phase $\text{LiM}_x\text{Mn}_{2-x}\text{O}_4$ ($\text{Fd}3^-\text{m}$) ($M = \text{Ni}$) are

detected. The rocksalt NiO is detected. The rocksalt NiO phase heat-treated at 750degC in oxygen is the same as air atmosphere. The composite composition is layered-layered-spinel-rocksalt ($\text{Li}_2\text{MnO}_3 \cdot \text{Li}(\text{Ni},\text{Co},\text{Mn})\text{O}_2 \cdot \text{LiNi}_{0.5}\text{Mn}_{1.5}\text{O}_4 \cdot \text{NiO}$).

Figure 3.2.5 shows the charge-discharge profiles at the first cycle, i.e. activation at 4.7 V. The cells delivered discharge capacities of 278, 266, 262, 232 and 169 $\text{mAh} \cdot \text{g}^{-1}$ with spinel $\text{LiNi}_{0.5}\text{Mn}_{1.5}\text{O}_4$ 0, 2, 5, 10, and 20mol% cathode materials, respectively. Table 3.2.1 lists the rate capabilities of these compositions. The specific capacity vs. cycle number results are also shown in Table 3.2.1. The higher spinel $\text{LiNi}_{0.5}\text{Mn}_{1.5}\text{O}_4$ content shows the lower capacity and cycle performance. The growth of primary particle size during high temperature condition(900degC) limits lithium ion diffusion during charge-discharge even though spinel embedding improves structure stability. During charging all the compositions display a plateau around 4.5 V , which is known as the activation region of (C2/m) phase found at all spinel $\text{LiNi}_{0.5}\text{Mn}_{1.5}\text{O}_4$ levels (Figure 3.2.5). In spinel $\text{LiNi}_{0.5}\text{Mn}_{1.5}\text{O}_4$ 20mol%, the plateau around 2.7 V during discharging is related to the electrochemical reaction of the spinel phase. This plateau is only visible in spinel $\text{LiNi}_{0.5}\text{Mn}_{1.5}\text{O}_4$ 20mol%.

The specific capacity vs. cycle number results are also shown in Table 3.2.1. The higher spinel $\text{LiNi}_{0.5}\text{Mn}_{1.5}\text{O}_4$ content (20mol%) shows the lower capacity (169mAh/g at 0.1C) and cycle performance (87.5% at 50th). At spinel $\text{LiNi}_{0.5}\text{Mn}_{1.5}\text{O}_4$ content (5mol%) the voltage decay is improved. Capacity retention after 50th cycle is 92.7%, and voltage decay -55mV. The spinel embedded structure improved the structure stability during charge-

discharge.

Table 3.2.1 Electrochemical performance tests of spinel (1) 0, (2) 2, (3) 5, (4) 10, and (5) 20mol% heat-treated at 900degC in air at different currents (C rates) in the potential range 2.5-4.6/4.7V in coin type cells. Li counter electrodes.

	1st cycle			Discharge Rate @0.5C Cha				Cycle Life (50 th)	
	0.1C Cha mAh/g	0.1C Dis mAh/g	eff. %	0.2C mAh/g	1C Dis mAh/g	2C Dis mAh/g	2C vs. 0.2C	CRR (%)	Voltage Decay (mV)
(1) x=0.00	327	278	85.20	257	231	214	83.40%	95.3	-67
(2) x=0.02	307	266	86.50	248	225	212	85.50%	92.8	-72
(3) x=0.05	296	262	88.50	245	219	205	83.70%	92.7	-55
(4) x=0.10	269	232	86.10	220	197	184	83.60%	88.8	-60
(5) x=0.20	194	169	87.20	172	160	146	84.80%	87.5	-67

• Based on capacity 230mAh/g, 90:5:5=(Active Material):DB:PVDF, Charge : 4.70/4.60V, Discharge : 2.5V,

* $(1-x)[0.4\text{Li}_2\text{MnO}_3 \cdot 0.6\text{LiNi}_{0.417}\text{Co}_{0.167}\text{Mn}_{0.417}\text{O}_2]_x\text{LiMn}_2\text{O}_4$

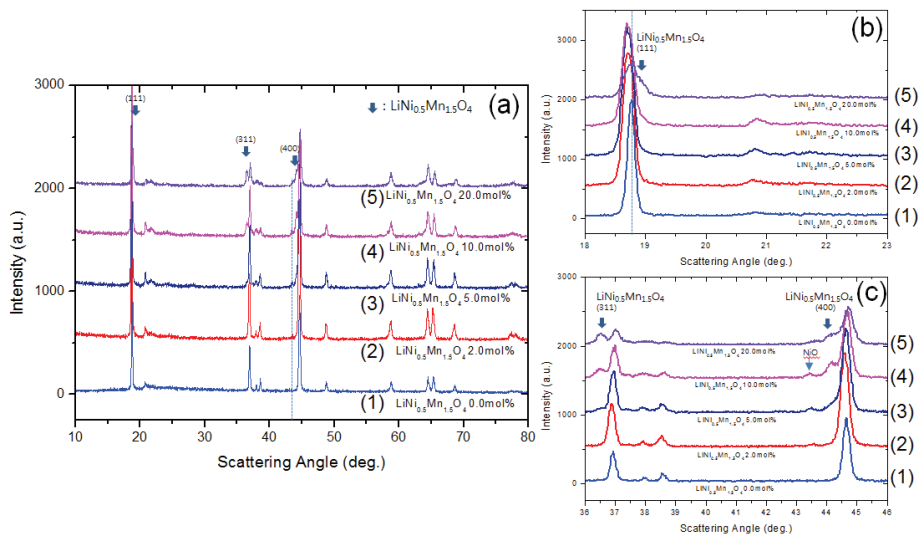


Figure 3.2.1 (a) Panels (1)-(5) are XRD patterns of spinel 0, 2, 5, 10, and 20mol% respectively, after heat-treatment at 900 °C in air. Selected angular ranges highlight the (b) layered and (c) spinel peaks.

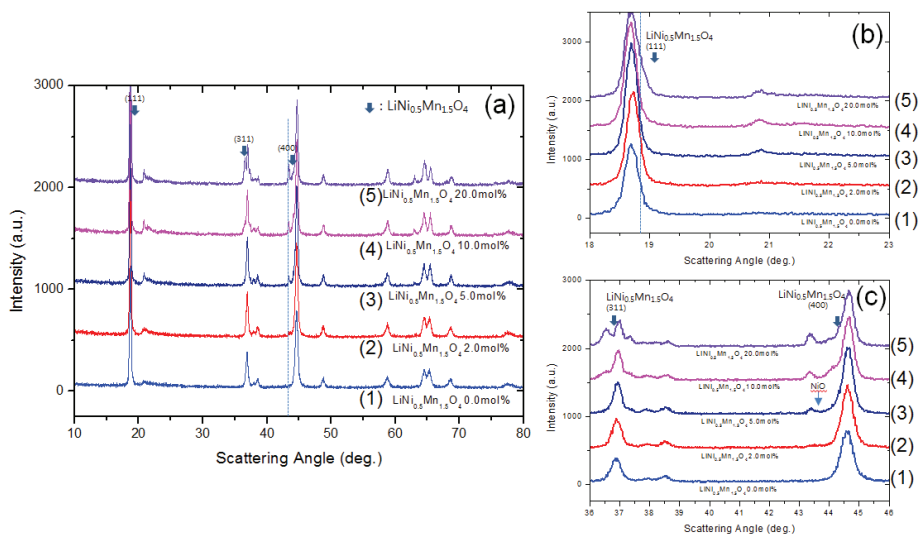


Figure 3.2.2 (a) Panels (1)-(5) are XRD patterns of spinel 0, 2, 5, 10, and 20mol% respectively, after heat-treatment at 750 °C in air. Selected angular ranges highlight the (b) layered and (c) spinel peaks.

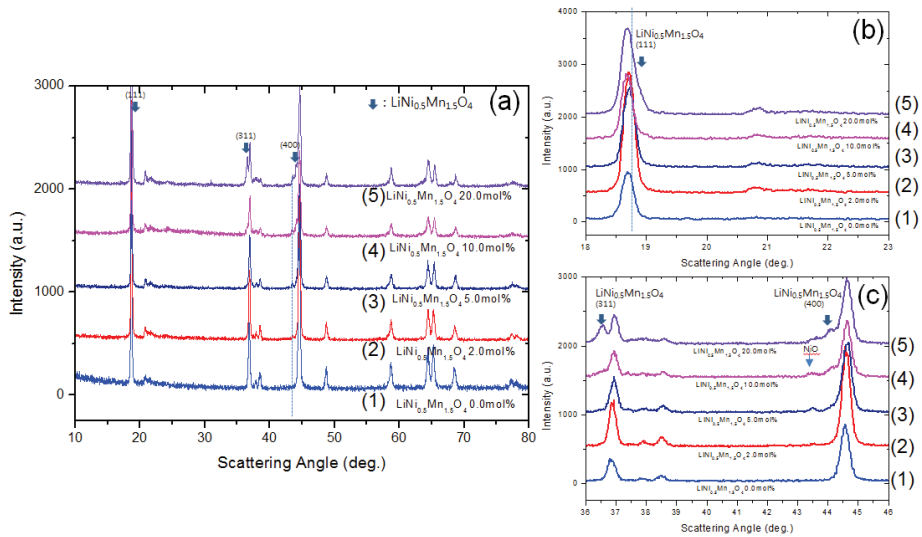


Figure 3.2.3 (a) Panels (1)-(5) are XRD patterns of spinel 0, 2, 5, 10, and 20mol% respectively, after heat-treatment at 900 °C in oxygen. Selected angular ranges highlight the (b) layered and (c) spinel peaks.

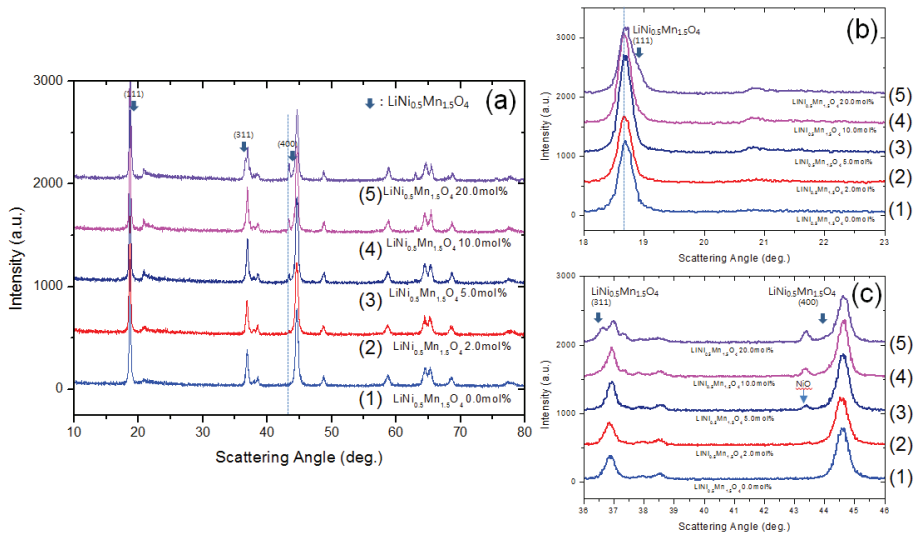


Figure 3.2.4 (a) Panels (1)-(5) are XRD patterns of spinel 0, 2, 5, 10, and 20mol% respectively, after heat-treatment at 750 °C in oxygen. Selected angular ranges highlight the (b) layered and (c) spinel peaks.

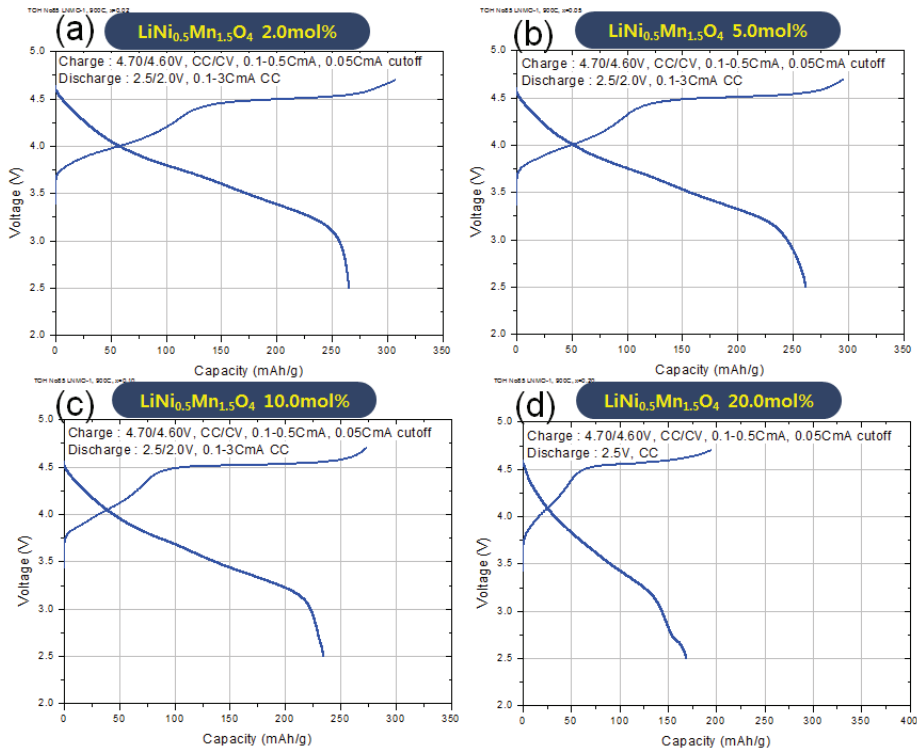


Figure 3.2.5 (a)-(d) Initial charge-discharge profiles measured upon galvanostatic cycle of spinel 0-20mol% compositions heat-treated at 900degC in air. The data are recorded at 23 mA/g (C/10) rate in the potential range of 2.5-4.7V in coin-type cells with Li counter electrodes.

3.3.3 Spinel $\text{LiCo}_{0.5}\text{Mn}_{1.5}\text{O}_4$ composite

The XRD patterns of spinel $\text{LiCo}_{0.5}\text{Mn}_{1.5}\text{O}_4$ embedded samples ($x = 0, 2, 5, 10, 20\text{mol\%}$) heat-treated at 900°C are shown in Figure 3.3.1. In Figure 3.3.1 (a), peaks of the Li_2MnO_3 ($\text{C}2/\text{m}$), $\text{Li}(\text{Ni},\text{Co},\text{Mn})\text{O}_2$ ($\text{R}3^-\text{m}$) phases and the spinel phase $\text{LiM}_x\text{Mn}_{2-x}\text{O}_4$ ($\text{Fd}3^-\text{m}$) ($M = \text{Co}$) were detected. Layered Li_2MnO_3 ($\text{C}2/\text{m}$) phase can be distinguished in $20.5\text{--}21^\circ$ range in Figure 3.3.1, and is named “ Li_2MnO_3 -like super-lattice peak”. These peaks exist in all compositions studied here. The composite composition is layered-layered-spinel ($\text{Li}_2\text{MnO}_3 \cdot \text{Li}(\text{Ni},\text{Co},\text{Mn})\text{O}_2 \cdot \text{LiCo}_{0.5}\text{Mn}_{1.5}\text{O}_4$).

The Rietveld refinement with XRD data was performed in order to clarify the phase contents and crystalline structures in the powder samples. Table 3.3.2 summarizes the lattice parameters and crystal sizes of Li_2MnO_3 ($\text{C}2/\text{m}$), $\text{Li}(\text{Ni},\text{Co},\text{Mn})\text{O}_2$ ($\text{R}3^-\text{m}$), and $\text{LiM}_x\text{Mn}_{2-x}\text{O}_4$ ($\text{Fd}3^-\text{m}$) ($M = \text{Co}$). The crystal sizes are increased as spinel $\text{LiCo}_{0.5}\text{Mn}_{1.5}\text{O}_4$ content is increased. The phase contents were calculated from the main and characterized peaks of each phase in Figure 3.3.2. None of the samples could be assigned to a single phase structure; instead they were composites of two or three phases. As spinel $\text{LiCo}_{0.5}\text{Mn}_{1.5}\text{O}_4$ content is increased, the phase content of $\text{Li}(\text{Ni},\text{Co},\text{Mn})\text{O}_2$ ($\text{R}3^-\text{m}$) is decreased and Li_2MnO_3 ($\text{C}2/\text{m}$) is slightly increased. The larger phase content of Li_2MnO_3 phase might be exaggerated, though. This is because Li_2MnO_3 has a higher degree of crystallinity than the other phases due to the high temperature calcination.[69]

Figure 3.3.3 shows SEM images of spinel $\text{LiCo}_{0.5}\text{Mn}_{1.5}\text{O}_4$ embedded samples ($x = 0, 2, 5, 10, 20\text{mol\%}$) heat-treated at 900°C . After heat treatment, the primary particles grew into spheres with faceted

morphology. The smallest primary particles, approximately 200 nm in size, occurred in spinel $\text{LiCo}_{0.5}\text{Mn}_{1.5}\text{O}_4$ 0.0mol% composition. At higher spinel $\text{LiCo}_{0.5}\text{Mn}_{1.5}\text{O}_4$ content (20mol%), the size increased to 1um (Figure 3.3.3 (c)), which could be attributed to the Co(OH)_2 and MnCO_3 phase which act as a flux medium. At higher spinel $\text{LiCo}_{0.5}\text{Mn}_{1.5}\text{O}_4$ contents, the primary particles were larger and octahedral-shaped (Figure 3.3.3 (c)).

Figure 3.3.4 shows the EPMA composition mapping data. EPMA is generally used to determine the compositional distribution of transition metals. The powders were molded in epoxy and Ar ion-milled to reveal the vertical section of particles. At high spinel $\text{LiCo}_{0.5}\text{Mn}_{1.5}\text{O}_4$ content (20mol%), separate Ni-rich and Co-rich regions formed inside a single particle. Mn, on the other hand, was uniformly distributed. Different diffusional mobilities and composition differences of Ni, Co and Mn in $\text{Ni}_{0.25}\text{Co}_{0.10}\text{Mn}_{0.65}(\text{OH})_2$ precursor might cause the segregation during the heat treatment at high spinel $\text{LiCo}_{0.5}\text{Mn}_{1.5}\text{O}_4$ level.[34, 70-72] The segregated Co induced by spinel $\text{LiCo}_{0.5}\text{Mn}_{1.5}\text{O}_4$ (raw material - Co(OH)_2 and MnCO_3) promotes particle growth.

Co and Ni segregations were also visible from the HAADF image and EDS mapping of Co and Ni, as shown in Figure 3.3.5. The composite structures of layered and spinel phases are also identified in high-resolution TEM results, as shown in Figure 3.3.5 (d). The row of spots indicated by the white arrow in Figure 3.3.5 (d) corresponds to the spinel phase, which is integrated with layered phase at the nanometer scale to form the composite structure.

Figure 3.3.6 shows Mn XPS spectra for spinel $\text{LiNi}_{0.5}\text{Mn}_{1.5}\text{O}_4$ and

$\text{LiCo}_{0.5}\text{Mn}_{1.5}\text{O}_4$ (20mol%) embedded samples. The major peak centered at 642.2eV corresponds to Mn^{4+} and the minor one at 641.0eV corresponds to Mn^{3+} ions in the composite oxide. XPS result shows that spinel $\text{LiCo}_{0.5}\text{Mn}_{1.5}\text{O}_4$ embedded oxide increases Mn^{3+} compared to spinel $\text{LiCo}_{0.5}\text{Mn}_{1.5}\text{O}_4$ embedding.

Table 3.3.1 lists the rate capabilities of these compositions. The specific capacity vs. cycle number results are also shown in Table 3.3.1. The higher spinel $\text{LiCo}_{0.5}\text{Mn}_{1.5}\text{O}_4$ content shows the lower capacity and cycle performance. The growth of primary particle size during high temperature condition(900degC) limits lithium ion diffusion during charge-discharge even though spinel embedding improves structure stability. The initial coulombic efficiencies are improved by embedding spinel $\text{LiCo}_{0.5}\text{Mn}_{1.5}\text{O}_4$.

The XRD patterns of spinel $\text{LiCo}_{0.5}\text{Mn}_{1.5}\text{O}_4$ embedded samples ($x = 0, 2, 5, 10, 20\text{mol\%}$) heat-treated at 750°C are shown in Figure 3.3.7. In Figure 3.3.7 (a), peaks of the Li_2MnO_3 ($\text{C}2/\text{m}$), $\text{Li}(\text{Ni},\text{Co},\text{Mn})\text{O}_2$ ($\text{R}3^-\text{m}$) phases and the spinel phase $\text{LiM}_x\text{Mn}_{2-x}\text{O}_4$ ($\text{Fd}3^-\text{m}$) ($\text{M} = \text{Co}$) were detected. The composite composition is layered-layered-spinel ($(\text{Li}_2\text{MnO}_3 \cdot \text{Li}(\text{Ni},\text{Co},\text{Mn})\text{O}_2 \cdot \text{LiCo}_{0.5}\text{Mn}_{1.5}\text{O}_4)$).

Figure 3.3.8 shows SEM images of spinel $\text{LiCo}_{0.5}\text{Mn}_{1.5}\text{O}_4$ embedded samples ($x = 0, 5, 20\text{mol\%}$) heat-treated at 750°C. At higher spinel $\text{LiCo}_{0.5}\text{Mn}_{1.5}\text{O}_4$ content (20mol%), the size is the same as lower spinel content, which could be attributed to low temperature for grain growth. The smallest primary particles, approximately 200 nm in size, occurred in spinel $\text{LiCo}_{0.5}\text{Mn}_{1.5}\text{O}_4$ 0.0mol% composition.

Figure 3.3.9 shows the EPMA composition mapping data heat-

treated at 750degC. At high spinel $\text{LiCo}_{0.5}\text{Mn}_{1.5}\text{O}_4$ content (20mol%), separate Ni-rich and Co-rich regions formed inside a single particle.

Table 3.3.3 lists the rate capabilities of these compositions. The specific capacity vs. cycle number results are also shown in Table 3.3.3. The higher spinel $\text{LiCo}_{0.5}\text{Mn}_{1.5}\text{O}_4$ content (10mol%) shows the capacity (251mAh/g at 0.1C), cycle performance (90.9% at 50th) and voltage decay (-64mV). By embedding spinel $\text{LiCo}_{0.5}\text{Mn}_{1.5}\text{O}_4$ the cycle performance and voltage decay are improved. The spinel embedded structure improved the structure stability during charge-discharge at small primary particle morphology.

Figure 3.3.10 shows the charge-discharge profiles at the first cycle, i.e. activation at 4.7 V. The cells delivered discharge capacities of 270, 270, 262, and 251 $\text{mAh}\cdot\text{g}^{-1}$ with spinel $\text{LiCo}_{0.5}\text{Mn}_{1.5}\text{O}_4$ 0, 2, 5, and 10 mol% cathode materials, respectively. In spinel $\text{LiCo}_{0.5}\text{Mn}_{1.5}\text{O}_4$ 10mol%, the plateau around 2.7 V during discharging is related to the electrochemical reaction of the spinel phase. This plateau is only visible in spinel $\text{LiCo}_{0.5}\text{Mn}_{1.5}\text{O}_4$ 10mol%.

Full cell cycle performance is evaluated using cylindrical 18650 cell with graphite anode in Figure 3.3.11. Spinel $\text{LiCo}_{0.5}\text{Mn}_{1.5}\text{O}_4$ embedded composite shows better discharge capacity retention and voltage decay. The phase stability using spinel $\text{LiCo}_{0.5}\text{Mn}_{1.5}\text{O}_4$ embedded structure improves the cycling performance.

Table 3.3.1 Electrochemical performance tests of spinel (1) 0, (2) 2, (3) 5, and (4) 10mol% heat-treated at 900degC at different currents (C rates) in the potential range 2.5-4.6/4.7V in coin type cells. Li counter electrodes.

	1st cycle			Discharge Rate @0.5C Cha				Cycle Life (50 th)	
	0.1C Cha mAh/g	0.1C Dis mAh/g	eff. %	0.2C mAh/g	1C Dis mAh/g	2C Dis mAh/g	2C vs. 0.2C	CRR (%)	Voltage Decay (mV)
(1) x=0.00	327	278	85.20	257	231	214	83.40%	95.3	-67
(2) x=0.02	299	259	86.40	241	216	202	83.50%	92.5	-74
(3) x=0.05	293	259	88.40	242	214	198	81.80%	83.4	-94
(4) x=0.10	278	238	85.80	224	196	179	79.80%	78.3	-92

• Based on capacity 230mAh/g, 90:5=(Active Material):DB:PVDF, Charge : 4.70/4.60V, Discharge : 2.5V,

* $(1-x)[0.4\text{Li}_2\text{MnO}_3 \cdot 0.6\text{LiNi}_{0.417}\text{Co}_{0.167}\text{Mn}_{0.417}\text{O}_2] \cdot x\text{LiMn}_2\text{O}_4$

Table 3.3.2 The results of the Rietveld refinement for the materials under study

No.	Composition	Lattice Parameter						Crystal size		
		Li ₂ MnO ₃			Li(Ni _x Co _y Mn _z)O ₂			Li ₂ Mn _{1.5} O ₄	Li ₂ MnO ₃ (nm)	Li(Ni _x Co _y Mn _z)O ₂ (nm)
		a (Å)	b (Å)	c (Å)	beta(deg)	a (Å)	c (Å)			
1	0.4Li ₂ MnO ₃ 0.6LiNi _{0.417} Co _{0.167} Mn _{0.417} O ₂	4.94435	8.58995	5.02724	109.00260	2.85873	14.23635	-	82.5	125.5
2	0.98 0.4Li ₂ MnO ₃ 0.6LiNi _{0.417} Co _{0.167} Mn _{0.417} O ₂] 0.02LiCo _{0.5} Mn _{1.5} O ₄	4.94615	8.58832	5.02816	109.00970	2.85826	14.24412	-	88.2	134.6
3	0.95 0.4Li ₂ MnO ₃ 0.6LiNi _{0.417} Co _{0.167} Mn _{0.417} O ₂] 0.05LiCo _{0.5} Mn _{1.5} O ₄	4.94242	8.57629	5.02722	108.97440	2.85478	14.24464	8.19038	89.1	160.2
4	0.90 0.4Li ₂ MnO ₃ 0.6LiNi _{0.417} Co _{0.167} Mn _{0.417} O ₂] 0.10LiCo _{0.5} Mn _{1.5} O ₄	4.93686	8.56543	5.02352	108.95780	2.85143	14.23277	8.16928	87.2	-
5	0.89 0.4Li ₂ MnO ₃ 0.6LiNi _{0.417} Co _{0.167} Mn _{0.417} O ₂] 0.20LiCo _{0.5} Mn _{1.5} O ₄	4.93888	8.54604	5.03325	109.26210	2.85360	14.22993	8.16902	105.4	-
										69.3

Table 3.3.3 Electrochemical performance tests of spinel (1) 0, (2) 2, (3) 5, and (4) 10mol% heat-treated at 750degC at different currents (C rates) in the potential range 2.5-4.6/4.7V in coin type cells. Li counter electrodes.

	1st cycle			Discharge Rate @0.5C Cha				Cycle Life (50 th)	
	0.1C Cha mAh/g	0.1C Dis mAh/g	eff. %	0.2C mAh/g	1C Dis mAh/g	2C Dis mAh/g	2C vs. 0.2C	CRR (%)	Voltage Decay (mV)
(1) x=0.00	319	270	84.80	252	229	215	85.60%	88.4	-75
(2) x=0.02	300	270	90.10	255	233	219	85.70%	90.7	-70
(3) x=0.05	286	262	91.80	250	225	208	83.30%	90.7	-64
(4) x=0.10	282	251	89.00	235	213	200	85.30%	90.9	-64

• Based on capacity 230mAh/g, 90:5:(Active Material):DB:PVDF, Charge : 4.70/4.60V, Discharge : 2.5V,

* $(1-x)[0.4\text{Li}_2\text{MnO}_3 \cdot 0.6\text{LiNi}_{0.417}\text{Co}_{0.167}\text{Mn}_{0.417}\text{O}_2] \cdot x\text{LiMn}_2\text{O}_4$

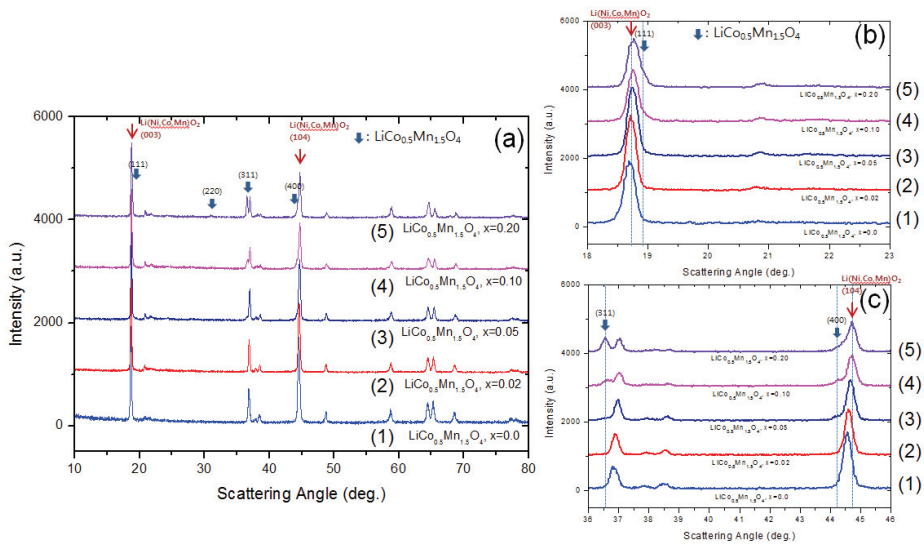


Figure 3.3.1 (a) Panels (1)-(5) are XRD patterns of spinel 0, 2, 5, 10, and 20 mol% respectively, after heat-treatment at 900 °C. Selected angular ranges highlight the (b) layered and (c) spinel peaks.

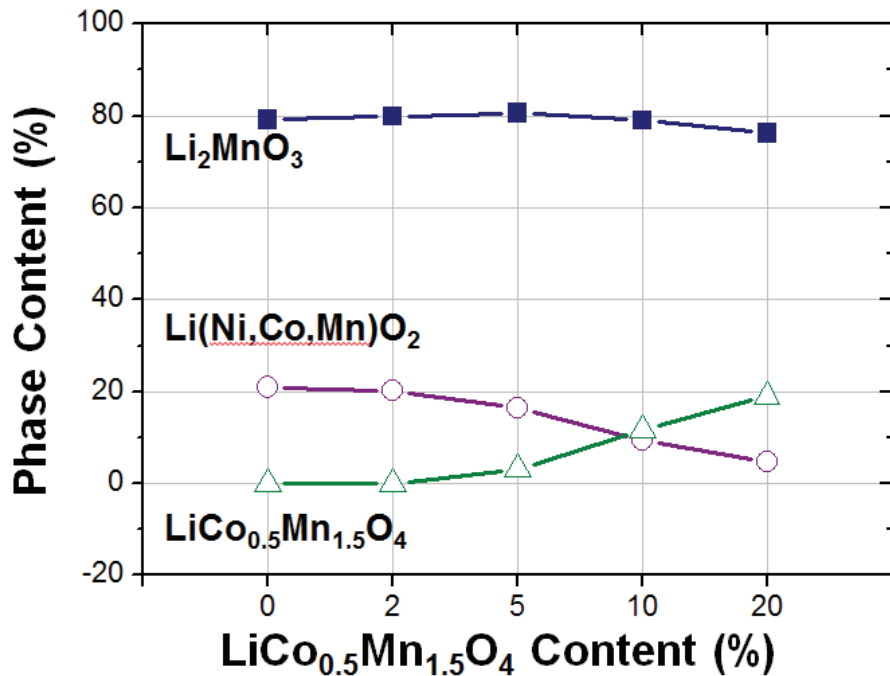


Figure 3.3.2 Rietveld refinement for the phase contents in (1-x)[0.4Li₂MnO₃·0.6Li(Ni,Co,Mn)O₂]·xLiCo_{0.5}Mn_{1.5}O₄ compositions. The fractions are calculated with the composite notation like Li₂MnO₃·Li(Ni,Co,Mn)O₂·LiM_xMn_{2-x}O₄ (M=Ni, Co, Mn).

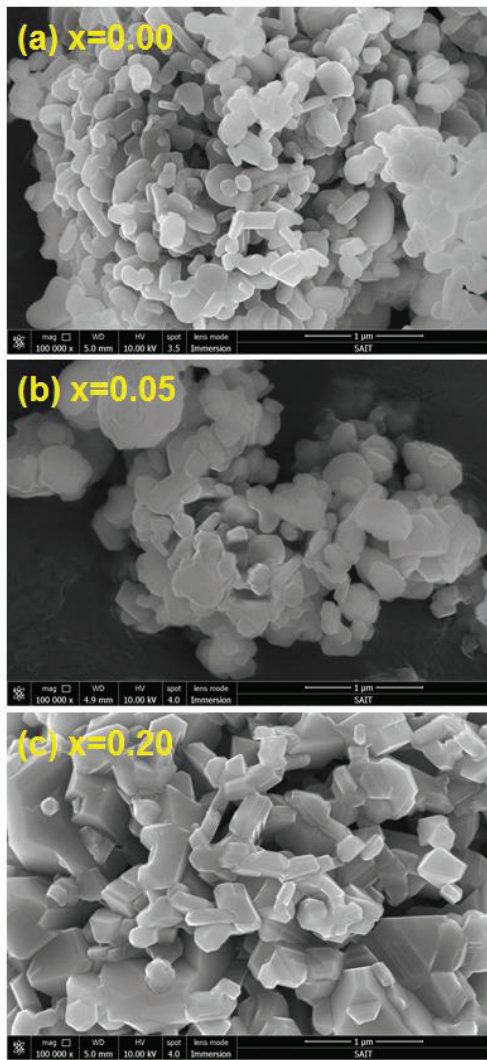


Figure 3.3.3 FESEM images of spinel composites (a) 0, (b) 5, and (c) 20mol% heat-treated at 900 °C.

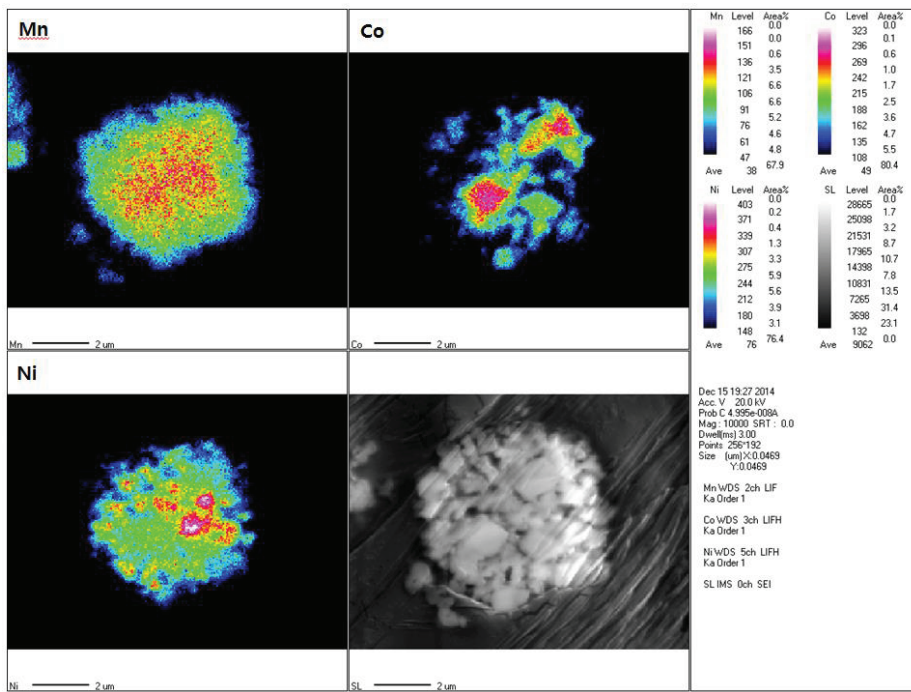


Figure 3.3.4 Cross-sectional EPMA mapping and images of spinel 20mol% composite heat-treated at 900degC. A scale bar is located at the right corner.

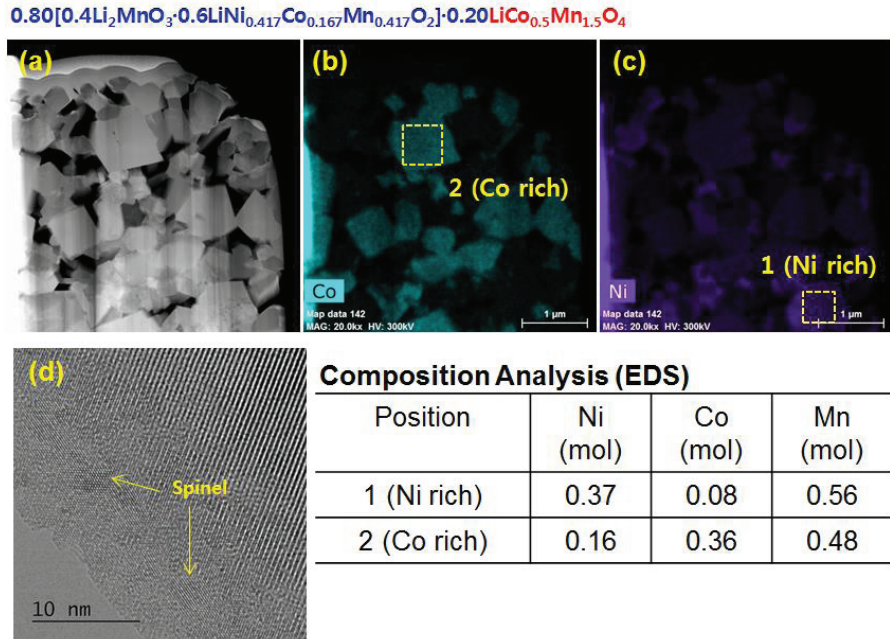
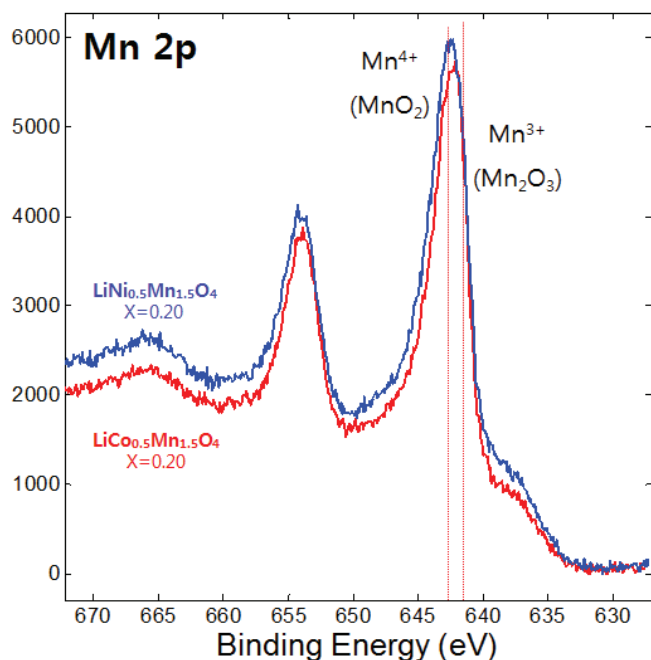


Figure 3.3.5 (a)-(c) HAADF image and EDS mapping taken from spinel 20mol% heat-treated at 900degC. (d) High-resolution TEM image taken from spinel 20mol% heat-treated at 900degC.



Composition Analysis (XPS)

Atomic Concentration Table

Abscissa	Li1s	Mn2p3	Co2p3	Ni2p3
LiCo _{0.5} Mn _{1.5} O ₄ X=0.20	16.65	13.82	1.19	5.15
LiNi _{0.5} Mn _{1.5} O ₄ X=0.20	14.68	12.84	0.56	5.12

Figure 3.3.6 XPS data taken from spinel 20mol% heat-treated at 900degC.

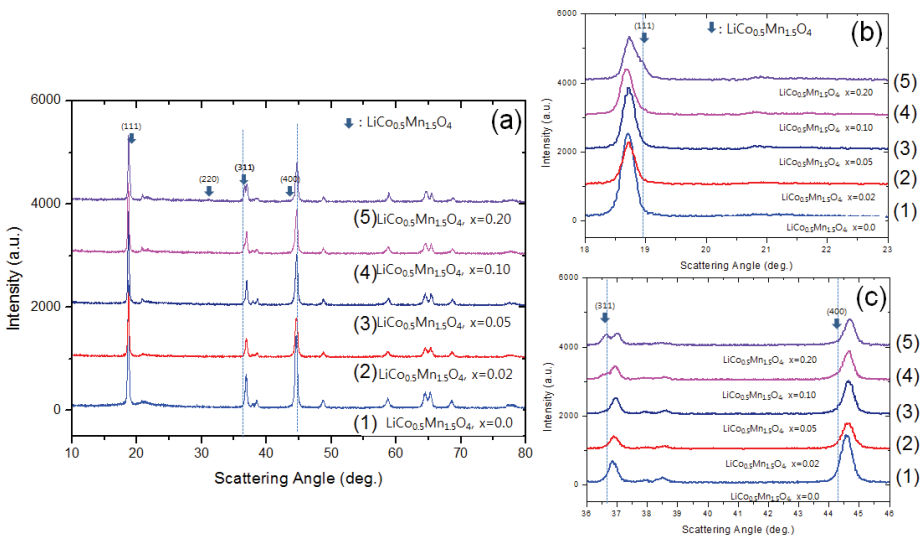


Figure 3.3.7 (a) Panels (1)-(5) are XRD patterns of spinel 0, 2, 5, 10, and 20 mol% respectively, after heat-treatment at 750 °C. Selected angular ranges highlight the (b) layered and (c) spinel peaks.

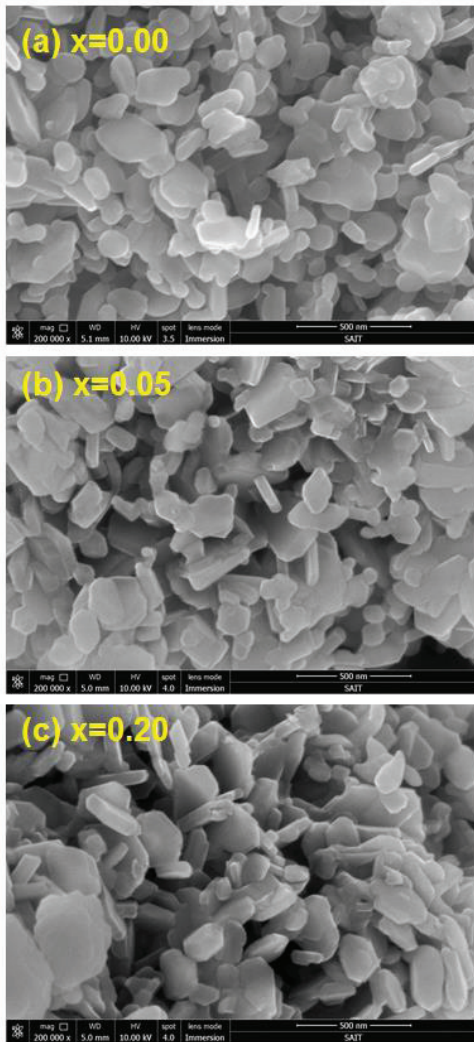


Figure 3.3.8 FESEM images of spinel composites (a) 0, (b) 5, and (c) 20mol% heat-treated at 750 °C.

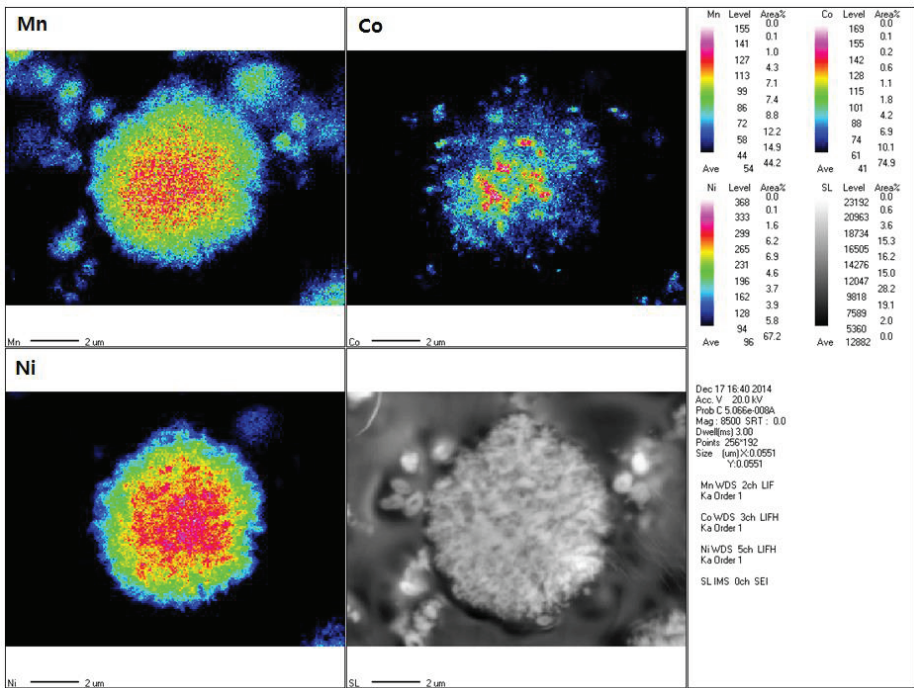


Figure 3.3.9 Cross-sectional EPMA mapping and images of spinel 20mol% composite heat-treated at 750degC. A scale bar is located at the right corner.

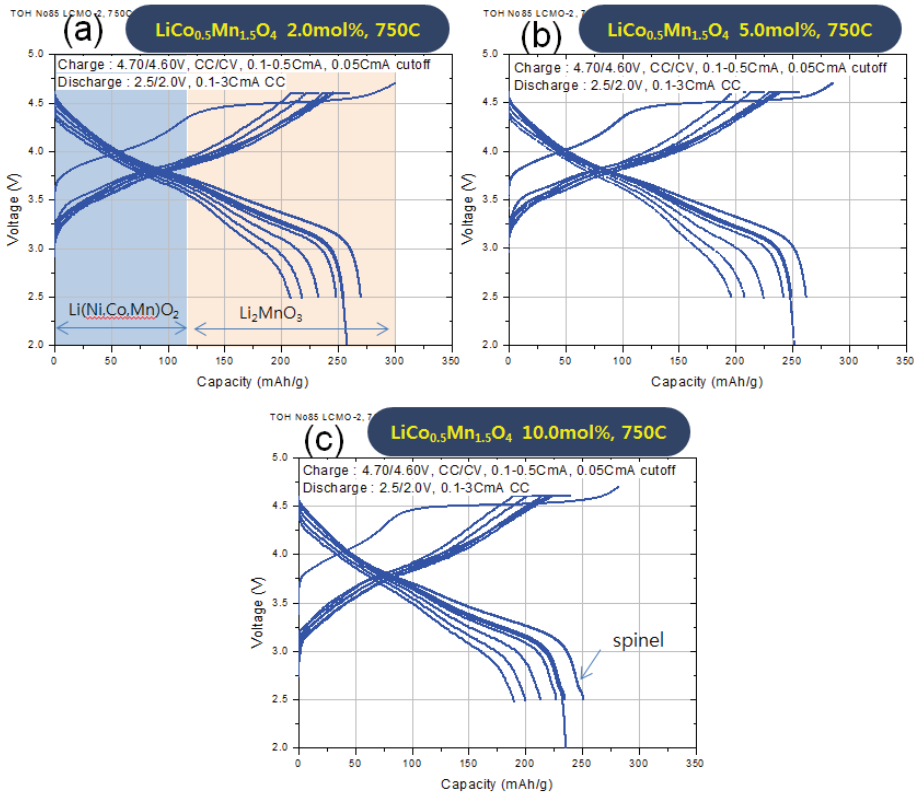


Figure 3.3.10 (a)-(c) Initial charge-discharge profiles measured upon galvanostatic cycle of spinel 0-10mol% compositions heat-treated at 750degC. The data are recorded at 23 mA/g (C/10) rate in the potential range of 2.5-4.7V in coin-type cells with Li counter electrodes.

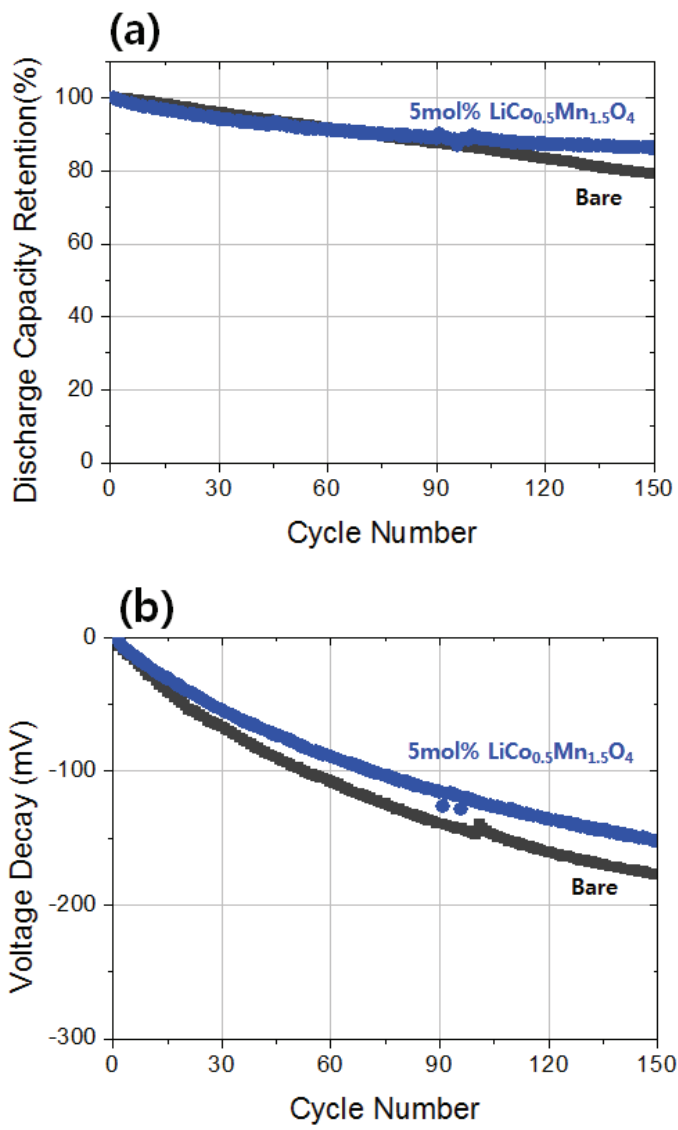


Figure 3.3.11 Full cell cycle life (a) discharge capacity retention (b) voltage decay in 18650-type full cells with graphite anode.

3.4. Conclusions

Spinel embedded lithium rich oxides are synthesized and structural phases are analyzed. By adding Mn, Ni, Co sources in precursor $\text{Ni}_{0.25}\text{Co}_{0.10}\text{Mn}_{0.65}(\text{OH})_2$ the spinel embedded composite oxides are prepared.

In spinel LiMn_2O_4 embedded composition $\text{Li}_2\text{MnO}_3 \cdot \text{Li}(\text{Ni},\text{Co},\text{Mn})\text{O}_2 \cdot \text{LiMn}_2\text{O}_4 \cdot \text{LiNi}_{0.5}\text{Mn}_{1.5}\text{O}_4$ phase is formed. At 750degC heat-treatment spinel LiMn_2O_4 2mol% the capacity retention and voltage decay are improved.

In spinel $\text{LiNi}_{0.5}\text{Mn}_{1.5}\text{O}_4$ embedded composition $\text{Li}_2\text{MnO}_3 \cdot \text{Li}(\text{Ni},\text{Co},\text{Mn})\text{O}_2 \cdot \text{LiNi}_{0.5}\text{Mn}_{1.5}\text{O}_4 \cdot \text{NiO}$ phase is formed. Even using oxygen atmosphere heat-treatment the rocksalt NiO phase is maintained. At 750degC heat-treatment spinel $\text{LiNi}_{0.5}\text{Mn}_{1.5}\text{O}_4$ 2mol% the capacity retention and voltage decay are improved.

In spinel $\text{LiCo}_{0.5}\text{Mn}_{1.5}\text{O}_4$ embedded composition ternary $\text{Li}_2\text{MnO}_3 \cdot \text{Li}(\text{Ni},\text{Co},\text{Mn})\text{O}_2 \cdot \text{LiCo}_{0.5}\text{Mn}_{1.5}\text{O}_4$ phase is formed. Using EPMA Ni and Co segregation is analyzed. At 750degC heat-treatment spinel $\text{LiCo}_{0.5}\text{Mn}_{1.5}\text{O}_4$ 2mol% the capacity retention and voltage decay are improved.

The phase evolutions are summarized in Table 3.4.1. As MnCO_3 is added to evolve LiMn_2O_4 embedded composite $\text{LiNi}_{0.5}\text{Mn}_{1.5}\text{O}_4$ phase is also formed. Some of the added MnCO_3 is consumed to make Li_2MnO_3 and the spinel phase is formed into $\text{LiNi}_{0.5}\text{Mn}_{1.5}\text{O}_4$ in high LiMn_2O_4 embedded composition. As $\text{Ni}(\text{OH})_2$ is used for $\text{LiNi}_{0.5}\text{Mn}_{1.5}\text{O}_4$ embedded composite rocksalt NiO phase is formed. Even in oxygen atmosphere rocksalt NiO phase is inevitable phase. Using $\text{Co}(\text{OH})_2$ precursor the spinel

$\text{LiCo}_{0.5}\text{Mn}_{1.5}\text{O}_4$ embedded composite is homogeneously formed.

The phases which are evolved in different spinel composition design are compared in XRD data in Figure 3.4.1. Each spinel phase can be distinguished in spinel peak position spinel (311) and spine (400) peaks.

The formation energies of spinel embedded composite are calculated using ab initio method in Figure 3.4.2. In the baseline $\text{Li}_2\text{MnO}_3 \cdot \text{Li}(\text{Ni},\text{Co},\text{Mn})\text{O}_2$ composite the spinel $\text{LiCo}_{0.5}\text{Mn}_{1.5}\text{O}_4$ embedding decreases formation energy in (1)

$0.8[0.4\text{Li}_2\text{MnO}_3 \cdot 0.6\text{LiNi}_{0.417}\text{Co}_{0.167}\text{Mn}_{0.417}\text{O}_2] \cdot 0.2\text{LiCo}_{0.5}\text{Mn}_{1.5}\text{O}_4$. The phase stability of spinel $\text{LiCo}_{0.5}\text{Mn}_{1.5}\text{O}_4$ lowers the formation energy. Mixed spinel $\text{LiCo}_{0.25}\text{Ni}_{0.25}\text{Mn}_{1.5}\text{O}_4$ phase shows similar formation energy as $\text{LiCo}_{0.5}\text{Mn}_{1.5}\text{O}_4$. As Li_2MnO_3 is increased from 40% to 45%, the formation energy decreases to -32.516eV/f.u.. Li_2MnO_3 and mixed spinel $\text{LiCo}_{0.25}\text{Ni}_{0.25}\text{Mn}_{1.5}\text{O}_4$ embedding decreases the formation energy more.

The phase evolution is analyzed using high temperature XRD in the spinel $\text{LiCo}_{0.5}\text{Mn}_{1.5}\text{O}_4$ embedding in in Figure 3.4.3. Layered $\text{Li}(\text{Ni},\text{Co},\text{Mn})\text{O}_2$ phase is emerged at 400degC. Layered Li_2MnO_3 -like superlattice peak is detected at 550degC. Spinel $\text{LiCo}_{0.5}\text{Mn}_{1.5}\text{O}_4$ peak is emerged at 650degC. The spinel $\text{LiCo}_{0.5}\text{Mn}_{1.5}\text{O}_4$ is stabilized after layered $\text{Li}(\text{Ni},\text{Co},\text{Mn})\text{O}_2$ and Li_2MnO_3 are formed. Lithium is going to be accommodated by the formation of Li_2MnO_3 -like domains, and then layered $\text{Li}(\text{Ni},\text{Co},\text{Mn})\text{O}_2$ and spinel $\text{LiCo}_{0.5}\text{Mn}_{1.5}\text{O}_4$ domains.[46]

Figure 3.4.4 schematically sketches the phase evolution during heat-treatment of spinel embedded composite. When the raw materials for spinel phase (MnCO_3 , Ni(OH)_2 , and Co(OH)_2) are added, cobalt and nickel

become segregated. In the segregated region the ternary $\text{Li}_2\text{MnO}_3 \cdot \text{Li}(\text{Ni},\text{Co},\text{Mn})\text{O}_2 \cdot \text{LiM}_{0.5}\text{Mn}_{1.5}\text{O}_4$ ($\text{M}=\text{Ni, Co, Mn}$) phase is formed.

In lithium-rich composite oxide by adding spinel forming sources the different types of spinel phase embedded composites are synthesized. Controlling the spinel composition and content the electrochemical performance is improved.

Table 3.4.1 Summary of spinel composites.

Composite	$\text{Li}_2\text{MnO}_3 \cdot \text{Li}(\text{Ni},\text{Co},\text{Mn})\text{O}_2$	+ Li-M-O	Phases
I. $\text{Li}_2\text{MnO}_3 \cdot \text{Li}(\text{Ni},\text{Co},\text{Mn})\text{O}_2 \cdot \text{LiMn}_2\text{O}_4$	$(\text{Ni},\text{Co},\text{Mn})(\text{OH})_2 + \text{Li}_2\text{CO}_3$	+ MnCO_3	$\text{Li}_2\text{MnO}_3 \cdot \text{Li}(\text{Ni},\text{Co},\text{Mn})\text{O}_2 \cdot \text{LiMn}_2\text{O}_4 \cdot \text{LiNi}_{0.5}\text{Mn}_{1.5}\text{O}_4$
II. $\text{Li}_2\text{MnO}_3 \cdot \text{Li}(\text{Ni},\text{Co},\text{Mn})\text{O}_2 \cdot \text{LiNi}_{0.5}\text{Mn}_{1.5}\text{O}_4$	$(\text{Ni},\text{Co},\text{Mn})(\text{OH})_2 + \text{Li}_2\text{CO}_3$	+ $\text{MnCO}_3 + \text{Ni}(\text{OH})_2$	$\text{Li}_2\text{MnO}_3 \cdot \text{Li}(\text{Ni},\text{Co},\text{Mn})\text{O}_2 \cdot \text{LiNi}_{0.5}\text{Mn}_{1.5}\text{O}_4 \cdot \text{NiO}$
III. $\text{Li}_2\text{MnO}_3 \cdot \text{Li}(\text{Ni},\text{Co},\text{Mn})\text{O}_2 \cdot \text{LiCo}_{0.5}\text{Mn}_{1.5}\text{O}_4$	$(\text{Ni},\text{Co},\text{Mn})(\text{OH})_2 + \text{Li}_2\text{CO}_3$	+ $\text{MnCO}_3 + \text{Co}(\text{OH})_2$	$\text{Li}_2\text{MnO}_3 \cdot \text{Li}(\text{Ni},\text{Co},\text{Mn})\text{O}_2 \cdot \text{LiCo}_{0.5}\text{Mn}_{1.5}\text{O}_4$

* Base composition : $\text{Li}_{1.40}\text{Ni}_{0.25}\text{Co}_{0.10}\text{Mn}_{0.65}\text{O}_{2.40} - 0.4\text{Li}_2\text{MnO}_3 \cdot 0.6\text{LiNi}_{0.417}\text{Co}_{0.167}\text{Mn}_{0.417}\text{O}_2$

** $(1-x)[0.4\text{Li}_2\text{MnO}_3 \cdot 0.6\text{LiNi}_{0.417}\text{Co}_{0.167}\text{Mn}_{0.417}\text{O}_2]x\text{LiMn}_{0.5}\text{Mn}_{1.5}\text{O}_4$ (M=Mn, Ni, Co)

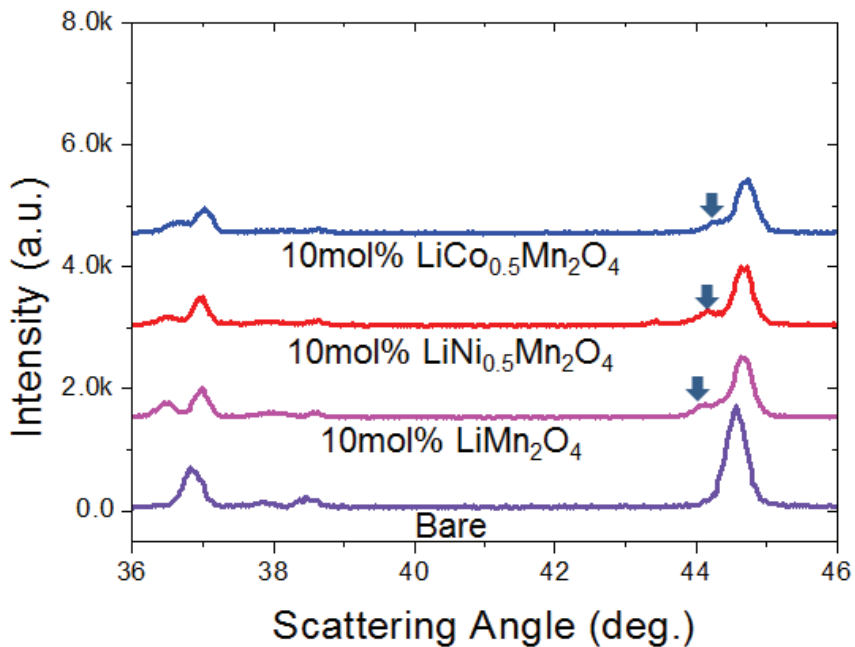
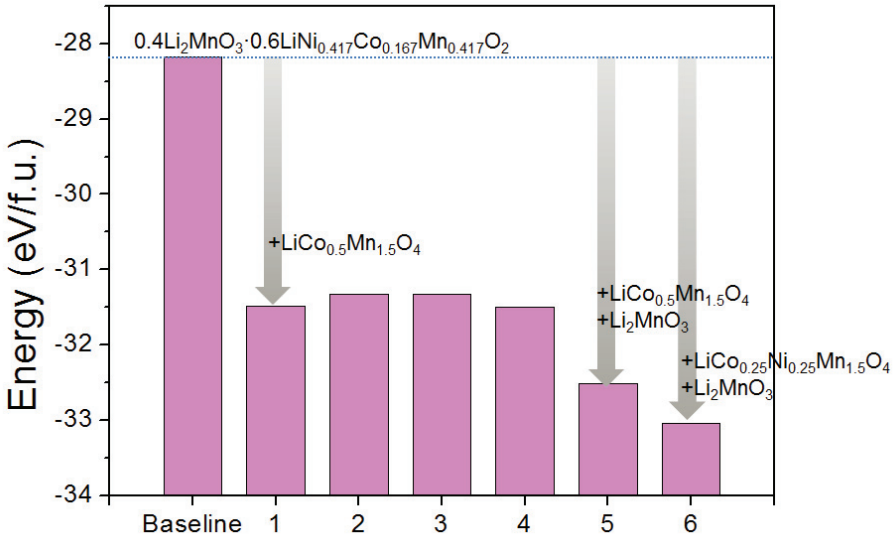


Figure 3.4.1 (a) Panels (1)-(4) are XRD patterns of spinel 0mol%, 20mol% LiMn₂O₄, 20mol% LiNi_{0.5}Mn_{1.5}O₄ and 20mol% LiCo_{0.5}Mn_{1.5}O₄ respectively, after heat-treatment at 900 °C. Selected angular ranges highlight the (b) layered and (c) spinel peaks.



Composition : Synthesis-Design *	Composition : Composite structure (Probable)	Formation Energy ** (eV/f.u.)
$\text{Li}_{1.40}\text{-Ni}_{0.25}\text{Co}_{0.10}\text{Mn}_{0.65}\text{-O}$	Baseline) $0.4\text{Li}_2\text{MnO}_3 \cdot 0.6\text{LiNi}_{0.417}\text{Co}_{0.167}\text{Mn}_{0.417}\text{O}_2$	-28.173
	(1) $0.8[0.4\text{Li}_2\text{MnO}_3 \cdot 0.6\text{LiNi}_{0.417}\text{Co}_{0.167}\text{Mn}_{0.417}\text{O}_2] \cdot 0.2\text{LiCo}_{0.5}\text{Mn}_{1.5}\text{O}_4$	-31.483
	(2) $0.8[0.4\text{Li}_2\text{MnO}_3 \cdot 0.6\text{LiNi}_{0.209}\text{Co}_{0.375}\text{Mn}_{0.416}\text{O}_2] \cdot 0.2\text{LiNi}_{0.5}\text{Mn}_{1.5}\text{O}_4$	-31.329
$\text{Li}_{1.10}\text{-Ni}_{0.167}\text{Co}_{0.150}\text{Mn}_{0.683}\text{-O}$	(3) $0.8[0.4\text{Li}_2\text{MnO}_3 \cdot 0.6\text{LiNi}_{0.418}\text{Co}_{0.375}\text{Mn}_{0.206}\text{O}_2] \cdot 0.2\text{LiMn}_2\text{O}_4$	-31.324
	(4) $0.8[0.4\text{Li}_2\text{MnO}_3 \cdot 0.6\text{LiNi}_{0.313}\text{Co}_{0.271}\text{Mn}_{0.416}\text{O}_2] \cdot 0.2\text{LiCo}_{0.25}\text{Ni}_{0.25}\text{Mn}_{1.5}\text{O}_4$	-31.492
	(5) $0.8[0.45\text{Li}_2\text{MnO}_3 \cdot 0.55\text{LiNi}_{0.481}\text{Co}_{0.167}\text{Mn}_{0.359}\text{O}_2] \cdot 0.226\text{LiCo}_{0.5}\text{Mn}_{1.5}\text{O}_4$	-32.516
	(6) $0.8[0.45\text{Li}_2\text{MnO}_3 \cdot 0.55\text{LiNi}_{0.348}\text{Co}_{0.299}\text{Mn}_{0.359}\text{O}_2] \cdot 0.226\text{LiCo}_{0.25}\text{Ni}_{0.25}\text{Mn}_{1.5}\text{O}_4$	-33.036

Figure 3.4.2 Formation energy of spinel embedded composite.

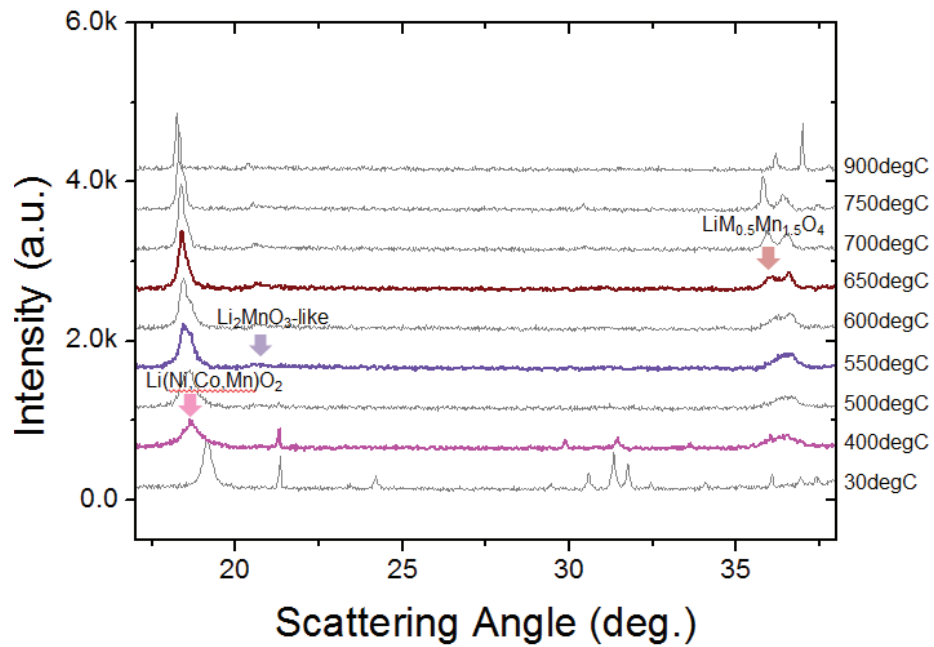


Figure 3.4.3 High temperature XRD of spinel embedded composite.

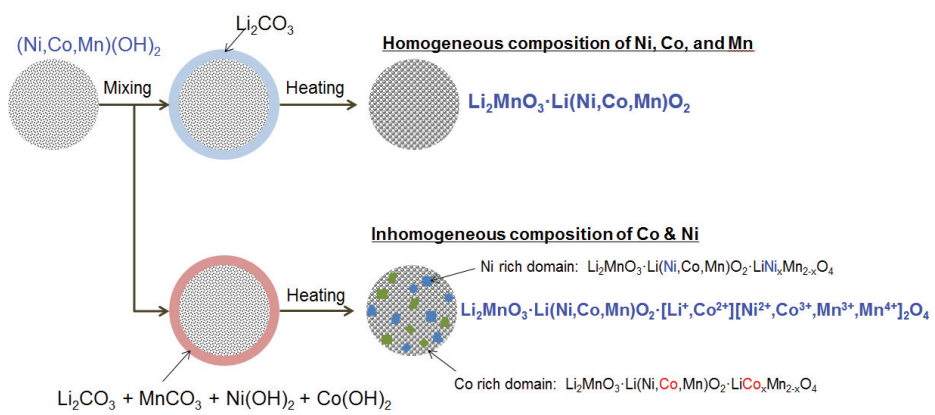


Figure 3.4.4 Schematic drawing showing the proposed phase evolution process for spinel embedded composite.

Chapter 4.

Conclusion

Lithium-rich oxides $\text{Li}_x\text{Ni}_{0.25}\text{Co}_{0.10}\text{Mn}_{0.65}\text{O}_{(3.4+x)/2}$ ($x = 1.6, 1.4, 1.2, 1.0, 0.8$) were synthesized by hydroxide co-precipitation method. The baseline $x=1.4$ composition showed the best electrochemical performance due to its small primary particle size and homogeneous distribution of nano-sized phase domains. XRD, XANES and EXAFS studies indicate that the high-lithium compositions Li1.60 and Li1.40 consisted of two phases ($\text{C}2/\text{m}$) and ($\text{R}3^-\text{m}$) phase which contains Ni^{2+} and Ni^{3+} . At lower lithium levels ($x < 1.4$) the composition contains three different phases: ($\text{C}2/\text{m}$), ($\text{R}3^-\text{m}$) and the spinel phase $\text{LiM}_x\text{Mn}_{2-x}\text{O}_4$ ($\text{Fd}3^-\text{m}$). EXAFS analysis shows that low lithium content forces Co to move from octahedral site to tetrahedral site, suggesting that the spinel phase might be composed of mixed transition metals as $[\text{Li}^+, \text{Co}^{2+}][\text{Ni}^{2+}, \text{Co}^{3+}, \text{Mn}^{4+}]_2\text{O}_4$. Low lithium condition is also shown to induce Co, Ni segregation and primary particle growth. As the spinel phase is known to affect the electrochemical performance of the composite, results presented here will help formulating the composition and synthesis protocol of cobalt-containing, lithium-rich oxides for optimal Li-ion batteries performance.

Spinel embedded lithium rich oxides are synthesized and structural phases are analyzed. By adding Mn, Ni, Co sources in precursor NiCoMn(OH)_2 the spinel embedded composite oxides are prepared.

In spinel LiMn_2O_4 embedded composition $\text{Li}_2\text{MnO}_3 \cdot \text{Li}(\text{Ni}, \text{Co}, \text{Mn})\text{O}_2 \cdot \text{LiMn}_2\text{O}_4 \cdot \text{LiNi}_{0.5}\text{Mn}_{1.5}\text{O}_4$ phase is formed. At 750degC heat-treatment spinel LiMn_2O_4 2mol% the capacity retention and voltage decay are improved.

In spinel $\text{LiNi}_{0.5}\text{Mn}_{1.5}\text{O}_4$ embedded composition $\text{Li}_2\text{MnO}_3 \cdot \text{Li}(\text{Ni},\text{Co},\text{Mn})\text{O}_2 \cdot \text{LiNi}_{0.5}\text{Mn}_{1.5}\text{O}_4 \cdot \text{NiO}$ phase is formed. Using oxygen atmosphere heat-treatment the rocksalt NiO phase is maintained. At 750degC heat-treatment spinel $\text{LiNi}_{0.5}\text{Mn}_{1.5}\text{O}_4$ 2mol% the capacity retention and voltage decay are improved.

In spinel $\text{LiCo}_{0.5}\text{Mn}_{1.5}\text{O}_4$ embedded composition ternary $\text{Li}_2\text{MnO}_3 \cdot \text{Li}(\text{Ni},\text{Co},\text{Mn})\text{O}_2 \cdot \text{LiCo}_{0.5}\text{Mn}_{1.5}\text{O}_4$ phase is formed. Using EPMA Ni and Co segregation is analyzed. At 750degC heat-treatment spinel LiMn_2O_4 2mol% the capacity retention and voltage decay are improved.

The formation energy calculation using ab initio method shows that spinel embedding can decrease the formation energy in the ternary $\text{Li}_2\text{MnO}_3 \cdot \text{Li}(\text{Ni},\text{Co},\text{Mn})\text{O}_2 \cdot \text{LiM}_{0.5}\text{Mn}_{1.5}\text{O}_4$ ($\text{M}=\text{Ni, Co, Mn}$) phase. More Li_2MnO_3 can decrease the formation energy.

High temperature XRD analysis shows that layered $\text{Li}(\text{Ni},\text{Co},\text{Mn})\text{O}_2$ is emerged first, layered Li_2MnO_3 , and then spinel $\text{LiCo}_{0.5}\text{Mn}_{1.5}\text{O}_4$. Low lithium concentration region can facilitate the formation of spine phase.[73, 74]

References

- [1] M.S. Whittingham, *Chemical reviews* **104** (2004) (10) 4271.
- [2] K. Ozawa, *Solid State Ionics* **69** (1994) (3) 212.
- [3] N. Yabuuchi, K. Yoshii, S.-T. Myung, I. Nakai, S. Komaba, *Journal of the American Chemical Society* **133** (2011) (12) 4404.
- [4] S. Hy, H. Liu, M. Zhang, D. Qian, B.-J. Hwang, Y.S. Meng, *Energy & Environmental Science* **9** (2016) (6) 1931.
- [5] D. Andre, S.-J. Kim, P. Lamp, S.F. Lux, F. Maglia, O. Paschos, B. Stiaszny, *Journal of Materials Chemistry A* **3** (2015) (13) 6709.
- [6] M.S. Whittingham, *Chemical Reviews* **114** (2014) (23) 11414.
- [7] B. Dunn, H. Kamath, J.-M. Tarascon, *Science* **334** (2011) (6058) 928.
- [8] M.M. Thackeray, S.-H. Kang, C.S. Johnson, J.T. Vaughey, R. Benedek, S. Hackney, *Journal of Materials Chemistry* **17** (2007) (30) 3112.
- [9] B.R. Long, J.R. Croy, J.S. Park, J. Wen, D.J. Miller, M.M. Thackeray, *Journal of The Electrochemical Society* **161** (2014) (14) A2160.
- [10] J.-M. Kim, N. Kumagai, Y. Kadoma, H. Yashiro, *J. Power Sources* **174** (2007) (2) 473.
- [11] J.-H. Park, J. Lim, J. Yoon, K.-S. Park, J. Gim, J. Song, H. Park, D. Im, M. Park, D. Ahn, *Dalton Transactions* **41** (2012) (10) 3053.
- [12] T. Zhao, L. Li, R. Chen, H. Wu, X. Zhang, S. Chen, M. Xie, F. Wu,

- J. Lu, K. Amine, *Nano Energy* **15** (2015) 164.
- [13] J. Li, J. Camardese, R. Shunmugasundaram, S. Glazier, Z. Lu, J.R. Dahn, *Chemistry of Materials* **27** (2015) (9) 3366.
- [14] W. Choi, A. Benayad, J.-H. Park, J. Park, S.-G. Doo, J. Mun, *Electrochimica Acta* **117** (2014) 492.
- [15] J. Zheng, M. Gu, J. Xiao, B.J. Polzin, P. Yan, X. Chen, C. Wang, J.-G. Zhang, *Chemistry of Materials* **26** (2014) (22) 6320.
- [16] P.K. Nayak, J. Grinblat, M. Levi, B. Markovsky, D. Aurbach, *Journal of The Electrochemical Society* **161** (2014) (10) A1534.
- [17] Y. Wang, N. Sharma, D. Su, D. Bishop, H. Ahn, G. Wang, *Solid State Ionics* **233** (2013) 12.
- [18] H. Koga, L. Croguennec, M. Ménétrier, K. Douhil, S. Belin, L. Bourgeois, E. Suard, F. Weill, C. Delmas, *Journal of The Electrochemical Society* **160** (2013) (6) A786.
- [19] J.R. Croy, D. Kim, M. Balasubramanian, K. Gallagher, S.-H. Kang, M.M. Thackeray, *Journal of The Electrochemical Society* **159** (2012) (6) A781.
- [20] B. Choi, J.Y. Yoon, J.-H. Park, M. Kim, Y.-s. Kang, S.-J. Ahn, S.-G. Doo, Voltage Decay Performance at High Voltage Cycling in Cobalt Content Controlled Lithium and Manganese Rich Oxide, *64th Annual Meeting of the International Society of Electrochemistry*, The International Society of Electrochemistry, Santiago de Queretaro, Mexico (2013).
- [21] H. Deng, I. Belharouak, H. Wu, D. Dambourret, K. Amine, *Journal of The Electrochemical Society* **157** (2010) (7) A776.

- [22] C.S. Johnson, N. Li, C. Lefief, J.T. Vaughey, M.M. Thackeray, *Chemistry of Materials* **20** (2008) (19) 6095.
- [23] S.-H. Kang, P. Kempgens, S. Greenbaum, A. Kropf, K. Amine, M. Thackeray, *Journal of Materials Chemistry* **17** (2007) (20) 2069.
- [24] C.S. Johnson, N. Li, C. Lefief, M.M. Thackeray, *Electrochemistry Communications* **9** (2007) (4) 787.
- [25] M.M. Thackeray, S.H. Kang, C.S. Johnson, J.T. Vaughey, S.A. Hackney, *Electrochemistry Communications* **8** (2006) (9) 1531.
- [26] P.K. Nayak, J. Grinblat, M. Levi, O. Haik, E. Levi, Y.-K. Sun, N. Munichandraiah, D. Aurbach, *Journal of Materials Chemistry A* (2015).
- [27] J. Yang, F. Cheng, X. Zhang, H. Gao, Z. Tao, J. Chen, *J. Mater. Chem. A* **2** (2014) (6) 1636.
- [28] B.R. Long, J.R. Croy, F. Dogan, M.R. Suchomel, B. Key, J. Wen, D.J. Miller, M.M. Thackeray, M. Balasubramanian, *Chemistry of Materials* (2014).
- [29] H. Deng, I. Belharouak, Y.-K. Sun, K. Amine, *Journal of Materials Chemistry* **19** (2009) (26) 4510.
- [30] Z. Lu, J.R. Dahn, *Journal of The Electrochemical Society* **149** (2002) (7) A815.
- [31] C. Liu, Z. Wang, C. Shi, E. Liu, C. He, N. Zhao, *ACS applied materials & interfaces* **6** (2014) (11) 8363.
- [32] D. Kim, G. Sandi, J.R. Croy, K.G. Gallagher, S.-H. Kang, E. Lee, M.D. Slater, C.S. Johnson, M.M. Thackeray, *Journal of The Electrochemical*

Society **160** (2013) (1) A31.

- [33] M. Gu, I. Belharouak, J. Zheng, H. Wu, J. Xiao, A. Genc, K. Amine, S. Thevuthasan, D.R. Baer, J.-G. Zhang, N.D. Browning, J. Liu, C. Wang, *ACS Nano* **7** (2013) (1) 760.
- [34] P. Lu, P. Yan, E. Romero, E.D. Spoerke, J.-G. Zhang, C.-M. Wang, *Chemistry of Materials* **27** (2015) (4) 1375.
- [35] H. Kawai, M. Nagata, H. Tukamoto, A.R. West, *J. Power Sources* **81** (1999) 67.
- [36] A. Bhaskar, N.N. Bramnik, A. Senyshyn, H. Fuess, H. Ehrenberg, *J. Electrochem. Soc.* **157** (2010) (6) A689.
- [37] H. Deng, I. Belharouak, R.E. Cook, H. Wu, Y.-K. Sun, K. Amine, *Journal of The Electrochemical Society* **157** (2010) (4) A447.
- [38] á. Ravel, M. Newville, *Journal of synchrotron radiation* **12** (2005) (4) 537.
- [39] G. Kresse, J. Hafner, *Physical Review B* **47** (1993) (1) 558.
- [40] G. Kresse, J. Furthmüller, *Computational Materials Science* **6** (1996) (1) 15.
- [41] G. Kresse, D. Joubert, *Physical Review B* **59** (1999) (3) 1758.
- [42] J.P. Perdew, K. Burke, M. Ernzerhof, *Physical review letters* **77** (1996) (18) 3865.
- [43] L. Wang, T. Maxisch, G. Ceder, *Physical Review B* **73** (2006) (19) 195107.

- [44] X. Yu, Y. Lyu, L. Gu, H. Wu, S.M. Bak, Y. Zhou, K. Amine, S.N. Ehrlich, H. Li, K.W. Nam, *Advanced Energy Materials* **4** (2014) (5).
- [45] W.-S. Yoon, M. Balasubramanian, K.Y. Chung, X.-Q. Yang, J. McBreen, C.P. Grey, D.A. Fischer, *J. Am. Chem. Soc.* **127** (2005) (49) 17479.
- [46] J. Barenco, M. Balasubramanian, S. Kang, J. Wen, C. Lei, S. Pol, I. Petrov, D. Abraham, *Chem. Mater.* **23** (2011) (8) 2039.
- [47] E. McCalla, C. Lowartz, C. Brown, J. Dahn, *Chemistry of Materials* **25** (2013) (6) 912.
- [48] E. McCalla, A. Rowe, R. Shunmugasundaram, J. Dahn, *Chemistry of Materials* **25** (2013) (6) 989.
- [49] E.-S. Lee, A. Huq, H.-Y. Chang, A. Manthiram, *Chemistry of Materials* **24** (2012) (3) 600.
- [50] Y. Ein-Eli, W. Howard, S.H. Lu, S. Mukerjee, J. McBreen, J.T. Vaughey, M.M. Thackeray, *J. Electrochem. Soc.* **145** (1998) (4) 1238.
- [51] J. Li, L. Wang, Q. Zhang, X. He, *Journal of Power Sources* **189** (2009) (1) 28.
- [52] J. Lee, A. Urban, X. Li, D. Su, G. Hautier, G. Ceder, *Science* **343** (2014) (6170) 519.
- [53] J.R. Croy, H. Iddir, K. Gallagher, C.S. Johnson, R. Benedek, M. Balasubramanian, *Physical Chemistry Chemical Physics* (2015).
- [54] J.R. Croy, M. Balasubramanian, K.G. Gallagher, A.K. Burrell, *Accounts of Chemical Research* **48** (2015) (11) 2813.
- [55] Y.K. Sun, M.J. Lee, C.S. Yoon, J. Hassoun, K. Amine, B. Scrosati,

Advanced Materials **24** (2012) (9) 1192.

- [56] M.N. Ates, Q. Jia, A. Shah, A. Busnaina, S. Mukerjee, K. Abraham, *Journal of The Electrochemical Society* **161** (2014) (3) A290.
- [57] J.R. Croy, J.S. Park, Y. Shin, B.T. Yonemoto, M. Balasubramanian, B.R. Long, Y. Ren, M.M. Thackeray, *Journal of Power Sources* **334** (2016) 213.
- [58] S. Kim, J.-K. Noh, M. Aykol, Z. Lu, H. Kim, W. Choi, C. Kim, K.Y. Chung, C. Wolverton, B.-W. Cho, *ACS applied materials & interfaces* **8** (2015) (1) 363.
- [59] K.M. Shaju, P.G. Bruce, *Chemistry of Materials* **20** (2008) (17) 5557.
- [60] J. Cabana, M. Casas-Cabanas, F.O. Omenya, N.A. Chernova, D. Zeng, M.S. Whittingham, C.P. Grey, *Chemistry of Materials* **24** (2012) (15) 2952.
- [61] A. Manthiram, K. Chemelewski, E.-S. Lee, *Energy & Environmental Science* **7** (2014) (4) 1339.
- [62] K.R. Chemelewski, E.-S. Lee, W. Li, A. Manthiram, *Chemistry of Materials* **25** (2013) (14) 2890.
- [63] T.-F. Yi, Y. Xie, M.-F. Ye, L.-J. Jiang, R.-S. Zhu, Y.-R. Zhu, *Ionics* **17** (2011) (5) 383.
- [64] A. West, *Journal of Materials Chemistry* **8** (1998) (4) 837.
- [65] M. Hu, Y. Tian, J. Wei, D. Wang, Z. Zhou, *Journal of Power Sources* **247** (2014) 794.

- [66] A. Bhaskar, N.N. Bramnik, A. Senyshyn, H. Fuess, H. Ehrenberg, *Journal of The Electrochemical Society* **157** (2010) (6) A689.
- [67] R.I. Eglitis, *Physica Scripta* **90** (2015) (9) 094012.
- [68] D. Wang, I. Belharouak, L.H. Ortega, X. Zhang, R. Xu, D. Zhou, G. Zhou, K. Amine, *Journal of Power Sources* **274** (2015) 451.
- [69] P.K. Nayak, J. Grinblat, M. Levi, O. Haik, E. Levi, Y.-K. Sun, N. Munichandraiah, D. Aurbach, *Journal of Materials Chemistry A* **3** (2015) (28) 14598.
- [70] J. Li, J. Camardese, R. Shunmugasundaram, S. Glazier, Z. Lu, J. Dahn, *Chemistry of Materials* **27** (2015) (9) 3366.
- [71] M. Gu, A. Genc, I. Belharouak, D. Wang, K. Amine, S. Thevuthasan, D.R. Baer, J.-G. Zhang, N.D. Browning, J. Liu, *Chemistry of Materials* **25** (2013) (11) 2319.
- [72] G.-L. Xu, Y. Qin, Y. Ren, L. Cai, K. An, K. Amine, Z. Chen, *Journal of Materials Chemistry A* **3** (2015) (24) 13031.
- [73] B. Xu, C.R. Fell, M. Chi, Y.S. Meng, *Energy & Environmental Science* **4** (2011) (6) 2223.
- [74] S. Komaba, L. Croguennec, F. Tournadre, P. Willmann, C. Delmas, *The Journal of Physical Chemistry C* **117** (2013) (7) 3264.

초 록

리튬 과잉 복합 양극소재 $\text{Li}_x\text{Ni}_{0.25}\text{Co}_{0.10}\text{Mn}_{0.65}\text{O}_{(3.4+x)/2}$ ($x=1.6, 1.4, 1.2, 1.0, 0.8$)를 전구체 및 고상합성으로 제조하여 구조, 형상 및 전기화학 특성 분석을 진행하였다. 리튬 함량에 따른 XRD구조 분석으로 리튬 함량이 높은 경우($x=1.6$ 과 1.4) 2상 복합구조인 Li_2MnO_3 ($\text{C}2/\text{m}$)와 LiMO_2 ($\text{M} = \text{Ni}, \text{Co}, \text{Mn}$) ($\text{R}3^-\text{m}$)를 가지고, 리튬 함량이 작은 경우($x=1.2, 1.0$, 및 0.8) 추가적으로 스피넬 LiM_2O_4 ($\text{Fd}3^-\text{m}$) 가지는 3상 복합 구조를 가지는 점을 밝혀냈다. 3상 복합에 추가된 스피넬 구조는 전기화학 특성에 큰 영향을 미친다. 구조 분석 결과 생성된 스피넬 구조는 코발트가 리튬층과 전이금속층에 코발트 산화수 2가와 산화수 3가가 각각 들어간 $[\text{Li}^+, \text{Co}^{2+}][\text{Ni}^{2+}, \text{Co}^{3+}, \text{Mn}^{4+}]_2\text{O}_4$ 구조이다. 리튬 함량이 작은 경우 1차입자의 성장도 커짐과 코발트 와 니켈이 조성 분리 되어 2차입자내 분포함을 알 수 있었다.

리튬 과잉 전구체에 스피넬 복합 구조를 도입하기 위해 망간, 니켈 및 코발트를 혼합하여 스피넬 복합 리튬 과잉 복합 양극재 $\text{Li}_2\text{MnO}_3 \cdot \text{Li}(\text{Ni}, \text{Co}, \text{Mn})\text{O}_2 \cdot \text{LiM}_{0.5}\text{Mn}_{1.5}\text{O}_4$ ($\text{M} = \text{Mn}, \text{Ni}, \text{Co}$)를 합성하였다. XRD구조 분석으로 Li_2MnO_3 ($\text{C}2/\text{m}$), $\text{Li}(\text{Ni}, \text{Co}, \text{Mn})\text{O}_2$ ($\text{R}3^-\text{m}$), 및 스피넬 $\text{LiM}_{0.5}\text{Mn}_{1.5}\text{O}_4$ ($\text{M} = \text{Mn}, \text{Ni}, \text{Co}$) ($\text{Fd}3^-\text{m}$)이 형성됨을 확인하였다. $\text{LiM}_{0.5}\text{Mn}_{1.5}\text{O}_4$ ($\text{M} = \text{Mn}$) 복합 조성으로 LiMn_2O_4 상 복합화 확인 되었으며 20mol%이상에서 추가적으로 $\text{LiNi}_{0.5}\text{Mn}_{1.5}\text{O}_4$ 상이 검출되었다. $\text{LiM}_{0.5}\text{Mn}_{1.5}\text{O}_4$ ($\text{M} = \text{Ni}$) 조성은 $\text{LiNi}_{0.5}\text{Mn}_{1.5}\text{O}_4$ 상 이외에 암염구조 NiO 가 생성되었는데 산소 분위기 열처리를 통해서도

제거되지 않았다. $\text{LiM}_{0.5}\text{Mn}_{1.5}\text{O}_4$ ($\text{M} = \text{Co}$)조성은 균일한 $\text{LiCo}_{0.5}\text{Mn}_{1.5}\text{O}_4$ 복합상이 20mol%까지 형성됨을 XRD로 확인 할 수 있었다. 구조분석 결과 Li_2MnO_3 상이 과량 형성되고 $\text{Li}(\text{Ni},\text{Co},\text{Mn})\text{O}_2$ 상 분율은 감소함을 알 수 있었다. 리튬 함량별 상구조에서 확인되었던 코발트와 니켈 조성 분리 현상도 관찰되었다. 최상의 성능은 코발트 스피넬이 복합된 경우로 용량 감소 없이 수명과 전압 감소가 개선됨을 확인할 수 있었다.

본 연구 결과는 향후 고용량 양극 소재로 각광 받는 리튬 과잉 복합 양극재의 상용화에 기여할 수 있을 것이다.

주요어: 양극, 리튬, 리튬이온전지, 스피넬, 복합체

학 번: 2014-30221